

**Original citation:**

Elliott, Charles M. and Fritz, Hans. (2016) On approximations of the curve shortening flow and of the mean curvature flow based on the DeTurck trick. IMA Journal of Numerical Analysis . doi: 10.1093/imanum/drw020

**Permanent WRAP URL:**

<http://wrap.warwick.ac.uk/78789>

**Copyright and reuse:**

The Warwick Research Archive Portal (WRAP) makes this work by researchers of the University of Warwick available open access under the following conditions. Copyright © and all moral rights to the version of the paper presented here belong to the individual author(s) and/or other copyright owners. To the extent reasonable and practicable the material made available in WRAP has been checked for eligibility before being made available.

Copies of full items can be used for personal research or study, educational, or not-for profit purposes without prior permission or charge. Provided that the authors, title and full bibliographic details are credited, a hyperlink and/or URL is given for the original metadata page and the content is not changed in any way.

**Publisher's statement:**

This is a pre-copyedited, author-produced PDF of an article accepted for publication in IMA Journal of Numerical Analysis following peer review. The version of record Elliott, Charles M. and Fritz, Hans. (2016) On approximations of the curve shortening flow and of the mean curvature flow based on the DeTurck trick. IMA Journal of Numerical Analysis .is available online at: <http://dx.doi.org/10.1093/imanum/drw020>

**A note on versions:**

The version presented here may differ from the published version or, version of record, if you wish to cite this item you are advised to consult the publisher's version. Please see the 'permanent WRAP url' above for details on accessing the published version and note that access may require a subscription.

For more information, please contact the WRAP Team at: [wrap@warwick.ac.uk](mailto:wrap@warwick.ac.uk)

# On Approximations of the Curve Shortening Flow and of the Mean Curvature Flow based on the DeTurck trick

Charles M. Elliott\* and Hans Fritz\*

## Abstract

In this paper we discuss novel numerical schemes for the computation of the curve shortening and mean curvature flows that are based on special reparametrizations. The main idea is to use special solutions to the harmonic map heat flow in order to reparametrize the equations of motion. This idea is widely known from the Ricci flow as the DeTurck trick. By introducing a variable time scale for the harmonic map heat flow, we obtain families of numerical schemes for the reparametrized flows. For the curve shortening flow this family unveils a surprising geometric connection between the numerical schemes in [5] and [9]. For the mean curvature flow we obtain families of schemes with good mesh properties similar to those in [3]. We prove error estimates for the semi-discrete scheme of the curve shortening flow. The behaviour of the fully-discrete schemes with respect to the redistribution of mesh points is studied in numerical experiments. We also discuss possible generalizations of our ideas to other extrinsic flows.

**Key words.** Curve shortening flow, mean curvature flow, harmonic map heat flow, DeTurck trick, parametric finite elements, error estimates, tangential redistributions, mesh properties.

**AMS subject classifications.** 65M60, 65M15, 35K93, 53C44, 58E20.

## 1 Introduction

### Motivation

The numerical analysis and the approximation of geometric flows have made significant progress during the last decades, see [10, 14] and references therein. Different numerical schemes for geometric flows such as the mean curvature flow and the Willmore flow have been proposed by several authors - all very appealing for different kinds of reason. In [13], for example, Dziuk presented a discretization of the mean curvature flow based on the fact that the mean curvature flow is a kind of diffusion equation for the surface embedding. On the other hand, Barrett, Garcke and Nürnberg introduced in a series of papers, see [2, 3, 4, 5, 6], numerical schemes with good properties with respect to the redistribution of mesh points. Algorithms providing time-dependent rearrangements of mesh points that prevent mesh degenerations are indeed very desirable. In fact, it can be stated that the formation of degenerate meshes in the simulation of geometric flows is the Achilles heel of many state of the art algorithms that are based on the parametric approach. Numerical simulations usually have to be stopped, when the mesh degenerates and some sophisticated machinery for remeshing the polyhedral surfaces, for example, using harmonic maps between surfaces [29], has to be applied. It seems therefore to be a far better solution of this problem to use algorithms that already induce tangential motions that lead to good redistributions of mesh points, see [2, 3, 4, 5, 6]. On the other hand, introducing schemes that lead to artificial tangential motions seems to be problematic too. Obviously, discrete solutions with non-vanishing tangential motions cannot converge to smooth solutions with vanishing tangential velocities. Hence, such solutions cannot converge to the surface parametrization evolving according to the original (that is non-reparametrized) system of PDEs. It is thus unclear whether there is at all a well-defined evolution of the surface

---

\*Mathematics Institute, Zeeman Building, University of Warwick, Coventry. CV4 7AL. UK  
C.M.Elliott@warwick.ac.uk, H.Fritz@warwick.ac.uk

parametrization that is approximated by the discrete solution. Since the numerical analysis of geometric flows is usually based on the analysis of non-degenerate evolution equations for the surface parametrization rather than on the analysis of evolving shapes only determined by their normal velocity, the numerical analysis of such schemes seems to be very difficult.

## Our approach

An obvious possibility to tackle this problem is to replace the original evolution equations by suitable reparametrizations that lead to the desired tangential motions in the discrete setting. An interesting reparametrization of the curve shortening flow can be found in the paper of Deckelnick and Dziuk [9]. Surprisingly, it turns out that this reparametrization can be linked to the so-called DeTurck trick. This trick refers to an idea, which was originally introduced by DeTurck for the Ricci flow for purely analytical reasons, see [11] and [21] for details. Reparametrizing the Ricci flow by solutions to the harmonic map heat flow leads to a strongly parabolic PDE, which is now known as the Ricci-DeTurck flow or as the dual Ricci-harmonic map heat flow. Fortunately, this idea is not restricted to the Ricci flow. Rather, it is possible to apply this idea also to other geometric flows such as the curve shortening and mean curvature flows, see [1, 20]. Below, we will explicitly derive the reparametrized evolution equations of these flows by using solutions to harmonic map heat flows. For the curve shortening flow, we will obtain the evolution equations considered by Deckelnick and Dziuk in [9] for numerical reasons as a special case of our more general approach. As we will see, the reparametrization by the harmonic map heat flow gives rise to tangential motions, which we here aim to exploit for purely numerical reasons, namely for the tangential redistribution of the mesh points. Since the numerical scheme in [9] is fully based on a consistent discretization of a non-degenerate system of PDEs, it is possible to prove rigorous error estimates. This still holds in our more general setting. Unfortunately, in general, the scheme in [9] does not provide sufficiently large redistributions that are able to keep the mesh points approximately equidistributed. The reason for this lack seems to be that the time scale on which the tangential redistributions take place is just too large.

In this paper, we hence generalize the idea to use the DeTurck trick as a tool of deriving useful reparametrizations of geometric evolution equations by introducing a variable time scale. Our aim is to develop novel algorithms which can be analysed rigorously and which also provide good mesh properties. We here say that a discrete curve has good mesh properties if all mesh segments have approximately the same length. For higher-dimensional hypersurfaces a triangulation is said to be a good mesh if the quotient of the diameter of a simplex and of the radius of the largest ball contained in it is reasonable small for all simplices of the triangulation, see also definition (7.3) below. This seems to be a good quantity to evaluate the mesh quality, since it plays an important role in the numerical analysis of PDEs. An interesting open question is the rigorous proof that an algorithm maintains this mesh quality.

Our approach leads to families of numerical schemes for the approximation of the curve shortening and mean curvature flows depending on a parameter  $\alpha > 0$ , which determines the time scale for the tangential motions of the surface parametrization. Indeed, it is not very surprising that for a special choice of this parameter, here for  $\alpha = 1$ , we recover the semi-discrete problem studied in [9], that is

$$\int_0^{2\pi} \hat{X}_{ht} \cdot \varphi_h |\hat{X}_{h\theta}|^2 d\theta + \int_0^{2\pi} \hat{X}_{h\theta} \cdot \varphi_{h\theta} d\theta = 0, \quad \forall \varphi_h \in \mathcal{S}_h^2, 0 < t < T,$$

where  $\hat{X}_h \in H^{1,2}((0, T), \mathcal{S}_h^2)$  is an approximation to the reparametrized curve shortening flow. Here,  $\mathcal{S}_h$  denotes the space of piecewise linear, continuous functions  $\varphi_h : [0, 2\pi] \rightarrow \mathbb{R}$  with  $\varphi_h(0) = \varphi_h(2\pi)$  on a given grid in  $[0, 2\pi]$  with grid size  $h$ . We are also able to recover a scheme similar to the curve shortening flow scheme in [5] if we formally choose  $\alpha = 0$ . This means that we are able to connect the schemes in [5] and in [9] by a family of numerical schemes depending on the time scale parameter  $\alpha$ . To be more precise, for  $\alpha = 0$ , Algorithm 1 proposed below simplifies to

$$\int_0^{2\pi} \left( \left( \frac{\hat{X}_h^{m+1} - \hat{X}_h^m}{\tau} \cdot \nu_h^m \right) (\nu_h^m \cdot \varphi_h) \right) |\hat{X}_{h\theta}^m|^2 d\theta + \int_0^{2\pi} \hat{X}_{h\theta}^{m+1} \cdot \varphi_{h\theta} d\theta = 0, \quad \forall \varphi_h \in \mathcal{S}_h^2,$$

while the solution of algorithm (2.16a) from [5] satisfies

$$\int_0^{2\pi} I_h \left( \left( \frac{\hat{X}_h^{m+1} - \hat{X}_h^m}{\tau} \cdot \rho_h^{m+1} \right) (\rho_h^{m+1} \cdot \varphi_h) \right) d\theta + \int_0^{2\pi} \hat{X}_{h\theta}^{m+1} \cdot \varphi_{h\theta} d\theta = 0, \quad \forall \varphi_h \in \mathcal{S}_h^2,$$

where  $I_h$  denotes the Lagrange interpolation operator and  $\rho_h^{m+1} \in \mathcal{S}_h^2$  is defined such that in each node  $\theta_j \in [0, 2\pi]$  of the grid it is given by the mean value of the piecewise constant vector field  $\nu_h^{m+1}|_{\hat{X}_h^{m+1}}$ .

The important similarities between both schemes are the appearance of a discrete normal projection acting on the discrete time derivative and the multiplication of this term by the square of the length element. Furthermore, the elliptic operator in both schemes only depends linearly on the curve parametrization, which is a rather surprising result, since the curve shortening flow itself is non-linear with respect to the curve parametrization. In [5] the normal projection is motivated by the fact that the geometric problem associated with the curve shortening flow only describes the normal velocity, whereas the tangential motion is undetermined by the geometry, and therefore, regarded as free. It is hence a bit surprising that the algorithm based on this view gives rise to desirable tangential motions that lead to the advantageous redistribution of the mesh points. In our derivation, the normal projection is a formal limit of a certain map which has its origin in the reparametrization by the DeTurck trick. This observation leads to the interesting question whether the tangential redistributions observed in [5] could be explained as the limiting behaviour of the DeTurck reparametrization process. Although, we are able to formally choose  $\alpha = 0$  in our algorithms, which in the one-dimensional case  $n = 1$  leads to the above scheme, it has to be stated that the derivation of the reparametrized evolution equations is only valid for  $\alpha > 0$ . Unfortunately, it is not only the derivation, which becomes problematic for the choice  $\alpha = 0$ , but also the system of PDEs for the surface parametrization itself. This means that the reparametrized evolution equation that underlies Algorithm 1 changes from a non-degenerate system of parabolic differential equations for  $\alpha > 0$  to a system of PDEs where the normal component of the system looks parabolic and its tangential part seems to be elliptic. We, therefore, restrict the analytical part of this paper to the case  $\alpha > 0$ . Nevertheless, the relation between Algorithm 1 for  $\alpha = 0$  and the scheme proposed in [5] strengthens the idea, that for a suitable choice of the parameter  $\alpha > 0$  a sufficiently good redistribution behaviour of the mesh points should be achievable. In order to confirm this assumption we study the limiting behaviour  $\alpha \searrow 0$  of our algorithms in numerical experiments.

In contrast to the curve shortening flow, our numerical schemes for the mean curvature flow seem to be totally new. Although, it is still possible to connect them loosely to the scheme in [3], the main difference between both approaches is that our schemes are based on the consistent discretization of a non-degenerate system of parabolic PDEs for the surface parametrization, whereas the scheme in [3] is based on the evolution equation for the normal velocity of the surface, and hence on a degenerate equation. This difference becomes manifest in the appearance of an additional (second order) term in our numerical scheme for the mean curvature flow.

The here presented approach is based on the DeTurck trick and the harmonic map heat flow. At first glance this approach seems to be rather ad hoc and it does not seem to be clear why this approach should lead to schemes with good mesh properties. Yet, the following observations strengthen the idea that it is indeed possible to produce nice meshes by using DeTurck reparametrizations.

1. Under certain assumptions it is possible to prove that solutions to the harmonic map heat flow converge to harmonic maps for long times; see [16].
2. Under certain assumptions, harmonic maps of surfaces are conformal maps; see, for example, in [17]. We therefore expect that the map  $y_h^m$  in Algorithms 2 and 3 of this paper will also approximate a conformal map – at least for very small  $\alpha$ .
3. Suppose that there is a conformal map between two surfaces with different Riemannian metrics. Furthermore, suppose that one surface is approximated by a simplicial mesh such that the triangles do not have any sharp angles with respect to the corresponding metric. The image of this mesh under the conformal map, or more precisely, under a good approximation thereof should then give a good mesh for the other surface.

Any rigorous results in this direction are far beyond the scope of this paper. In the above arguments we have not made use of any properties of the curve shortening and mean curvature flows. Hence, our approach should be applicable in a much wider context; see Section 8. In the main part of this paper, however, we will focus on the curve shortening and mean curvature flows. The applicability of our approach might be restricted by the fact that, in the general case, solutions to the harmonic map heat flow can generate singularities in finite time; see, for example, in [7]. It is unclear whether these singularities then also arise in the curve shortening-DeTurck and mean curvature-DeTurck flows.

## Related work

The redistribution of mesh points in order to prevent mesh degenerations has been studied for quite a long time. In [22], a non-local equation for the tangential velocity functional of curves in  $\mathbb{R}^2$  was introduced and utilized for the first time. Later, this functional has been studied in detail in [24] showing that the redistribution preserves relative local lengths of curve segments. The method was then generalized in [25] in order to achieve asymptotically uniform redistribution of grid points for evolving curves. In [26] this approach was extended by the addition of a diffusive term to the equation of the tangential velocity. The advantages of adding a diffusive term to the curve shortening flow have already been exploited in [9]. The scheme proposed in [26] is suitably chosen in order to uniformly redistribute the mesh points.

Only recently, a numerical scheme for the tangential redistribution of mesh points on higher-dimensional manifolds has been proposed in [27]. The approach of this paper is based on an appropriate variation of the surface velocities. The additional tangential velocities are chosen in such a way that the volume density of the surface parametrization can be controlled. In order to obtain well-defined problems, the authors assume that the tangential velocities are in fact gradient fields. This assumption then leads to elliptic problems, in which time is an additional parameter. The authors demonstrate the effectiveness of their approach in numerical experiments. It is an interesting question whether controlling relative volumes during the evolution can really prevent the formation of mesh degenerations in general. Reparametrizations by harmonic maps, see [29], might be an interesting alternative, since it allows for conformal remeshing.

We believe that introducing additional equations into numerical schemes in order to control certain mesh quantities not only increases the computational costs, but also makes the numerical analysis of the scheme much more involved. Hence, we aim to use a kind of built-in reparametrization based on the DeTurck trick such that we do not have to solve other problems than the (reparametrized) evolution equation of the surface parametrization. This approach differs from the schemes in [22, 24, 25, 26, 27, 29], where a larger system of PDEs is considered in order to improve or maintain the mesh quality. We therefore only compare our numerical results to the schemes in [3, 4, 5], which are also in the spirit of a built-in approach. We expect that such an approach can reduce the computational errors, while still providing sufficiently good mesh behaviour.

In [29], the DeTurck trick has already been used to derive a family of numerical schemes for the approximation of the curve shortening flow; compare equation (4.5) in [29] to (2.16) in the present paper. However, the author does not use an important trick, which we introduce below and which is crucial for different kinds of reasons. Firstly, without this trick, it is not possible to consider the limit  $\alpha \searrow 0$  and to see the connection between the schemes in [5] and [9]. Furthermore, in [29] a variable for the mean curvature vector has to be introduced in order to be able to discretize the weak formulation by piecewise linear finite elements. In contrast to this result, it is not necessary in our formulation to introduce any further variables for the computation of the curve shortening flow. Finally, the author in [29] does not prove any error estimates for his scheme, which we will do in Theorem 2. We are not aware of any further publications, where the reparametrization of the evolution equations by solutions to the harmonic map heat flow has been used to develop numerical schemes based on surface finite elements. We would like to emphasize that the ideas developed in this paper are not restricted to any dimension  $n$  of the hypersurface, even if the error analysis in Section 3 is only valid for the one-dimensional case, that is  $n = 1$ .

## Outline of the paper

This paper is organised as follows. In Section 2, we introduce the DeTurck trick and apply it to the  $n$ -dimensional mean curvature flow. We derive the reparametrized evolution equations in detail for any dimension  $n \in \mathbb{N}$  of the hypersurface. In Section 3, we discretize a weak formulation of the reparametrized evolution equations in space for the one-dimensional problem, that is for the curve shortening flow. We then show that it is possible to adapt the proof of the error estimates in [9] to our novel schemes with only minor changes. In Section 4, numerical tests for the computation of the curve shortening flow are presented with a special focus on the behaviour of the mesh properties. In Section 5, we derive a weak formulation of the reparametrized mean curvature flow of  $n$ -dimensional hypersurfaces for arbitrary  $n \in \mathbb{N}$ . These equations are then lifted onto the moving hypersurface and discretized using surface finite

elements. In Section 6, we introduce a variant of the DeTurck trick that leads to a formulation, which only contains terms that can be related to the first variation of some energy functionals. In Section 7, numerical experiments for the mean curvature flow are presented with a special focus on mesh properties. We compare the performance of our schemes to the behaviour of the scheme proposed in [3]. Possible generalizations of the ideas developed in this paper to other geometric flows are explained in Section 8. In Section 9, we discuss the results of this paper and compare our approach to previous works.

The main results of this paper are Algorithm 1 for the computation of the reparametrized curve shortening flow and Algorithms 2 and 3 for the computation of the reparametrized mean curvature flow.

## 2 Reparametrizations via the DeTurck trick

### 2.1 Notation

Henceforward, let  $\mathcal{M}$  be a closed (that is compact and without boundary), connected, orientable,  $n$ -dimensional smooth manifold  $\mathcal{M}$  (that is a topological space which is locally homeomorphic to open subsets of  $\mathbb{R}^n$  via the so-called coordinate charts  $\mathcal{C}_i : U_i \subset \mathcal{M} \rightarrow \Omega_i \subset \mathbb{R}^n$ , where the transition maps  $\mathcal{C}_i \circ \mathcal{C}_j^{-1}$  are supposed to be smooth). We denote the identity map on  $\mathcal{M}$  by  $id(p) = p$ . Let  $g$  be a smooth Riemannian metric on  $\mathcal{M}$ , that is a smooth map which defines an inner product on all tangent spaces of  $\mathcal{M}$ . The components of  $g$  with respect to a local coordinate system are denoted by  $g_{ij}$ . The components of the inverse of the matrix  $(g_{ij})_{i,j=1,\dots,n}$  are denoted by  $g^{ij}$ . In the following we will make use of the convention to sum over repeated indices.

For a  $C^2$ -function  $f : \mathcal{M} \rightarrow \mathbb{R}$  the Laplace operator  $\Delta_g$  with respect to the metric  $g$  is defined by

$$(\Delta_g f) \circ \mathcal{C}_1^{-1} := g^{ij} \left( \frac{\partial^2 F}{\partial \theta^i \partial \theta^j} - \Gamma(g)_{ij}^k \frac{\partial F}{\partial \theta^k} \right), \quad (2.1)$$

where  $F := f \circ \mathcal{C}_1^{-1}$  and  $\Gamma(g)_{ij}^k$  are the Christoffel symbols of  $g$  defined by

$$\Gamma(g)_{ij}^k := \frac{1}{2} g^{kl} \left( \frac{\partial g_{lj}}{\partial \theta^i} + \frac{\partial g_{li}}{\partial \theta^j} - \frac{\partial g_{ij}}{\partial \theta^l} \right). \quad (2.2)$$

If  $\mathcal{M}$  is a hypersurface of the Euclidean space  $\mathbb{R}^{n+1}$  and  $g$  the corresponding induced metric, the Laplace operator  $\Delta_g$  coincides with the surface Laplacian defined in Definition (2.3) of [10]. Because of Jacobi's formula for the derivative of the determinant we obtain

$$\begin{aligned} g^{ij} \Gamma(g)_{ij}^k &= g^{ij} g^{kl} \left( \frac{\partial g_{li}}{\partial \theta^j} - \frac{1}{2} \frac{\partial g_{ij}}{\partial \theta^l} \right) = -\frac{\partial g^{jk}}{\partial \theta^j} - g^{kl} \frac{1}{\sqrt{|g|}} \frac{\partial \sqrt{|g|}}{\partial \theta^l} \\ &= -\frac{1}{\sqrt{|g|}} \frac{\partial}{\partial \theta^j} \left( \sqrt{|g|} g^{jk} \right), \end{aligned}$$

where  $|g| = \det(g_{ij})$ , and hence,

$$(\Delta_g f) \circ \mathcal{C}_1^{-1} = \frac{1}{\sqrt{|g|}} \frac{\partial}{\partial \theta^i} \left( \sqrt{|g|} g^{ij} \frac{\partial F}{\partial \theta^j} \right),$$

which is sometimes used as an alternative definition of the Laplace operator.

The map Laplacian  $\Delta_{g,h}\psi$  of a twice-differentiable map  $\psi : \mathcal{M} \rightarrow \mathcal{M}$  is defined by

$$(\mathcal{C}_2 \circ (\Delta_{g,h}\psi) \circ \mathcal{C}_1^{-1})^q := g^{ij} \left( \frac{\partial^2 \Psi^q}{\partial \theta^i \partial \theta^j} - \Gamma(g)_{ij}^k \frac{\partial \Psi^q}{\partial \theta^k} + (\Gamma(h)_{mn}^q \circ \Psi) \frac{\partial \Psi^m}{\partial \theta^i} \frac{\partial \Psi^n}{\partial \theta^j} \right). \quad (2.3)$$

Here,  $g^{ij}$  and  $\Gamma(g)_{ij}^k$  are the components of the inverse of the matrix  $(g_{ij})_{i,j=1,\dots,n}$ , and respectively, of the Christoffel symbols of  $g$  with respect to the coordinate chart  $\mathcal{C}_1$ . The quantities  $h^{mn}$  and  $\Gamma(h)_{mn}^q$  denote the corresponding quantities of the metric  $h$  with respect to the coordinate chart  $\mathcal{C}_2$ . The local representation of the map  $\psi$  with respect to the charts  $\mathcal{C}_1$  and  $\mathcal{C}_2$  is denoted by  $\Psi := \mathcal{C}_2 \circ \psi \circ \mathcal{C}_1^{-1}$ . In order to keep notation simple yet concise, we make the convention that whenever a term depends on different local coordinates, then the indices  $i, j, k, l$

refers to the coordinates with respect to the chart  $\mathcal{C}_1$ , whereas the indices  $m, n, p, q$  refers to the coordinates with respect to the chart  $\mathcal{C}_2$  – if not otherwise stated.

The differential  $\nabla f$  of a differentiable function  $f : \mathcal{M} \rightarrow \mathbb{R}$  on  $\mathcal{M}$  is defined by

$$(\nabla f)(w) \circ \mathcal{C}_1^{-1} := W^j \frac{\partial F}{\partial \theta^j},$$

where  $F := f \circ \mathcal{C}_1^{-1}$  and  $w = W^j \frac{\partial}{\partial \theta^j}$  is an arbitrary tangent vector field on  $\mathcal{M}$ .

For a function  $f$  on an  $n$ -dimensional smooth hypersurface  $\mathcal{N} \subset \mathbb{R}^{n+1}$  differentiable at  $p \in \mathcal{N}$ , the tangential gradient  $\nabla_{\mathcal{N}} f(p)$  is defined by

$$\nabla_{\mathcal{N}} f(p) := \nabla \bar{f}(p) - (\nu \cdot \nabla \bar{f})(p) \nu(p).$$

Here,  $\nu(p)$  is a unit normal to  $\mathcal{N}$  at the point  $p$  and  $\bar{f}$  is a differentiable extension of  $f$  to an open neighbourhood  $U \subset \mathbb{R}^{n+1}$  of  $p$ , such that  $\bar{f}|_{\mathcal{N} \cap U} = f|_{\mathcal{N} \cap U}$ . The tangential gradient is well-defined, since the above definition only depends on the values of  $f$  on  $\mathcal{N}$ , see [10] for more details. The components of the tangential gradient are denoted by

$$\begin{pmatrix} \underline{D}_1 f \\ \vdots \\ \underline{D}_{n+1} f \end{pmatrix} := \nabla_{\mathcal{N}} f.$$

We define the integral on a Riemannian manifold  $(\mathcal{M}, g)$  with respect to a Riemannian metric  $g$  by

$$\int_{\mathcal{M}} f d\sigma_g := \int_{\Omega} f \circ \mathcal{C}_1^{-1} \sqrt{\det(g_{ij})} d^n \theta,$$

where  $\mathcal{C}_1 : U \subset \mathcal{M} \rightarrow \Omega \subset \mathbb{R}^n$  denotes a local coordinate chart of  $\mathcal{M}$  and  $f : \mathcal{M} \rightarrow \mathbb{R}$  is an integrable function on  $\mathcal{M}$  with support  $\text{supp} f \subset U$ . Using a partition of unity, this definition easily generalizes to arbitrary integrable functions on  $\mathcal{M}$ . On  $n$ -dimensional hypersurfaces in  $\mathbb{R}^{n+1}$  the volume form that is induced by the  $n$ -dimensional Hausdorff measure will be denoted by  $d\sigma$ . Below, we will make use of the matrix scalar product  $A : B$  defined by  $A : B = \sum_{\alpha, \beta=1}^{n+1} A_{\alpha\beta} B_{\alpha\beta}$  for  $A, B \in \mathbb{R}^{(n+1) \times (n+1)}$ .

Henceforward, let  $x : \mathcal{M} \times [0, T] \rightarrow \mathbb{R}^{n+1}$  be a time-dependent embedding of  $\mathcal{M}$  (that is an immersion on  $\mathcal{M}$  which is a homeomorphism of  $\mathcal{M}$  onto  $x(\mathcal{M})$ ) of at least class  $C^2$ . The local representation of the embedding  $x$  with respect to a coordinate chart  $\mathcal{C}_1$  is denoted by  $X := x \circ \mathcal{C}_1^{-1}$ . The embedding  $x$  induces a Riemannian metric on  $\mathcal{M}$  given by the pull-back of the Euclidean metric  $\mathfrak{e}$  in  $\mathbb{R}^{n+1}$ . In the following we will denote this metric by  $g(t) := x(t)^* \mathfrak{e}$ . In local coordinates the pull-back metric  $g(t)$  is given by

$$g_{ij}(\theta, t) := \mathfrak{e} \left( \frac{\partial X}{\partial \theta^i}(\theta, t), \frac{\partial X}{\partial \theta^j}(\theta, t) \right) := \frac{\partial X}{\partial \theta^i}(\theta, t) \cdot \frac{\partial X}{\partial \theta^j}(\theta, t), \quad \forall i, j \in \{1, \dots, n\}. \quad (2.4)$$

The Euclidean metric  $\mathfrak{e}$  will also be denoted by  $\cdot$ , where convenient. For the sake of convenience, we will omit the full dependency of the metric  $g(p, t)(\cdot, \cdot)$  with  $(p, t) \in \mathcal{M} \times [0, T]$  where appropriate.

## 2.2 The mean curvature flow

We next introduce the (non-reparametrized) evolution equations of the mean curvature flow. Very readable surveys on the mean curvature flow are [15] and [23]. The embedding  $x$  is said to evolve according to the mean curvature flow if

$$\frac{\partial}{\partial t} x = -(H\nu) \circ x. \quad (2.5)$$

Here,  $\nu$  denotes a unit normal vector field on the embedded hypersurface  $\Gamma(t) := x(\mathcal{M}, t) \subset \mathbb{R}^{n+1}$  and  $H$  is the corresponding mean curvature, that is

$$H \circ X := g^{ij} \frac{\partial X}{\partial \theta^i} \cdot \frac{\partial (\nu \circ X)}{\partial \theta^j} = -g^{ij} \frac{\partial^2 X}{\partial \theta^i \partial \theta^j} \cdot (\nu \circ X). \quad (2.6)$$

The definition of the mean curvature flow does not depend on the choice of the unit normal field. Please note that our definition of the mean curvature  $H$  differs from the more common

one by a factor of  $n$ . For example, the mean curvature of the  $n$ -dimensional unit sphere with unit normal pointing outwards is  $n$ . From the definition of the induced metric (2.4) one directly obtains that

$$\frac{\partial^2 X}{\partial \theta^i \partial \theta^j} \cdot \frac{\partial X}{\partial \theta^l} = \frac{1}{2} \left( \frac{\partial g_{jl}}{\partial \theta^i} + \frac{\partial g_{il}}{\partial \theta^j} - \frac{\partial g_{ij}}{\partial \theta^l} \right) = g_{kl} \Gamma(g)_{ij}^k,$$

and hence,

$$\Gamma(g)_{ij}^k \frac{\partial X}{\partial \theta^k} = \frac{\partial^2 X}{\partial \theta^i \partial \theta^j} \cdot \frac{\partial X}{\partial \theta^l} g^{lk} \frac{\partial X}{\partial \theta^k}.$$

The following identity

$$\mathbf{1} = (\nu \circ X) \otimes (\nu \circ X) + g^{lk} \frac{\partial X}{\partial \theta^l} \otimes \frac{\partial X}{\partial \theta^k}$$

then gives the decomposition

$$\frac{\partial^2 X}{\partial \theta^i \partial \theta^j} = \frac{\partial^2 X}{\partial \theta^i \partial \theta^j} \cdot (\nu \circ X)(\nu \circ X) + \Gamma(g)_{ij}^k \frac{\partial X}{\partial \theta^k}. \quad (2.7)$$

From this identity, the definition of the Laplace operator (2.1) and the definition of the mean curvature in (2.6) it follows that

$$(\Delta_{g(t)} x) \circ \mathcal{C}_1^{-1} = g^{ij} \frac{\partial^2 X}{\partial \theta^i \partial \theta^j} \cdot (\nu \circ X)(\nu \circ X) = -(H \circ X)(\nu \circ X).$$

This means that

$$\Delta_{g(t)} x = -(H\nu) \circ x. \quad (2.8)$$

The mean curvature flow is therefore given by the following non-linear heat equation

$$\frac{\partial}{\partial t} x = \Delta_{g(t)} x,$$

where  $g(t) = x(t)^* \mathfrak{e}$ .

A straightforward calculation gives the evolution of the metric  $g(t)$  under the mean curvature flow, see, for example, in [23],

$$\frac{\partial}{\partial t} g_{ij} = 2(H \circ X) \frac{\partial^2 X}{\partial \theta^i \partial \theta^j} \cdot (\nu \circ X) = -2(H \circ X) \mathcal{H}_{ij},$$

where  $\mathcal{H}_{ij}$  denotes the components of the second fundamental form  $\mathcal{H}$  defined by

$$\mathcal{H}_{ij} := \frac{\partial X}{\partial \theta^i} \cdot \frac{\partial (\nu \circ X)}{\partial \theta^j}.$$

### 2.3 The harmonic map heat flow

We now introduce the harmonic map heat flow on the manifold  $\mathcal{M}$ . A map  $\psi : \mathcal{M} \times [0, T) \rightarrow \mathcal{M}$  is said to evolve according to the harmonic map heat flow if

$$\frac{\partial}{\partial t} \psi = \Delta_{g,h} \psi.$$

Here,  $\Delta_{g,h}$  denotes the map Laplacian (2.3) on  $\mathcal{M}$  with respect to the smooth metrics  $g$  and  $h$  on  $\mathcal{M}$ . In the following we choose  $g$  to be the time-dependent metric  $g(t) = x(t)^* \mathfrak{e}$  induced by the embedding  $x(t)$  on  $\mathcal{M}$ . This choice is motivated by our aim to use the harmonic map heat flow  $\psi$  for the reparametrization of the mean curvature flow  $x(t)$ . In contrast to the metric  $g(t)$ , we keep the metric  $h$  arbitrary but fixed in time. In local coordinates, the harmonic map heat flow is given by

$$\frac{\partial}{\partial t} \Psi^q = g^{ij} \left( \frac{\partial^2 \Psi^q}{\partial \theta^i \partial \theta^j} - \Gamma(g)_{ij}^k \frac{\partial \Psi^q}{\partial \theta^k} + (\Gamma(h)_{mn}^q \circ \Psi) \frac{\partial \Psi^m}{\partial \theta^i} \frac{\partial \Psi^n}{\partial \theta^j} \right).$$

Short-time existence and uniqueness results for this flow can be found in [16]. In the following, we choose the initial conditions for the harmonic map heat flow to be the identity on  $\mathcal{M}$ , that is  $\psi(\cdot, 0) = id(\cdot)$ .



## 2.4 The mean curvature-DeTurck flow

The DeTurck trick was first introduced in [11] in order to prove existence and uniqueness of solutions to the Ricci flow [19]. Later, it was also used to prove existence and uniqueness for the mean curvature flow, see for example [1, 20]. However, to our knowledge, it has never been considered in a numerical setting so far.

The basic idea of the trick is to reparametrize the original evolution equations by a smooth family of diffeomorphisms solving the harmonic map heat flow. Since this is a rather special concept, we here provide a detailed derivation of the reparametrized evolution equations. In the first step, we combine the mean curvature flow with the harmonic map heat flow by

$$(P) = \begin{cases} \frac{\partial}{\partial t} x = -(H\nu) \circ x, & \text{with } x(\cdot, 0) = x_0 \text{ on } \mathcal{M}, \\ \frac{\partial}{\partial t} \psi_\alpha = \frac{1}{\alpha} \Delta_{g(t), h} \psi_\alpha, & \text{with } g(t) := x(t)^* \mathbf{e} \text{ and } \psi_\alpha(\cdot, 0) = id(\cdot) \text{ on } \mathcal{M}, \end{cases}$$

where  $h$  is a fixed yet arbitrary smooth Riemannian metric on  $\mathcal{M}$ . We have here introduced the inverse diffusion constant  $\alpha > 0$  in the harmonic map heat flow. As we will see below, this parameter determines the time scale on which the tangential motions of the reparametrized flow take place. Since  $\psi_\alpha(\cdot, 0) = id(\cdot)$  is initially the identity, the map  $\psi_\alpha(t)$  remains a diffeomorphism at least for short times. We can thus reparametrize the mean curvature flow by

$$\hat{x}_\alpha(t) := (\psi_\alpha(t)^{-1})^* x(t) := x(t) \circ \psi_\alpha(t)^{-1}. \quad (2.9)$$

The idea to use this reparametrization is usually called the DeTurck trick. Two properties of this reparametrization are of particular importance: Firstly, it turns out that  $\hat{x}_\alpha(t)$  is the solution to a strongly parabolic PDE, see [1]. Secondly, this PDE does not depend on the solution  $\psi(t)$  of the harmonic map heat flow. The latter point, in particular, means that it will not be necessary to solve the harmonic map heat flow numerically, although we use the above reparametrization to derive our numerical schemes. We now state the reparametrized evolution equations.

**Lemma 1** (Mean curvature-DeTurck flow). *The evolution equation for the reparametrized embedding  $\hat{x}_\alpha : \mathcal{M} \times [0, T] \rightarrow \mathbb{R}^{n+1}$  defined in (2.9) is given by*

$$\frac{\partial}{\partial t} \hat{x}_\alpha = \Delta_{\hat{g}_\alpha(t)} \hat{x}_\alpha - \frac{1}{\alpha} \nabla \hat{x}_\alpha (V_\alpha). \quad (2.10)$$

In local coordinates this equation looks like

$$\frac{\partial}{\partial t} \hat{X}_\alpha = \hat{g}_\alpha^{ij} \left( \frac{\partial^2 \hat{X}_\alpha}{\partial \theta^i \partial \theta^j} - \Gamma(\hat{g}_\alpha)_{ij}^k \frac{\partial \hat{X}_\alpha}{\partial \theta^k} \right) - \frac{1}{\alpha} V_\alpha^j \frac{\partial \hat{X}_\alpha}{\partial \theta^j}.$$

Here,  $\hat{g}_\alpha(t) := (\hat{x}_\alpha(t))^* \mathbf{e}$  is the metric induced by the embedding  $\hat{x}_\alpha(t)$ , and  $V_\alpha$  is the vector field locally defined by

$$V_\alpha^j := \hat{g}_\alpha^{kl} (\Gamma(h)_{kl}^j - \Gamma(\hat{g}_\alpha)_{kl}^j). \quad (2.11)$$

*Proof.* Below, we will make use of the fact that the pull-back metrics  $(\psi_\alpha(t)^{-1})^* g(t)$  and  $(\hat{x}_\alpha(t))^* \mathbf{e}$  on  $\mathcal{M}$  are equal

$$(\psi_\alpha(t)^{-1})^* g(t) = (\psi_\alpha(t)^{-1})^* (x(t)^* \mathbf{e}) = (x(t) \circ \psi_\alpha(t)^{-1})^* \mathbf{e} = (\hat{x}_\alpha(t))^* \mathbf{e} = \hat{g}_\alpha(t). \quad (2.12)$$

For the time derivative of  $\hat{x}_\alpha$  we obtain

$$\begin{aligned} \frac{\partial}{\partial t} \hat{x}_\alpha(t) &= \frac{\partial}{\partial t} x(t) \circ \psi_\alpha(t)^{-1} + (\nabla x \circ \psi_\alpha(t)^{-1}) \left( \frac{\partial}{\partial t} (\psi_\alpha(t)^{-1}) \right) \\ &= (\Delta_{g(t)} x) \circ \psi_\alpha(t)^{-1} + (\nabla x \circ \psi_\alpha(t)^{-1}) \left( \frac{\partial}{\partial t} (\psi_\alpha(t)^{-1}) \right), \end{aligned}$$

where  $\nabla x$  denotes the differential of  $x$ . From the identity  $\psi_\alpha(t)^{-1} \circ \psi_\alpha(t) = id$ , it follows that

$$\frac{\partial (\Psi_\alpha^{-1})^j}{\partial t} \circ \Psi_\alpha = - \left( \frac{\partial (\Psi_\alpha^{-1})^j}{\partial \theta^q} \right) \circ \Psi_\alpha \frac{\partial \Psi_\alpha^q}{\partial t},$$

where  $\Psi_\alpha = \mathcal{C}_2 \circ \psi_\alpha \circ \mathcal{C}_1^{-1}$ . And hence,

$$\frac{\partial(\Psi_\alpha^{-1})^j}{\partial t} = -\frac{\partial(\Psi_\alpha^{-1})^j}{\partial \theta^q} \left( \frac{\partial \Psi_\alpha^q}{\partial t} \circ \Psi_\alpha^{-1} \right).$$

For  $X := x \circ \mathcal{C}_1^{-1}$  and  $\hat{X}_\alpha := \hat{x}_\alpha \circ \mathcal{C}_2^{-1} = x \circ \psi_\alpha(t)^{-1} \circ \mathcal{C}_2^{-1} = X \circ \Psi_\alpha^{-1}$ , we then obtain

$$\begin{aligned} \frac{\partial(\Psi_\alpha^{-1})^j}{\partial t} \left( \frac{\partial X}{\partial \theta^j} \circ \Psi_\alpha^{-1} \right) &= - \left( \frac{\partial X}{\partial \theta^j} \circ \Psi_\alpha^{-1} \right) \frac{\partial(\Psi_\alpha^{-1})^j}{\partial \theta^q} \left( \frac{\partial \Psi_\alpha^q}{\partial t} \circ \Psi_\alpha^{-1} \right) \\ &= -\frac{\partial \hat{X}_\alpha}{\partial \theta^q} \left( \frac{\partial \Psi_\alpha^q}{\partial t} \circ \Psi_\alpha^{-1} \right). \end{aligned}$$

We now conclude that

$$\begin{aligned} (\nabla x \circ \psi_\alpha(t)^{-1}) \left( \frac{\partial}{\partial t} (\psi_\alpha(t)^{-1}) \right) &= -(\nabla \hat{x}_\alpha) \left( \left( \frac{\partial}{\partial t} \psi_\alpha(t) \right) \circ \psi_\alpha(t)^{-1} \right) \\ &= -\frac{1}{\alpha} (\nabla \hat{x}_\alpha) ((\Delta_{g(t),h} \psi_\alpha(t)) \circ \psi_\alpha(t)^{-1}). \end{aligned} \quad (2.13)$$

According to Remark 2.46 in [8], the following identity holds

$$(\Delta_{g(t),h} \psi_\alpha(t)) \circ \psi_\alpha(t)^{-1} = \Delta_{(\psi_\alpha(t)^{-1})^* g(t),h} id. \quad (2.14)$$

Using the fact that  $(\psi_\alpha(t)^{-1})^* g(t) = (\hat{x}_\alpha(t))^* \mathfrak{e} = \hat{g}_\alpha(t)$ , we obtain

$$(\Delta_{g(t),h} \psi_\alpha(t)) \circ \psi_\alpha(t)^{-1} = \Delta_{\hat{g}_\alpha(t),h} id.$$

For the sake of completeness we here give a short proof of the identity (2.14). In local coordinates we have

$$\begin{aligned} \frac{\partial(\Psi_\alpha^q \circ \Psi_\alpha^{-1})}{\partial \theta^m} &= \frac{\partial \Psi_\alpha^q}{\partial \theta^i} \circ \Psi_\alpha^{-1} \frac{\partial(\Psi_\alpha^{-1})^i}{\partial \theta^m}, \\ \frac{\partial^2(\Psi_\alpha^q \circ \Psi_\alpha^{-1})}{\partial \theta^m \partial \theta^n} &= \frac{\partial^2 \Psi_\alpha^q}{\partial \theta^i \partial \theta^j} \circ \Psi_\alpha^{-1} \frac{\partial(\Psi_\alpha^{-1})^i}{\partial \theta^m} \frac{\partial(\Psi_\alpha^{-1})^j}{\partial \theta^n} + \frac{\partial \Psi_\alpha^q}{\partial \theta^i} \circ \Psi_\alpha^{-1} \frac{\partial^2(\Psi_\alpha^{-1})^i}{\partial \theta^m \partial \theta^n}, \\ \hat{g}_{\alpha mn} &= (g_{ij} \circ \Psi_\alpha^{-1}) \frac{\partial(\Psi_\alpha^{-1})^i}{\partial \theta^m} \frac{\partial(\Psi_\alpha^{-1})^j}{\partial \theta^n}, \\ (g^{ij} \circ \Psi_\alpha^{-1}) &= \hat{g}_\alpha^{mn} \frac{\partial(\Psi_\alpha^{-1})^i}{\partial \theta^m} \frac{\partial(\Psi_\alpha^{-1})^j}{\partial \theta^n}. \end{aligned}$$

A straightforward calculation also shows that

$$\hat{g}_\alpha^{mn} \Gamma(\hat{g}_\alpha)_{mn}^p \frac{\partial(\Psi_\alpha^{-1})^k}{\partial \theta^p} = (g^{ij} \circ \Psi_\alpha^{-1}) \Gamma(g)_{ij}^k \circ \Psi_\alpha^{-1} + \hat{g}_\alpha^{mn} \frac{\partial^2(\Psi_\alpha^{-1})^k}{\partial \theta^m \partial \theta^n}.$$

Using these formulas, we obtain

$$\begin{aligned} &(\mathcal{C}_2 \circ (\Delta_{\hat{g}_\alpha(t),h} id) \circ \mathcal{C}_1^{-1})^q \\ &= \hat{g}_\alpha^{mn} \left( \frac{\partial^2(\Psi_\alpha^q \circ \Psi_\alpha^{-1})}{\partial \theta^m \partial \theta^n} - \Gamma(\hat{g}_\alpha)_{mn}^p \frac{\partial(\Psi_\alpha^q \circ \Psi_\alpha^{-1})}{\partial \theta^p} + \Gamma(h)_{pr}^q \frac{\partial(\Psi_\alpha^p \circ \Psi_\alpha^{-1})}{\partial \theta^m} \frac{\partial(\Psi_\alpha^r \circ \Psi_\alpha^{-1})}{\partial \theta^n} \right) \\ &= (g^{ij} \circ \Psi_\alpha^{-1}) \frac{\partial^2 \Psi_\alpha^q}{\partial \theta^i \partial \theta^j} \circ \Psi_\alpha^{-1} + \frac{\partial \Psi_\alpha^q}{\partial \theta^i} \circ \Psi_\alpha^{-1} \frac{\partial^2(\Psi_\alpha^{-1})^i}{\partial \theta^m \partial \theta^n} \hat{g}_\alpha^{mn} \\ &\quad - (g^{ij} \circ \Psi_\alpha^{-1}) \Gamma(g)_{ij}^k \circ \Psi_\alpha^{-1} \frac{\partial \Psi_\alpha^q}{\partial \theta^k} \circ \Psi_\alpha^{-1} - \hat{g}_\alpha^{mn} \frac{\partial^2(\Psi_\alpha^{-1})^k}{\partial \theta^m \partial \theta^n} \frac{\partial \Psi_\alpha^q}{\partial \theta^k} \circ \Psi_\alpha^{-1} \\ &\quad + \Gamma(h)_{pr}^q \frac{\partial \Psi_\alpha^p}{\partial \theta^i} \circ \Psi_\alpha^{-1} \frac{\partial \Psi_\alpha^r}{\partial \theta^j} \circ \Psi_\alpha^{-1} (g^{ij} \circ \Psi_\alpha^{-1}) \\ &= (g^{ij} \circ \Psi_\alpha^{-1}) \left( \frac{\partial^2 \Psi_\alpha^q}{\partial \theta^i \partial \theta^j} - \Gamma(g)_{ij}^k \frac{\partial \Psi_\alpha^q}{\partial \theta^k} + (\Gamma(h)_{pr}^q \circ \Psi_\alpha) \frac{\partial \Psi_\alpha^p}{\partial \theta^i} \frac{\partial \Psi_\alpha^r}{\partial \theta^j} \right) \circ \Psi_\alpha^{-1}. \end{aligned}$$

Together with the definition (2.3) of the map Laplacian this shows (2.14). On the other hand the map Laplacian of the identity is just given by

$$(\mathcal{C}_2 \circ (\Delta_{\hat{g}_\alpha(t),h} id) \circ \mathcal{C}_1^{-1})^j = \hat{g}_\alpha^{kl} (\Gamma(h)_{kl}^j - \Gamma(\hat{g}_\alpha)_{kl}^j) = V_\alpha^j,$$

where we have obtained the components  $V_\alpha^j$  of the vector field  $V_\alpha$  defined in (2.11). We summarize that

$$(\Delta_{g(t),h}\psi_\alpha(t)) \circ \psi_\alpha(t)^{-1} = V_\alpha,$$

and with (2.13) we obtain

$$(\nabla x \circ \psi_\alpha(t)^{-1}) \left( \frac{\partial}{\partial t} (\psi_\alpha(t)^{-1}) \right) = -\frac{1}{\alpha} (\nabla \hat{x}_\alpha)(V_\alpha).$$

From identity (2.8) it follows that

$$(\Delta_{g(t)}x) \circ \psi_\alpha(t)^{-1} = -((H\nu) \circ x) \circ \psi_\alpha(t)^{-1} = -(H\nu) \circ (x \circ \psi_\alpha(t)^{-1}) = -(H\nu) \circ \hat{x}_\alpha,$$

and thus,

$$(\Delta_{g(t)}x) \circ \psi_\alpha(t)^{-1} = \Delta_{\hat{g}_\alpha(t)}\hat{x}_\alpha,$$

where we have used that  $g(t) = x(t)^*\mathfrak{e}$  and  $\hat{g}_\alpha(t) = (\hat{x}_\alpha(t))^*\mathfrak{e}$ .  $\square$

**Remark 1.** Please note that one can, in principle, recover the solution  $x(t)$  to (2.5) from the solution to (2.10) by solving the ODE  $\frac{\partial}{\partial t}\psi_\alpha = \frac{1}{\alpha}V_\alpha \circ \psi_\alpha$  and setting  $x(t) = \hat{x}_\alpha(t) \circ \psi_\alpha(t)$ . Actually, this is how one can prove short-time existence of solutions to the mean curvature flow by using the existence result for the mean curvature-DeTurck flow, see, for example, in [1]. The reason why it is easier to establish short-time existence for the mean curvature-DeTurck flow than for the mean curvature flow itself is that the DeTurck flow is strongly parabolic whereas the original flow is not.

## 2.5 The time separation trick

We next introduce an idea, which will turn out to be advantageous for the spatial discretization and its numerical analysis.

In order to motivate this idea we will first apply the results of Lemma 1 to the curve shortening flow. In this case the reference manifold  $\mathcal{M}$  is one-dimensional. Without loss of generality we can assume that  $\mathcal{M}$  is parametrized in such a way that  $\hat{X}_\alpha : [0, 2\pi] \rightarrow \mathbb{R}^2$  with  $\hat{X}_\alpha(0) = \hat{X}_\alpha(2\pi)$ . The metric  $\hat{g}_\alpha$  is then given by  $\hat{g}_{\alpha 11} = |\frac{\partial \hat{X}_\alpha}{\partial \theta}|^2$ , and hence,

$$\Gamma(\hat{g})_{11}^1 = \frac{1}{2} \left| \frac{\partial \hat{X}_\alpha}{\partial \theta} \right|^{-2} \frac{\partial}{\partial \theta} \left| \frac{\partial \hat{X}_\alpha}{\partial \theta} \right|^2 = \left| \frac{\partial \hat{X}_\alpha}{\partial \theta} \right|^{-2} \frac{\partial \hat{X}_\alpha}{\partial \theta} \cdot \frac{\partial^2 \hat{X}_\alpha}{\partial \theta^2}.$$

Since  $h$  is a fixed yet arbitrary metric, we are allowed to choose  $h$  such that  $h_{11}$  is constant on  $[0, 2\pi]$  and thus  $\Gamma(h)_{11}^1 = 0$ . The reparametrized evolution equations of the curve shortening flow in local coordinates are then given by

$$\frac{\partial}{\partial t} \hat{X}_\alpha = \left| \frac{\partial \hat{X}_\alpha}{\partial \theta} \right|^{-2} \left( \frac{\partial^2 \hat{X}_\alpha}{\partial \theta^2} - \left| \frac{\partial \hat{X}_\alpha}{\partial \theta} \right|^{-2} \frac{\partial \hat{X}_\alpha}{\partial \theta} \cdot \frac{\partial^2 \hat{X}_\alpha}{\partial \theta^2} \frac{\partial \hat{X}_\alpha}{\partial \theta} \right) + \frac{1}{\alpha} \left| \frac{\partial \hat{X}_\alpha}{\partial \theta} \right|^{-4} \frac{\partial \hat{X}_\alpha}{\partial \theta} \cdot \frac{\partial^2 \hat{X}_\alpha}{\partial \theta^2} \frac{\partial \hat{X}_\alpha}{\partial \theta}, \quad (2.15)$$

which directly simplifies to

$$\frac{\partial}{\partial t} \hat{X}_\alpha = \left| \frac{\partial \hat{X}_\alpha}{\partial \theta} \right|^{-2} \frac{\partial^2 \hat{X}_\alpha}{\partial \theta^2} + \frac{1-\alpha}{\alpha} \left| \frac{\partial \hat{X}_\alpha}{\partial \theta} \right|^{-4} \frac{\partial \hat{X}_\alpha}{\partial \theta} \cdot \frac{\partial^2 \hat{X}_\alpha}{\partial \theta^2} \frac{\partial \hat{X}_\alpha}{\partial \theta}. \quad (2.16)$$

For  $\alpha = 1$  this equation was the starting point of the analysis in [9]. In [29] it was later derived for arbitrary  $\alpha > 0$ . However, the author in [29] did not use the following trick described below, which is crucial for two kinds of reasons. Firstly, the trick makes it possible to choose, at least formally,  $\alpha = 0$  in the reparametrized equations. This choice unveils the origin of the tangential redistributions in the scheme proposed in [5]. Secondly, our trick leads to an equation that can be directly discretized in space. In contrast to this result, the author in [29] had to introduce a variable for the curvature vector

$$-(H\nu) \circ \hat{X}_\alpha = \left| \frac{\partial \hat{X}_\alpha}{\partial \theta} \right|^{-1} \frac{\partial}{\partial \theta} \left( \left| \frac{\partial \hat{X}_\alpha}{\partial \theta} \right|^{-1} \frac{\partial \hat{X}_\alpha}{\partial \theta} \right)$$

in order to be able to discretize the reparametrized equations with piecewise linear finite elements, see Problem 4.1.7 in [29]. As a result, the author obtained a system of equations for the

computation of the mean curvature vector and of the curve shortening flow. However, for the computation of the curve shortening flow, such a system seems to be a bit exaggerated. We would like to emphasize that in contrast to the results in [29], the above derivations are also valid for the higher-dimensional case, that is for the mean curvature flow.

We now continue with the general case. Our trick is based on the following two observations. Firstly, as we have seen in (2.8), the Laplace operator with respect to metric  $\hat{g}_\alpha$  of the map  $\hat{x}_\alpha$  is equal to  $-(H\nu) \circ \hat{x}_\alpha$ . Secondly, the Laplace operator with respect to  $\hat{g}_\alpha$  satisfies the following identity

$$\Delta_{\hat{g}_\alpha} \hat{x}_\alpha = \text{tr}_{\hat{g}_\alpha}(\nabla^{\hat{g}_\alpha} \nabla \hat{x}_\alpha) = \text{tr}_{\hat{g}_\alpha}(\nabla^h \nabla \hat{x}_\alpha) + \nabla \hat{x}_\alpha(V_\alpha),$$

where  $\text{tr}_{\hat{g}_\alpha}$  denotes the trace with respect to the metric  $\hat{g}_\alpha$ . This easily follows from definition (2.11) and the formulas for the covariant derivatives of the differential  $\nabla \hat{x}_\alpha$  with respect to the metrics  $\hat{g}_\alpha$  and  $h$ , which are

$$\begin{aligned} (\nabla_i^{\hat{g}_\alpha} \nabla_j \hat{x}_\alpha) \circ \mathcal{C}_1^{-1} &= \frac{\partial^2 \hat{X}_\alpha}{\partial \theta^i \partial \theta^j} - \Gamma(\hat{g}_\alpha)_{ij}^k \frac{\partial \hat{X}_\alpha}{\partial \theta^k}, \\ (\nabla_i^h \nabla_j \hat{x}_\alpha) \circ \mathcal{C}_1^{-1} &= \frac{\partial^2 \hat{X}_\alpha}{\partial \theta^i \partial \theta^j} - \Gamma(h)_{ij}^k \frac{\partial \hat{X}_\alpha}{\partial \theta^k}. \end{aligned}$$

Please note that the vector field  $(\nabla_{V_\alpha} \hat{x}_\alpha) \circ \mathcal{C}_1^{-1} = V_\alpha^j \frac{\partial \hat{X}_\alpha}{\partial \theta^j}$  is tangential to the embedded hypersurface  $\Gamma(t)$ . We thus obtain the following decomposition of the operator  $\text{tr}_{\hat{g}_\alpha}(\nabla^h \nabla \hat{x}_\alpha)$  in its normal and tangential parts

$$(\nu \circ \hat{x}_\alpha) \otimes (\nu \circ \hat{x}_\alpha) \text{tr}_{\hat{g}_\alpha}(\nabla^h \nabla \hat{x}_\alpha) = \Delta_{\hat{g}_\alpha} \hat{x}_\alpha, \quad (2.17)$$

$$(P \circ \hat{x}_\alpha) \text{tr}_{\hat{g}_\alpha}(\nabla^h \nabla \hat{x}_\alpha) = -\nabla \hat{x}_\alpha(V_\alpha), \quad (2.18)$$

where  $P = \mathbf{1} - \nu \otimes \nu$  is the projection onto the tangent bundle of  $\Gamma$ . Inserting this decomposition into (2.10) then gives

$$\begin{aligned} \frac{\partial}{\partial t} \hat{x}_\alpha &= (\nu \circ \hat{x}_\alpha) \otimes (\nu \circ \hat{x}_\alpha) \text{tr}_{\hat{g}_\alpha}(\nabla^h \nabla \hat{x}_\alpha) + \frac{1}{\alpha} (P \circ \hat{x}_\alpha) \text{tr}_{\hat{g}_\alpha}(\nabla^h \nabla \hat{x}_\alpha) \\ &= \left( (\nu \circ \hat{x}_\alpha) \otimes (\nu \circ \hat{x}_\alpha) + \frac{1}{\alpha} P \circ \hat{x}_\alpha \right) \text{tr}_{\hat{g}_\alpha}(\nabla^h \nabla \hat{x}_\alpha). \end{aligned}$$

Applying the inverse map

$$((\nu \circ \hat{x}_\alpha) \otimes (\nu \circ \hat{x}_\alpha) + \alpha P \circ \hat{x}_\alpha) = (\alpha \mathbf{1} + (1 - \alpha)(\nu \circ \hat{x}_\alpha) \otimes (\nu \circ \hat{x}_\alpha)) \quad (2.19)$$

leads to the following evolution equations.

**Theorem 1.** *The mean curvature-DeTurck flow  $\hat{x}_\alpha : \mathcal{M} \times [0, T) \rightarrow \mathbb{R}^{n+1}$  defined in (2.9) satisfies*

$$(\alpha \mathbf{1} + (1 - \alpha)(\nu \circ \hat{x}_\alpha) \otimes (\nu \circ \hat{x}_\alpha)) \frac{\partial}{\partial t} \hat{x}_\alpha = \text{tr}_{\hat{g}_\alpha}(\nabla^h \nabla \hat{x}_\alpha), \quad \text{with } \hat{x}_\alpha(\cdot, 0) = x_0(\cdot) \text{ on } \mathcal{M}, \quad (2.20)$$

and in local coordinates respectively,

$$\left( \alpha \mathbf{1} + (1 - \alpha)(\nu \circ \hat{X}_\alpha) \otimes (\nu \circ \hat{X}_\alpha) \right) \frac{\partial}{\partial t} \hat{X}_\alpha = \hat{g}_\alpha^{ij} \left( \frac{\partial^2 \hat{X}_\alpha}{\partial \theta^i \partial \theta^j} - \Gamma(h)_{ij}^k \frac{\partial \hat{X}_\alpha}{\partial \theta^k} \right),$$

with  $\hat{X}_\alpha(\cdot, 0) = X_0(\cdot)$ .

Please note that the initial values of the reparametrized flow are just given by the initial values of the original flow. The reason for this is that the map  $\psi(t)$  satisfies  $\psi(\cdot, 0) = \text{id}(\cdot)$  on  $\mathcal{M}$ . For the curve shortening flow with the metric  $h$  chosen such that  $h_{11}$  is constant, we obtain

$$\left( \alpha \mathbf{1} + (1 - \alpha)(\nu \circ \hat{X}_\alpha) \otimes (\nu \circ \hat{X}_\alpha) \right) \frac{\partial}{\partial t} \hat{X}_\alpha = \left| \frac{\partial \hat{X}_\alpha}{\partial \theta} \right|^{-2} \frac{\partial^2 \hat{X}_\alpha}{\partial \theta^2}. \quad (2.21)$$

This equation will be the basis of the next section. Although the inverse diffusion constant  $\alpha$  has to be positive in the derivation of (2.20), it is yet possible to formally choose  $\alpha = 0$  in this equation. This would lead to

$$(\nu \circ \hat{x}_\alpha)(\nu \circ \hat{x}_\alpha) \cdot \frac{\partial}{\partial t} \hat{x}_\alpha = \text{tr}_{\hat{g}_\alpha}(\nabla^h \nabla \hat{x}_\alpha).$$

### 3 The reparametrized curve shortening flow

#### 3.1 Weak formulation and discretization

In this section, we develop an algorithm for the computation of the reparametrized curve shortening flow (2.21). Our algorithm is based on a straightforward discretization of the weak formulation of the reparametrized flow with piecewise linear finite elements. Henceforward, we omit the subscript  $\alpha$  and write  $\hat{X}_t$  and  $\hat{X}_\theta$  instead of  $\frac{\partial \hat{X}}{\partial t}$  and  $\frac{\partial \hat{X}}{\partial \theta}$ . Furthermore, we use the notation  $\nu$  for the local parametrization of the unit normal field  $\nu \circ \hat{X}$ . Multiplying (2.21) by a test function  $\varphi \in H^{1,2}(\mathbb{R}/2\pi, \mathbb{R}^2)$  as well as by the density function  $|\hat{X}_\theta|^2$  and integrating by parts yield

$$\int_0^{2\pi} \left( \alpha \hat{X}_t \cdot \varphi + (1 - \alpha)(\hat{X}_t \cdot \nu)(\nu \cdot \varphi) \right) |\hat{X}_\theta|^2 d\theta + \int_0^{2\pi} \hat{X}_\theta \cdot \varphi_\theta d\theta = 0, \quad 0 < t < T. \quad (3.1)$$

This weak formulation is now discretized in space by linear finite elements. In the following we consider the finite element mesh  $\theta_j \in [0, 2\pi)$ ,  $j = 1, \dots, N$ , with grid size  $h = |\theta_{j+1} - \theta_j|$  where  $\theta_{N+1} := 2\pi + \theta_1$ . The space of continuous functions  $\varphi_h : \mathbb{R}/2\pi \rightarrow \mathbb{R}$  that are linear on  $[\theta_j, \theta_{j+1}]$ ,  $\forall j = 1, \dots, N$ , is denoted by  $\mathcal{S}_h$ . The basis functions  $\phi_j \in \mathcal{S}_h$  are defined such that  $\phi_j(\theta_i) = \delta_{ij}$ ,  $\forall i, j = 1, \dots, N$ . The linear Lagrange interpolation for a continuous function  $f$  on  $\mathbb{R}/2\pi$  is defined by

$$I_h f := \sum_{j=1}^N f(\theta_j) \phi_j.$$

For a curve  $\Gamma_h = \hat{X}_h([0, 2\pi))$  with  $\hat{X}_h \in \mathcal{S}_h^2$ , a piecewise constant vector field  $\nu_h : [0, 2\pi] \rightarrow \mathbb{R}^2$  with  $|\nu_h| = 1$  and

$$\nu_h \cdot (\hat{X}_h(\theta_{j+1}) - \hat{X}_h(\theta_j)) = 0 \quad \text{on } [\theta_j, \theta_{j+1}) \text{ for } j = 1, \dots, N,$$

is called a unit normal vector field to  $\hat{X}_h$ .

#### 3.2 Convergence results

**Theorem 2.** *Let  $\alpha \in (0, 1]$  and suppose that  $\hat{X} \in C^{2,1}(\mathbb{R}/2\pi \times [0, T], \mathbb{R}^2)$  is a solution of*

$$\begin{aligned} \alpha \hat{X}_t + (1 - \alpha)(\nu \cdot \hat{X}_t)\nu &= |\hat{X}_\theta|^{-2} \hat{X}_{\theta\theta}, \quad \text{in } \mathbb{R}/2\pi \times (0, T), \\ \hat{X}(\cdot, 0) &= X_0(\cdot), \quad \text{on } \mathbb{R}/2\pi, \end{aligned}$$

with

$$\begin{aligned} \hat{X}_t &\in L^\infty((0, T), H^{1,2}(\mathbb{R}/2\pi, \mathbb{R}^2)) \cap L^2((0, T), H^{2,2}(\mathbb{R}/2\pi, \mathbb{R}^2)), \\ |\hat{X}_\theta| &\geq c_0 > 0, \quad \text{in } \mathbb{R}/2\pi \times [0, T]. \end{aligned} \quad (3.2)$$

Then there exists a constant  $h_0 > 0$  depending on  $\hat{X}$ ,  $T$  and  $\alpha$  such that for every  $0 < h \leq h_0$  there is a unique solution  $\hat{X}_h \in H^{1,2}((0, T), \mathcal{S}_h^2)$  of the non-linear, semi-discrete problem

$$\int_0^{2\pi} \left( \alpha \hat{X}_{ht} \cdot \varphi_h + (1 - \alpha)(\hat{X}_{ht} \cdot \nu_h)(\nu_h \cdot \varphi_h) \right) |\hat{X}_{h\theta}|^2 d\theta + \int_0^{2\pi} \hat{X}_{h\theta} \cdot \varphi_{h\theta} d\theta = 0, \quad (3.3)$$

$\forall \varphi_h \in \mathcal{S}_h^2$ ,  $0 < t < T$ , with initial data  $\hat{X}_h(\cdot, 0) = (I_h X_0)(\cdot)$  on  $\mathbb{R}/2\pi$ , and

$$\begin{aligned} &\alpha \int_0^T \|(\hat{X}_t - \hat{X}_{ht})(t)\|_{L^2(0, 2\pi)}^2 dt + (1 - \alpha) \int_0^T \|\nu_h \cdot (\hat{X}_t - \hat{X}_{ht})(t)\|_{L^2(0, 2\pi)}^2 dt \\ &+ \max_{t \in [0, T]} \|(\hat{X} - \hat{X}_h)(t)\|_{H^{1,2}(0, 2\pi)}^2 \leq C e^{\frac{M}{\alpha} T} h^2. \end{aligned}$$

The constants  $C$  and  $M$  depend on the continuous solution  $\hat{X}$  and on  $T$ .

*Proof.* The following proof is adopted from [9], where the special case  $\alpha = 1$  is considered. It is based on the Schauder fixed point theorem. For this, we first introduce the Banach space  $\mathcal{Z}_h := C^0([0, T], \mathcal{S}_h^2)$  of time-continuous functions with values in  $\mathcal{S}_h^2$  equipped with the norm

$$\|\hat{X}_h\|_{\mathcal{Z}_h} := \sup_{t \in [0, T]} \|\hat{X}_h(t)\|_{L^2},$$

and the convex subset  $\mathcal{B}_h$  defined by

$$\mathcal{B}_h := \left\{ \hat{X}_h \in \mathcal{Z}_h \mid \sup_{t \in [0, T]} e^{-\frac{M}{\alpha} t} \|(\hat{X}_\theta - \hat{X}_{h\theta})(t)\|_{L^2}^2 \leq K^2 h^2 \text{ and } \hat{X}_h(\cdot, 0) = (I_h X_0)(\cdot) \right\}, \quad (3.4)$$

where we will choose the constants  $K, M > 0$  below. Please note that the space  $\mathcal{S}_h$  is finite-dimensional. For sufficiently large  $K$  the subset  $\mathcal{B}_h$  is non-empty, since then  $I_h \hat{X} \in \mathcal{B}_h$ . Moreover,  $\mathcal{B}_h$  is closed. For  $\hat{X}_h \in \mathcal{B}_h$ ,  $0 \leq t \leq T$ , we obtain

$$\begin{aligned} \|(\hat{X}_\theta - \hat{X}_{h\theta})(t)\|_{L^\infty} &\leq \|(\hat{X}_\theta - (I_h \hat{X})_\theta)(t)\|_{L^\infty} + \|((I_h \hat{X})_\theta - \hat{X}_{h\theta})(t)\|_{L^\infty} \\ &\leq Ch + \frac{C}{\sqrt{h}} \|((I_h \hat{X})_\theta - \hat{X}_{h\theta})(t)\|_{L^2} \\ &\leq Ch + \frac{C}{\sqrt{h}} (\|((I_h \hat{X})_\theta - \hat{X}_\theta)(t)\|_{L^2} + \|(\hat{X}_\theta - \hat{X}_{h\theta})(t)\|_{L^2}) \\ &\leq C\sqrt{h}(1 + e^{\frac{M}{2\alpha} T} K), \end{aligned}$$

where we have used interpolation and inverse inequalities. Because of assumption (3.2), we can thus assume that for  $h_0 = h_0(M, K, \hat{X}, T, \alpha)$  sufficiently small the following lower and upper bounds hold

$$|\hat{X}_{h\theta}| \geq \frac{1}{2} c_0, \quad \text{and} \quad |\hat{X}_{h\theta}| \leq C \quad \text{in } \mathbb{R}/2\pi \times [0, T]. \quad (3.5)$$

We now consider the operator  $F$  defined by

$$F : \hat{X}_h \in \mathcal{B}_h \mapsto \hat{Y}_h \in \mathcal{Z}_h,$$

where  $\hat{Y}_h \in \mathcal{Z}_h$  is the unique solution of the following linear system of ODEs

$$\int_0^{2\pi} \left( \alpha \hat{Y}_{ht} \cdot \varphi_h + (1 - \alpha)(\hat{Y}_{ht} \cdot \nu_h)(\nu_h \cdot \varphi_h) \right) |\hat{X}_{h\theta}|^2 d\theta + \int_0^{2\pi} \hat{Y}_{h\theta} \cdot \varphi_{h\theta} d\theta = 0 \quad (3.6)$$

$\forall \varphi_h \in \mathcal{S}_h^2, 0 < t < T$ , with initial data  $\hat{Y}_h(\cdot, 0) = (I_h X_0)(\cdot)$ . Here,  $\nu_h$  is a piecewise constant unit normal vector field to the embedding  $\hat{X}_h$ . The operator  $F$  is continuous, since the solution  $\hat{Y}_h$  continuously depends on  $\hat{X}_h$ . Furthermore, we show below that  $\hat{Y}_h \in \mathcal{B}_h$  and that  $\|\hat{Y}_h\|_{H^{1,2}((0, T), \mathcal{S}_h^2)} \leq C$ . Hence, we have  $F(\mathcal{B}_h) \subset \mathcal{B}_h$ , and since the embedding  $H^{1,2}(0, T) \hookrightarrow C^0([0, T])$  is compact,  $F(\mathcal{B}_h) \subset H^{1,2}((0, T), \mathcal{S}_h^2)$  is a precompact subset of  $\mathcal{B}_h \subset C^0([0, T], \mathcal{S}_h^2)$ . The Schauder fixed point theorem therefore implies the existence of a fixed point  $F(\hat{X}_h) = \hat{X}_h$ , that is a solution of (3.3). The uniqueness of solutions to ODEs of the form  $x_t = f(x, t)$ , for  $f : G \subset \mathbb{R}^{m+1} \rightarrow \mathbb{R}^m$  locally Lipschitz continuous with respect to the variable  $x$ , implies that the solution  $\hat{X}_h$  to (3.3) is unique. In order to see that (3.3) is equivalent to such an equation, one chooses  $\varphi_h = \phi_i e_\beta$ ,  $i = 1, \dots, N$ ,  $\beta = 1, 2$ , with  $e_1 = (1, 0)^T$  and  $e_2 = (0, 1)^T$ , and inserts  $\hat{X}_h = \sum_{\gamma=1}^2 \sum_{j=1}^N \hat{\mathbf{X}}^{j\gamma} \phi_j e_\gamma$ . The resulting non-linear ODE then is

$$\sum_{\gamma=1}^2 \sum_{j=1}^N M_{ij\beta\gamma}(\hat{\mathbf{X}}) \hat{\mathbf{X}}_t^{j\gamma} + \sum_{\gamma=1}^2 \sum_{j=1}^N S_{ij\beta\gamma} \hat{\mathbf{X}}^{j\gamma} = 0, \quad \forall i = 1, \dots, N, \beta = 1, 2,$$

where the mass matrix  $M := (M_{ij\beta\gamma}(\hat{\mathbf{X}})) \in \mathbb{R}^{(2N) \times (2N)}$  non-linearly depends on the vector  $\hat{\mathbf{X}} := (\hat{\mathbf{X}}^{j\gamma}) \in \mathbb{R}^{2N}$ , whereas the components of the stiffness matrix  $S := (S_{ij\beta\gamma}) \in \mathbb{R}^{(2N) \times (2N)}$  are constants. The mass matrix is invertible if  $(\hat{\mathbf{X}}^{j+1, \gamma})_{\gamma=1,2} \neq (\hat{\mathbf{X}}^{j, \gamma})_{\gamma=1,2}$ , for all  $j = 1, \dots, N$ , where  $(\hat{\mathbf{X}}^{N+1, \gamma})_{\gamma=1,2} := (\hat{\mathbf{X}}^{1, \gamma})_{\gamma=1,2}$ . Furthermore, its inverse is locally Lipschitz continuous in  $G^* := \{\hat{\mathbf{X}} \in \mathbb{R}^{2N} \mid (\hat{\mathbf{X}}^{j+1, \gamma})_{\gamma=1,2} \neq (\hat{\mathbf{X}}^{j, \gamma})_{\gamma=1,2}\}$ . Since  $X_0$  is an embedding and  $\hat{X}_h(\cdot, 0) := (I_h X_0)(\cdot)$ , we have  $\hat{\mathbf{X}}(0) \in G^*$ . Hence, the standard uniqueness theorem for non-linear ODEs applies.

We now show that  $\hat{Y}_h \in \mathcal{B}_h$ . First, we obviously have  $\hat{Y}_h \in \mathcal{Z}_h$ , and from the weak formula-

tions (3.1) and (3.6) we obtain

$$\begin{aligned}
& \int_0^{2\pi} \left( \alpha(\hat{X}_t - \hat{Y}_{ht}) \cdot \varphi_h + (1 - \alpha)(\hat{X}_t - \hat{Y}_{ht}) \cdot \nu_h(\nu_h \cdot \varphi_h) \right) |\hat{X}_{h\theta}|^2 d\theta + \int_0^{2\pi} (\hat{X}_\theta - \hat{Y}_{h\theta}) \cdot \varphi_{h\theta} d\theta \\
&= \int_0^{2\pi} \left( \alpha \hat{X}_t \cdot \varphi_h + (1 - \alpha)(\hat{X}_t \cdot \nu_h)(\nu_h \cdot \varphi_h) \right) |\hat{X}_{h\theta}|^2 d\theta \\
&\quad - \int_0^{2\pi} \left( \alpha \hat{X}_t \cdot \varphi_h + (1 - \alpha)(\hat{X}_t \cdot \nu)(\nu \cdot \varphi_h) \right) |\hat{X}_\theta|^2 d\theta \\
&= \int_0^{2\pi} (|\hat{X}_{h\theta}|^2 - |\hat{X}_\theta|^2) \left( \alpha \hat{X}_t \cdot \varphi_h + (1 - \alpha)(\hat{X}_t \cdot \nu_h)(\nu_h \cdot \varphi_h) \right) d\theta \\
&\quad + \int_0^{2\pi} |\hat{X}_\theta|^2 (1 - \alpha) \left( (\hat{X}_t \cdot \nu_h)(\nu_h \cdot \varphi_h) - (\hat{X}_t \cdot \nu)(\nu \cdot \varphi_h) \right) d\theta \\
&= \int_0^{2\pi} (|\hat{X}_{h\theta}|^2 - |\hat{X}_\theta|^2) \left( \alpha \hat{X}_t \cdot \varphi_h + (1 - \alpha)(\hat{X}_t \cdot \nu_h)(\nu_h \cdot \varphi_h) \right) d\theta \\
&\quad + (1 - \alpha) \int_0^{2\pi} |\hat{X}_\theta|^2 \left( \hat{X}_t \cdot (\nu_h - \nu)(\nu_h \cdot \varphi_h) + (\hat{X}_t \cdot \nu)(\nu_h - \nu) \cdot \varphi_h \right) d\theta.
\end{aligned}$$

We now choose  $\varphi_h = I_h \hat{X}_t - \hat{Y}_{ht}$  and get

$$\begin{aligned}
& \int_0^{2\pi} \left( \alpha |\hat{X}_t - \hat{Y}_{ht}|^2 + (1 - \alpha) |\nu_h \cdot (\hat{X}_t - \hat{Y}_{ht})|^2 \right) |\hat{X}_{h\theta}|^2 d\theta + \int_0^{2\pi} (\hat{X}_\theta - \hat{Y}_{h\theta}) \cdot (\hat{X}_{t\theta} - \hat{Y}_{ht\theta}) d\theta \\
&= \int_0^{2\pi} \left( \alpha (\hat{X}_t - \hat{Y}_{ht}) \cdot (\hat{X}_t - I_h \hat{X}_t) + (1 - \alpha) (\hat{X}_t - \hat{Y}_{ht}) \cdot \nu_h \nu_h \cdot (\hat{X}_t - I_h \hat{X}_t) \right) |\hat{X}_{h\theta}|^2 d\theta \\
&\quad + \int_0^{2\pi} (\hat{X}_\theta - \hat{Y}_{h\theta}) \cdot (\hat{X}_{t\theta} - (I_h \hat{X}_t)_\theta) d\theta \\
&\quad + \int_0^{2\pi} (|\hat{X}_{h\theta}|^2 - |\hat{X}_\theta|^2) \left( \alpha \hat{X}_t \cdot (I_h \hat{X}_t - \hat{Y}_{ht}) + (1 - \alpha) (\hat{X}_t \cdot \nu_h) \nu_h \cdot (I_h \hat{X}_t - \hat{Y}_{ht}) \right) d\theta \\
&\quad + (1 - \alpha) \int_0^{2\pi} |\hat{X}_\theta|^2 \left( \hat{X}_t \cdot (\nu_h - \nu) \nu_h \cdot (I_h \hat{X}_t - \hat{Y}_{ht}) + (\hat{X}_t \cdot \nu)(\nu_h - \nu) \cdot (I_h \hat{X}_t - \hat{Y}_{ht}) \right) d\theta.
\end{aligned}$$

Using the lower and upper bounds in (3.5), we estimate

$$\begin{aligned}
& \frac{c_0^2}{4} \int_0^{2\pi} \alpha |\hat{X}_t - \hat{Y}_{ht}|^2 + (1 - \alpha) |\nu_h \cdot (\hat{X}_t - \hat{Y}_{ht})|^2 d\theta + \frac{1}{2} \frac{d}{dt} \int_0^{2\pi} |\hat{X}_\theta - \hat{Y}_{h\theta}|^2 d\theta \\
&\leq C \int_0^{2\pi} \alpha |\hat{X}_t - \hat{Y}_{ht}| |\hat{X}_t - I_h \hat{X}_t| + (1 - \alpha) |\nu_h \cdot (\hat{X}_t - \hat{Y}_{ht})| |\nu_h \cdot (\hat{X}_t - I_h \hat{X}_t)| d\theta \\
&\quad + \|(\hat{X}_t - I_h \hat{X}_t)_\theta\|_{L^2} \|\hat{X}_\theta - \hat{Y}_{h\theta}\|_{L^2} + \alpha \int_0^{2\pi} \|\hat{X}_{h\theta} - |\hat{X}_\theta|(|\hat{X}_{h\theta}| + |\hat{X}_\theta|)|\hat{X}_t\|_{L^2} |I_h \hat{X}_t - \hat{Y}_{ht}| d\theta \\
&\quad + (1 - \alpha) \int_0^{2\pi} \|\hat{X}_{h\theta} - |\hat{X}_\theta|(|\hat{X}_{h\theta}| + |\hat{X}_\theta|)|\hat{X}_t\|_{L^2} |\nu_h \cdot (I_h \hat{X}_t - \hat{Y}_{ht})| d\theta \\
&\quad + C(1 - \alpha) \int_0^{2\pi} |\hat{X}_t \cdot (\nu_h - \nu)| |\nu_h \cdot (I_h \hat{X}_t - \hat{Y}_{ht})| d\theta \\
&\quad + C(1 - \alpha) \int_0^{2\pi} |\hat{X}_t \cdot \nu| |(\nu_h - \nu) \cdot (I_h \hat{X}_t - \hat{Y}_{ht})| d\theta \\
&\leq C\alpha \|\hat{X}_t - I_h \hat{X}_t\|_{L^2} \|\hat{X}_t - \hat{Y}_{ht}\|_{L^2} + C(1 - \alpha) \|\nu_h \cdot (\hat{X}_t - I_h \hat{X}_t)\|_{L^2} \|\nu_h \cdot (\hat{X}_t - \hat{Y}_{ht})\|_{L^2} \\
&\quad + Ch \|\hat{X}_t\|_{H^{2,2}} \|\hat{X}_\theta - \hat{Y}_{h\theta}\|_{L^2} + C\alpha \|\hat{X}_t\|_{L^\infty} \int_0^{2\pi} |\hat{X}_{h\theta} - \hat{X}_\theta| |I_h \hat{X}_t - \hat{Y}_{ht}| d\theta \\
&\quad + C(1 - \alpha) \|\hat{X}_t\|_{L^\infty} \int_0^{2\pi} |\hat{X}_{h\theta} - \hat{X}_\theta| |\nu_h \cdot (I_h \hat{X}_t - \hat{Y}_{ht})| d\theta \\
&\quad + C(1 - \alpha) \int_0^{2\pi} |\hat{X}_t \cdot (\nu_h - \nu)| |\nu_h \cdot (I_h \hat{X}_t - \hat{Y}_{ht})| d\theta \\
&\quad + C(1 - \alpha) \int_0^{2\pi} |\hat{X}_t \cdot \nu| |(\nu_h - \nu) \cdot (I_h \hat{X}_t - \hat{Y}_{ht})| d\theta.
\end{aligned}$$

Applying the interpolation estimate  $\|\hat{X}_t - I_h \hat{X}_t\|_{L^2} \leq Ch \|\hat{X}_t\|_{H^{1,2}} \leq Ch$  then gives

$$\begin{aligned}
A &:= \frac{c_0^2}{4} \alpha \|\hat{X}_t - \hat{Y}_{ht}\|_{L^2}^2 + \frac{c_0^2}{4} (1 - \alpha) \|\nu_h \cdot (\hat{X}_t - \hat{Y}_{ht})\|_{L^2}^2 + \frac{1}{2} \frac{d}{dt} \|\hat{X}_\theta - \hat{Y}_{h\theta}\|_{L^2}^2 \\
&\leq Ch\alpha \|\hat{X}_t\|_{H^{1,2}} \|\hat{X}_t - \hat{Y}_{ht}\|_{L^2} + Ch(1 - \alpha) \|\hat{X}_t\|_{H^{1,2}} \|\nu_h \cdot (\hat{X}_t - \hat{Y}_{ht})\|_{L^2} \\
&\quad + Ch \|\hat{X}_t\|_{H^{2,2}} \|\hat{X}_\theta - \hat{Y}_{h\theta}\|_{L^2} + C\alpha \|\hat{X}_{h\theta} - \hat{X}_\theta\|_{L^2} \|I_h \hat{X}_t - \hat{Y}_{ht}\|_{L^2} \\
&\quad + C(1 - \alpha) \|\hat{X}_{h\theta} - \hat{X}_\theta\|_{L^2} \|\nu_h \cdot (I_h \hat{X}_t - \hat{Y}_{ht})\|_{L^2} \\
&\quad + C(1 - \alpha) \|\hat{X}_t\|_{L^\infty} \|\nu_h - \nu\|_{L^2} \|\nu_h \cdot (I_h \hat{X}_t - \hat{Y}_{ht})\|_{L^2} \\
&\quad + C(1 - \alpha) \|\hat{X}_t\|_{L^\infty} \|(\nu_h - \nu) \cdot (I_h \hat{X}_t - \hat{Y}_{ht})\|_{L^1} \\
&\leq Ch\alpha \|\hat{X}_t - \hat{Y}_{ht}\|_{L^2} + Ch(1 - \alpha) \|\nu_h \cdot (\hat{X}_t - \hat{Y}_{ht})\|_{L^2} \\
&\quad + Ch \|\hat{X}_t\|_{H^{2,2}} \|\hat{X}_\theta - \hat{Y}_{h\theta}\|_{L^2} + Ch\alpha \|\hat{X}_t\|_{H^{1,2}} \|\hat{X}_{h\theta} - \hat{X}_\theta\|_{L^2} + C\alpha \|\hat{X}_{h\theta} - \hat{X}_\theta\|_{L^2} \|\hat{X}_t - \hat{Y}_{ht}\|_{L^2} \\
&\quad + Ch(1 - \alpha) \|\hat{X}_t\|_{H^{1,2}} \|\hat{X}_{h\theta} - \hat{X}_\theta\|_{L^2} + C(1 - \alpha) \|\hat{X}_{h\theta} - \hat{X}_\theta\|_{L^2} \|\nu_h \cdot (\hat{X}_t - \hat{Y}_{ht})\|_{L^2} \\
&\quad + Ch(1 - \alpha) \|\hat{X}_t\|_{H^{1,2}} \|\nu_h - \nu\|_{L^2} + C(1 - \alpha) \|\nu_h - \nu\|_{L^2} \|\nu_h \cdot (\hat{X}_t - \hat{Y}_{ht})\|_{L^2} \\
&\quad + Ch(1 - \alpha) \|\hat{X}_t\|_{H^{1,2}} \|\nu_h - \nu\|_{L^2} + C(1 - \alpha) \|(\nu_h - \nu) \cdot (\hat{X}_t - \hat{Y}_{ht})\|_{L^1}.
\end{aligned}$$

Hence,

$$\begin{aligned}
A &\leq Ch\alpha \|\hat{X}_t - \hat{Y}_{ht}\|_{L^2} + Ch(1 - \alpha) \|\nu_h \cdot (\hat{X}_t - \hat{Y}_{ht})\|_{L^2} \\
&\quad + Ch \|\hat{X}_t\|_{H^{2,2}} \|\hat{X}_\theta - \hat{Y}_{h\theta}\|_{L^2} + Ch\alpha \|\hat{X}_{h\theta} - \hat{X}_\theta\|_{L^2} + C\alpha \|\hat{X}_{h\theta} - \hat{X}_\theta\|_{L^2} \|\hat{X}_t - \hat{Y}_{ht}\|_{L^2} \\
&\quad + Ch(1 - \alpha) \|\hat{X}_{h\theta} - \hat{X}_\theta\|_{L^2} + C(1 - \alpha) \|\hat{X}_{h\theta} - \hat{X}_\theta\|_{L^2} \|\nu_h \cdot (\hat{X}_t - \hat{Y}_{ht})\|_{L^2} \\
&\quad + Ch(1 - \alpha) \|\nu_h - \nu\|_{L^2} + C(1 - \alpha) \|\nu_h - \nu\|_{L^2} \|\nu_h \cdot (\hat{X}_t - \hat{Y}_{ht})\|_{L^2} \\
&\quad + C(1 - \alpha) \|(\nu_h - \nu) \cdot \tau_h\|_{L^2} \|\tau_h \cdot (\hat{X}_t - \hat{Y}_{ht})\|_{L^2},
\end{aligned}$$

where  $\tau_h$  denotes the vector field given by  $\tau_h := \hat{X}_{h\theta}/|\hat{X}_{h\theta}|$ . Since  $\hat{X}_h \in \mathcal{B}_h$ , the estimate  $\|\hat{X}_\theta - \hat{X}_{h\theta}\|_{L^2} \leq Ke^{\frac{M}{2\alpha}t}h$  holds for all  $0 \leq t \leq T$ . It is then not difficult to estimate  $\|\nu_h - \nu\|_{L^2} \leq CK e^{\frac{M}{2\alpha}t}h$ . Using Young's inequality we deduce

$$\begin{aligned}
A &\leq Ch\alpha \|\hat{X}_t - \hat{Y}_{ht}\|_{L^2} + Ch(1 - \alpha) \|\nu_h \cdot (\hat{X}_t - \hat{Y}_{ht})\|_{L^2} \\
&\quad + Ch \|\hat{X}_t\|_{H^{2,2}} \|\hat{X}_\theta - \hat{Y}_{h\theta}\|_{L^2} + Ch^2 Ke^{\frac{M}{2\alpha}t} + Ch\alpha Ke^{\frac{M}{2\alpha}t} \|\hat{X}_t - \hat{Y}_{ht}\|_{L^2} \\
&\quad + Ch(1 - \alpha) Ke^{\frac{M}{2\alpha}t} \|\nu_h \cdot (\hat{X}_t - \hat{Y}_{ht})\|_{L^2} \\
&\quad + C(1 - \alpha) \|(\nu_h - \nu) \cdot \tau_h\|_{L^2} \|\tau_h \cdot (\hat{X}_t - \hat{Y}_{ht})\|_{L^2} \\
&\leq \frac{Ch^2\alpha}{2\delta_1} + \frac{\delta_1}{2} \alpha \|\hat{X}_t - \hat{Y}_{ht}\|_{L^2}^2 + \frac{Ch^2(1 - \alpha)}{2\delta_2} + \frac{\delta_2}{2} (1 - \alpha) \|\nu_h \cdot (\hat{X}_t - \hat{Y}_{ht})\|_{L^2}^2 \\
&\quad + \frac{Ch^2}{2\delta_3} \|\hat{X}_t\|_{H^{2,2}}^2 + \frac{\delta_3}{2} \|\hat{X}_\theta - \hat{Y}_{h\theta}\|_{L^2}^2 + Ch^2 Ke^{\frac{M}{2\alpha}t} + \frac{Ch^2\alpha Ke^{\frac{M}{\alpha}t}}{2\delta_4} + \frac{\delta_4}{2} \alpha \|\hat{X}_t - \hat{Y}_{ht}\|_{L^2}^2 \\
&\quad + \frac{Ch^2(1 - \alpha) Ke^{\frac{M}{\alpha}t}}{2\delta_5} + \frac{\delta_5}{2} (1 - \alpha) \|\nu_h \cdot (\hat{X}_t - \hat{Y}_{ht})\|_{L^2}^2 \\
&\quad + C(1 - \alpha) \|(\nu_h - \nu) \cdot \tau_h\|_{L^2} \|\tau_h \cdot (\hat{X}_t - \hat{Y}_{ht})\|_{L^2}.
\end{aligned}$$

By choosing the constants  $\delta_i > 0$ , for  $i = 1, \dots, 5$ , appropriately, it follows that

$$\begin{aligned}
&\frac{c_0^2}{8} \alpha \|\hat{X}_t - \hat{Y}_{ht}\|_{L^2}^2 + \frac{c_0^2}{8} (1 - \alpha) \|\nu_h \cdot (\hat{X}_t - \hat{Y}_{ht})\|_{L^2}^2 + \frac{1}{2} \frac{d}{dt} \|\hat{X}_\theta - \hat{Y}_{h\theta}\|_{L^2}^2 \\
&\leq Ch^2(1 + \|\hat{X}_t\|_{H^{2,2}}^2) + \frac{1}{2} \|\hat{X}_\theta - \hat{Y}_{h\theta}\|_{L^2}^2 + Ch^2 Ke^{\frac{M}{\alpha}t} \\
&\quad + C(1 - \alpha) \|(\nu_h - \nu) \cdot \tau_h\|_{L^2} \|\tau_h \cdot (\hat{X}_t - \hat{Y}_{ht})\|_{L^2}.
\end{aligned}$$

We now estimate the last term on the right hand side. This term is the reason for the dependence of the approximation error on  $\alpha$ . Using the estimate  $\|\nu_h - \nu\|_{L^2} \leq CK e^{\frac{M}{2\alpha}t}h$  and Young's



inequality, we obtain

$$\begin{aligned}
& \frac{c_0^2}{4} \alpha \|\hat{X}_t - \hat{Y}_{ht}\|_{L^2}^2 + \frac{c_0^2}{4} (1 - \alpha) \|\nu_h \cdot (\hat{X}_t - \hat{Y}_{ht})\|_{L^2}^2 + \frac{d}{dt} \|\hat{X}_\theta - \hat{Y}_{h\theta}\|_{L^2}^2 \\
& \leq Ch^2(1 + \|\hat{X}_t\|_{H^{2,2}}^2) + \|\hat{X}_\theta - \hat{Y}_{h\theta}\|_{L^2}^2 + Ch^2K^2e^{\frac{M}{\alpha}t} + C(1 - \alpha)Ke^{\frac{M}{2\alpha}t}h\|\hat{X}_t - \hat{Y}_{ht}\|_{L^2} \\
& \leq Ch^2(1 + \|\hat{X}_t\|_{H^{2,2}}^2) + \|\hat{X}_\theta - \hat{Y}_{h\theta}\|_{L^2}^2 + Ch^2K^2e^{\frac{M}{\alpha}t} + \frac{Ch^2K^2e^{\frac{M}{\alpha}t}}{\alpha} + \frac{c_0^2}{8} \alpha \|\hat{X}_t - \hat{Y}_{ht}\|_{L^2}^2.
\end{aligned}$$

Hence, we have

$$\begin{aligned}
& \frac{c_0^2}{8} \alpha \|\hat{X}_t - \hat{Y}_{ht}\|_{L^2}^2 + \frac{c_0^2}{4} (1 - \alpha) \|\nu_h \cdot (\hat{X}_t - \hat{Y}_{ht})\|_{L^2}^2 + \frac{d}{dt} \|\hat{X}_\theta - \hat{Y}_{h\theta}\|_{L^2}^2 \\
& \leq Ch^2(1 + \|\hat{X}_t\|_{H^{2,2}}^2) + \|\hat{X}_\theta - \hat{Y}_{h\theta}\|_{L^2}^2 + \frac{Ch^2K^2e^{\frac{M}{\alpha}t}}{\alpha}. \tag{3.7}
\end{aligned}$$

Integrating with respect to time and using the fact that  $\hat{X}_t \in L^2((0, T), H^{2,2}(\mathbb{R}/2\pi))$  leads to

$$\begin{aligned}
\|(\hat{X}_\theta - \hat{Y}_\theta)(t)\|_{L^2}^2 & \leq \|(\hat{X}_\theta - \hat{Y}_\theta)(0)\|_{L^2}^2 + Ch^2 + \frac{Ch^2K^2e^{\frac{M}{\alpha}t}}{M} + \int_0^t \|(\hat{X}_\theta - \hat{Y}_{h\theta})(s)\|_{L^2}^2 ds \\
& \leq Ch^2 + \frac{Ch^2K^2e^{\frac{M}{\alpha}t}}{M} + \int_0^t \|(\hat{X}_\theta - \hat{Y}_{h\theta})(s)\|_{L^2}^2 ds,
\end{aligned}$$

where we have used  $X(\cdot, 0) = X_0(\cdot)$  and  $\hat{Y}_h(\cdot, 0) = (I_h X_0)(\cdot)$  as well as  $\|(X_0 - (I_h X_0))_\theta\|_{L^2} \leq Ch$ . We infer from Gronwall's lemma that

$$\|(\hat{X}_\theta - \hat{Y}_\theta)(t)\|_{L^2}^2 \leq Ch^2e^t + \frac{Ch^2K^2e^{(\frac{M}{\alpha}+1)t}}{M},$$

and hence,

$$\sup_{t \in [0, T]} e^{-\frac{M}{\alpha}t} \|(\hat{X}_\theta - \hat{Y}_{h\theta})(t)\|_{L^2}^2 \leq Ch^2 + \frac{Ch^2K^2}{M},$$

where  $C$  depends on  $\hat{X}$  and  $T$ . Choosing  $K^2 \geq 2C$  and  $M \geq 2C$  we can finally conclude that

$$\sup_{t \in [0, T]} e^{-\frac{M}{\alpha}t} \|(\hat{X}_\theta - \hat{Y}_{h\theta})(t)\|_{L^2}^2 \leq \frac{K^2h^2}{2} + \frac{C}{M}K^2h^2 \leq K^2h^2$$

and thus,  $\hat{Y}_h \in \mathcal{B}_h$ . The maximal grid size  $h_0$  then only depends on  $\hat{X}, T$  and  $\alpha$ . Inserting the estimate  $\|(\hat{X}_\theta - \hat{Y}_{h\theta})(t)\|_{L^2}^2 \leq K^2h^2e^{\frac{M}{\alpha}t}$  into (3.7) gives

$$\begin{aligned}
& \frac{c_0^2}{8} \alpha \|\hat{X}_t - \hat{Y}_{ht}\|_{L^2}^2 + \frac{c_0^2}{4} (1 - \alpha) \|\nu_h \cdot (\hat{X}_t - \hat{Y}_{ht})\|_{L^2}^2 + \frac{d}{dt} \|\hat{X}_\theta - \hat{Y}_{h\theta}\|_{L^2}^2 \\
& \leq Ch^2(1 + \|\hat{X}_t\|_{H^{2,2}}^2) + \frac{Ch^2K^2e^{\frac{M}{\alpha}t}}{\alpha}.
\end{aligned}$$

The same procedure as above then shows that

$$\begin{aligned}
& \frac{c_0^2}{8} \alpha \int_0^t \|(\hat{X}_t - \hat{Y}_{ht})(t)\|_{L^2}^2 dt + \frac{c_0^2}{4} (1 - \alpha) \int_0^t \|\nu_h \cdot (\hat{X}_t - \hat{Y}_{ht})(t)\|_{L^2}^2 dt + \|(\hat{X}_\theta - \hat{Y}_{h\theta})(t)\|_{L^2}^2 \\
& \leq Ch^2 + \frac{Ch^2K^2e^{\frac{M}{\alpha}t}}{M}.
\end{aligned}$$

and hence,

$$\begin{aligned}
& \alpha \int_0^T \|(\hat{X}_t - \hat{Y}_{ht})(t)\|_{L^2}^2 dt + (1 - \alpha) \int_0^T \|\nu_h \cdot (\hat{X}_t - \hat{Y}_{ht})(t)\|_{L^2}^2 dt + \max_{t \in [0, T]} \|(\hat{X}_\theta - \hat{Y}_{h\theta})(t)\|_{L^2}^2 \\
& \leq Ce^{\frac{M}{\alpha}T}h^2, \tag{3.8}
\end{aligned}$$

where  $C$  and  $M$  depends on  $\hat{X}$  and  $T$ . In particular, we have  $\int_0^T \|\hat{Y}_{ht}\|_{L^2}^2 dt \leq C(\alpha, h, T, \hat{X})$ . Together with  $\hat{Y}_h(\cdot, 0) = (I_h X_0)(\cdot)$  on  $[0, 2\pi]$ , this implies that  $\|\hat{Y}_h\|_{H^{1,2}((0, T), \mathcal{S}_h)} \leq C(\alpha, h, T, \hat{X})$ .

This completes the proof of the fact that  $F(\mathcal{B}_h) \subset \mathcal{B}_h$  is precompact. We can now apply the Schauder fixed point theorem. The error estimate for the solution to the semi-discrete flow (3.3), that is for the fixed point  $\hat{X}_h = F(\hat{X}_h)$ , finally infers from (3.8) and the fact that

$$\begin{aligned} \max_{t \in [0, T]} \|(\hat{X} - \hat{X}_h)(t)\|_{L^2}^2 &\leq C \|(\hat{X} - \hat{X}_h)(0)\|_{L^2}^2 + CT \int_0^T \|(\hat{X}_t - \hat{X}_{ht})(t)\|_{L^2}^2 dt \\ &\leq C \|(\hat{X} - I_h \hat{X})(0)\|_{L^2}^2 + CT \int_0^T \|(\hat{X}_t - \hat{X}_{ht})(t)\|_{L^2}^2 dt \\ &\leq Ch^4 + CT \int_0^T \|(\hat{X}_t - \hat{X}_{ht})(t)\|_{L^2}^2 dt. \end{aligned}$$

□

**Remark 2.** In the above theorem we have excluded the case  $\alpha > 1$ , since we are mainly interested in the behaviour of the reparametrized flow for small  $\alpha$  anyway. However, this restriction is clearly only a formal one. To be more precise, the proof for  $\alpha > 1$  works by writing the map  $\alpha \mathbf{1} + (1 - \alpha)\nu_h \otimes \nu_h$  as  $\alpha\tau_h \otimes \tau_h + \nu_h \otimes \nu_h$ , where  $\tau_h = \hat{X}_{h\theta}/|\hat{X}_{h\theta}|$  is a unit tangential vector field.

**Remark 3.** Unfortunately, for the case  $\alpha \searrow 0$  the error estimate in Theorem 2 becomes unbounded. It is therefore not clear whether for the choice  $\alpha = 0$ , the approximation error still converges to zero for  $h \searrow 0$ . This is an open question.

**Remark 4.** If we choose  $\varphi_h = \hat{X}_{ht}$  in (3.3) and integrate in time, we obtain the following stability estimate for the semi-discrete scheme

$$\frac{1}{2} \int_0^{2\pi} |\hat{X}_{h\theta}(\cdot, T)|^2 d\theta + \int_0^T \int_0^{2\pi} \left( \alpha |\hat{X}_{ht}|^2 + (1 - \alpha) |\hat{X}_{ht} \cdot \nu_h|^2 \right) |\hat{X}_{h\theta}|^2 d\theta = \frac{1}{2} \int_0^{2\pi} |\hat{X}_{h\theta}(\cdot, 0)|^2 d\theta.$$

### 3.3 Numerical scheme for the curve shortening flow

Time discretization of the semi-discrete scheme (3.3) leads to a family of algorithms for the computation of the curve shortening. Using the notation  $f^m = f(\cdot, m\tau)$  for the discrete time levels  $\{m\tau \mid m = 0, \dots, M_\tau \in \mathbb{N}\}$  with time step size  $\tau > 0$  and  $M_\tau\tau < T$ , we propose the following semi-implicit schemes.

**Algorithm 1.** Let  $\alpha \in (0, \infty)$ . For a given initial polygonal curve  $\Gamma_h^0 = \hat{X}_h^0([0, 2\pi])$  with  $\hat{X}_h^0 \in \mathcal{S}_h^2$ , determine for  $m = 0, \dots, M_\tau - 1$  the periodic solution  $\hat{X}_h^{m+1} \in \mathcal{S}_h^2$  of

$$\begin{aligned} &\int_0^{2\pi} \left( \frac{\alpha}{\tau} \hat{X}_h^{m+1} \cdot \varphi_h + \frac{1 - \alpha}{\tau} (\hat{X}_h^{m+1} \cdot \nu_h^m)(\nu_h^m \cdot \varphi_h) \right) |\hat{X}_{h\theta}^m|^2 d\theta + \int_0^{2\pi} \hat{X}_{h\theta}^{m+1} \cdot \varphi_h d\theta \\ &= \int_0^{2\pi} \left( \frac{\alpha}{\tau} \hat{X}_h^m \cdot \varphi_h + \frac{1 - \alpha}{\tau} (\hat{X}_h^m \cdot \nu_h^m)(\nu_h^m \cdot \varphi_h) \right) |\hat{X}_{h\theta}^m|^2 d\theta, \quad \forall \varphi \in \mathcal{S}_h^2, \end{aligned}$$

where  $\nu_h^m$  is a piecewise constant unit normal field to the polygonal curve  $\Gamma_h^m$ , and set

$$\Gamma_h^{m+1} := \hat{X}_h^{m+1}([0, 2\pi]).$$

**Remark 5.** If we choose  $\varphi_h = \hat{X}_h^{m+1} - \hat{X}_h^m$ , we obtain after a short calculation

$$\begin{aligned} &\frac{1}{2} \int_0^{2\pi} |\hat{X}_{h\theta}^M|^2 d\theta + \sum_{m=0}^{M-1} \int_0^{2\pi} \left( \frac{\alpha}{\tau} |\hat{X}_h^{m+1} - \hat{X}_h^m|^2 + \frac{1 - \alpha}{\tau} |(\hat{X}_h^{m+1} - \hat{X}_h^m) \cdot \nu_h^m|^2 \right) |\hat{X}_{h\theta}^m|^2 d\theta \\ &\leq \frac{1}{2} \int_0^{2\pi} |\hat{X}_{h\theta}^0|^2 d\theta \end{aligned}$$

This holds for all mesh sizes  $h > 0$  and time steps  $\tau > 0$ .

It is formally possible to choose  $\alpha = 0$  in Algorithm 1, although this case was excluded in the derivation of the reparametrized curve shortening flow. The algorithm (2.16a) in [5], which we have cited in the introduction, is in this spirit.

## 4 Numerical results for the curve shortening flow

In order to implement Algorithm 1 we solve the following linear system of equations within the Finite Element Toolbox ALBERTA, see [28],

$$\frac{1}{\tau} \sum_{\gamma=1}^2 \sum_{j=1}^N M_{ij\beta\gamma} \hat{\mathbf{X}}^{j\gamma} + \sum_{\gamma=1}^2 \sum_{j=1}^N S_{ij\beta\gamma} \hat{\mathbf{X}}^{j\gamma} = \frac{1}{\tau} \sum_{\gamma=1}^2 \sum_{j=1}^N M_{ij\beta\gamma} \hat{\mathbf{X}}_{old}^{j\gamma}, \quad \forall i = 1, \dots, N, \beta = 1, 2, \quad (4.1)$$

where  $\hat{X}_h^{m+1} = \sum_{\gamma=1}^2 \sum_{j=1}^N \hat{\mathbf{X}}^{j\gamma} \phi_j e_\gamma$  is the unknown parametrization of the polygonal curve and  $\hat{X}_h^m = \sum_{\gamma=1}^2 \sum_{j=1}^N \hat{\mathbf{X}}_{old}^{j\gamma} \phi_j e_\gamma$  is the solution from the previous time step. The mass matrix  $M := (M_{ij\beta\gamma}) \in \mathbb{R}^{(2N) \times (2N)}$  and the stiffness matrix  $S := (S_{ij\beta\gamma}) \in \mathbb{R}^{(2N) \times (2N)}$  are assembled by summing up all simplex matrices  $(M_{ij\beta\gamma}(T))$  and  $(S_{ij\beta\gamma}(T))$  given by

$$M_{ij\beta\gamma}(T) = (\alpha \delta_{\beta\gamma} |\rho_h^m(T)|^2 + (1 - \alpha) \rho_{h\beta}^m(T) \rho_{h\gamma}^m(T)) \int_T \phi_i(\theta) \phi_j(\theta) d\theta,$$

$$S_{ij\beta\gamma}(T) = \delta_{\beta\gamma} \int_T \phi_{i\theta}(\theta) \phi_{j\theta}(\theta) d\theta.$$

Here,  $\phi_i$  and  $\phi_j$  denote the local basis functions of the simplex  $T$  and  $\rho_h^m(T)$  is the constant vector field  $\hat{X}_{h\theta}^m|_T$  rotated by 90 degrees. The linear system (4.1) can be solved by the conjugate gradient method. The initial polygonal curve of the simulation is constructed by mapping the vertices of a triangulation of the unit sphere onto an initial smooth curve via a problem dependent map. We compare the performance of Algorithm 1 to the benchmark scheme (2.16a) of [5]. This fully-implicit scheme is solved by the fixed point iteration defined in (3.3a) of [5] with the suggested stopping criteria  $\|\hat{X}_h^{m+1,i+1} - \hat{X}_h^{m+1,i}\|_\infty < 10^{-8}$ . In order to solve the linear system (3.3a) in [5], we apply the conjugate gradient method.

### Example 1:

The first example is presented in Figure 1. The initial curve is given by the parametrization

$$X_0(\theta) := \begin{pmatrix} \cos \theta \\ (0.9 \cos^2 \theta + 0.1) \sin \theta \end{pmatrix}, \quad \theta \in [0, 2\pi).$$

Under the curve shortening flow, this curve shrinks to a round circle, which is clearly visible in Figure 1d. We here want to demonstrate that our scheme is not only able to maintain the mesh quality but also to improve it significantly. We therefore start with non-equidistributed meshes. Whether it is appropriate for the BGN-scheme (2.16a) of [5] to start with a non-equidistributed mesh is discussed in Example 3. Figure 2 shows the decrease of the length of the evolving curve. The BGN-scheme (2.16a) of [5] seems to lead to a slightly stronger drop of the curve length in the first time step. This is probably due to the fact that the BGN-scheme changes the mesh in the first time step such that the segments of the polygonal curve are equally long. The ratio of the maximal to the minimal segment length is therefore equal to 1 after the first time step. However, also Algorithm 1 leads to length ratios that are close to 1, provided that the parameter  $\alpha$  is chosen sufficiently small, see Figure 3. The main difference between the BGN-scheme and the  $\alpha$ -scheme is that the redistributions of the mesh vertices do not occur instantaneously under Algorithm 1. Moreover, the mesh ratio does not exactly stick to 1, which gives Algorithm 1 a bit more flexibility. In Example 2, it will turn out that this can be advantageous in certain circumstances. Since the BGN-scheme is a fully-implicit scheme, we have to solve a non-linear system of algebraic equations in each time step. We solve this system by the fixed point iteration proposed in (3.3a) of [5]. Apart from the first time step and the time step at the end of the simulation, where the round circle in Figure 1d actually drops to a point, the fixed point iteration converges rather fast, see Figure 4. The initial redistribution of the vertices in both schemes is associated with a large initial (tangential) velocity. Since for Algorithm 1 the redistribution of the mesh vertices occurs on a time scale determined by the parameter  $\alpha$ , smaller values of  $\alpha$  lead to a larger maximal initial velocity, see Figure 5. However, in contrast to the BGN-scheme, the maximal initial velocity of Algorithm 1 is bounded for different choices of the time step size  $\tau$ , see Figure 6. The fact that the maximal initial velocity in the BGN-scheme depends linearly on the inverse time step size  $\tau^{-1}$  is associated with the relatively large jumps of the mesh vertices in the first time step, see Figure 7. Since these jumps must lead to an equidistributed mesh, their

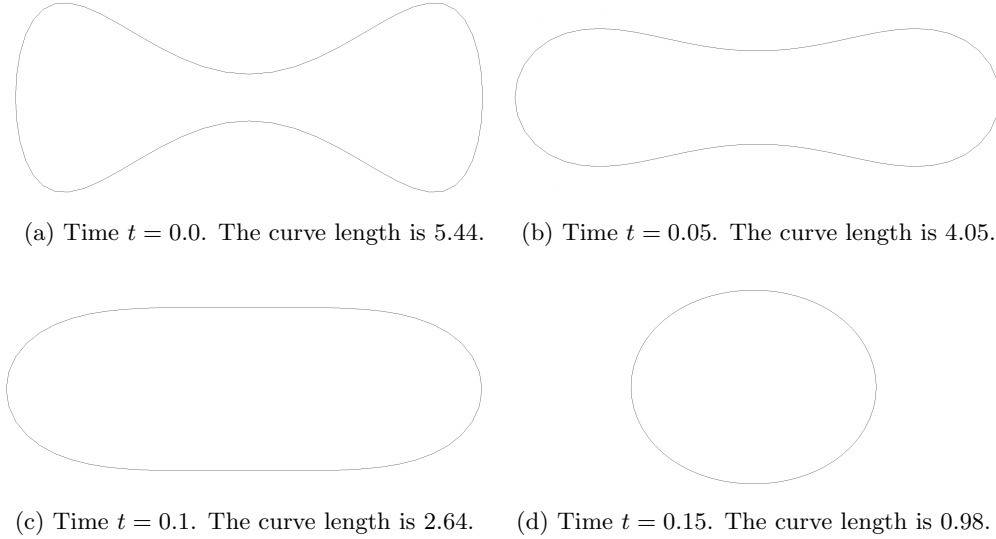


Figure 1: Simulation of the curve shortening flow with Algorithm 1 for  $\alpha = 10^{-3}$  and time step size  $\tau = 10^{-4}$ . The computational mesh had 64 vertices. The simulation clearly shows that the curve shrinks to a round circle whose length converges to zero. The images are rescaled. See Example 1 of Section 4 for further details.

size cannot become small even for small time step sizes  $\tau$ . This issue will be further discussed in Example 3. Interestingly, the  $\alpha$ -scheme seems to interpolate the initial jump of the vertices in the BGN-scheme, see Figure 7.

### Example 2:

We now consider the curve shortening flow for the initial curve given by the parametrization

$$X_0(\theta) := \begin{pmatrix} \cos(2\theta) \cos \theta \\ \cos(2\theta) \sin \theta \end{pmatrix}, \quad \theta \in [0, 2\pi),$$

see Figure 8a for a visualization. The simulation based on Algorithm 1 with  $\alpha = 10^{-3}$  shows that the curve shortening flow develops a singularity, see Figure 8d, at time  $t \approx 0.0828$ . Beyond this singularity, see Figures 8e and 8f, the curve shrinks to a round circle. Note that this example does not satisfy the regularity assumptions made in Theorem 2. Since the fixed point iteration used to solve the non-linear system of equations arising in the BGN-scheme stops to converge at the curve singularity shown in Figure 8d, see Figure 11 for the number of iteration steps in the fixed point iteration, it is not possible to compute the curve shortening flow through this singularity by the fixed point iteration we used for the BGN-scheme; also note the remark below. Figure 10 shows that at this singularity the ratio between the maximal and minimal segment length of the  $\alpha$ -scheme increases very fast before it decreases again. It is this flexibility which seems to be advantageous in this example. Apart from the singularities the  $\alpha$ -scheme shows again good mesh properties provided that  $\alpha$  is sufficiently small. The decrease of the curve length is presented in Figure 9. We here only report that by using a damped fixed point iteration in the BGN-scheme, the solver converges for mild damping parameters also at the singularity of the curve shortening flow; see also the remark at the end of Example 3.

### Example 3:

In this example, we demonstrate that the employed fixed point iteration for the BGN-scheme might not only fail at curve singularities as in Example 2. In fact, the problem also occurs for the most simple case, that is the unit circle, if the segment length of the initial triangulation is not constant and if the time step size  $\tau$  is smaller than a critical value. To start with non-equidistributed meshes might be indeed desirable for certain applications. Other algorithms like the scheme in [9] and the scheme (2.3) in [2], are expected to be more appropriate to handle non-equidistributed initial meshes than the BGN-scheme (2.16a) from [5]. In fact, it is an interesting

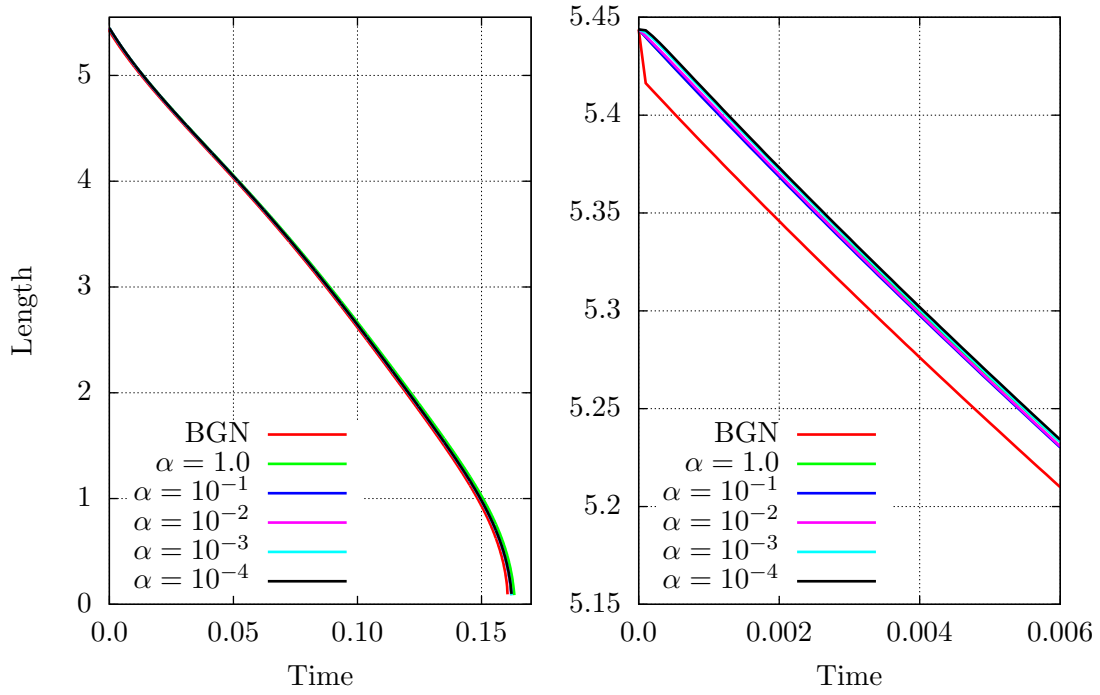


Figure 2: The images show the decrease of the curve length under the curve shortening flow for the BGN-scheme (2.16a) in [5] and for Algorithm 1 for different choices of  $\alpha$ . The initial curve is shown in Figure 1a. The time step size was chosen as  $\tau = 10^{-4}$ . The right image shows an enlarged section for small times  $t$ . Due to the equidistribution property of the BGN-scheme, this scheme leads to a slightly stronger drop of the curve length in the first time step. See Example 1 of Section 4 for further details.

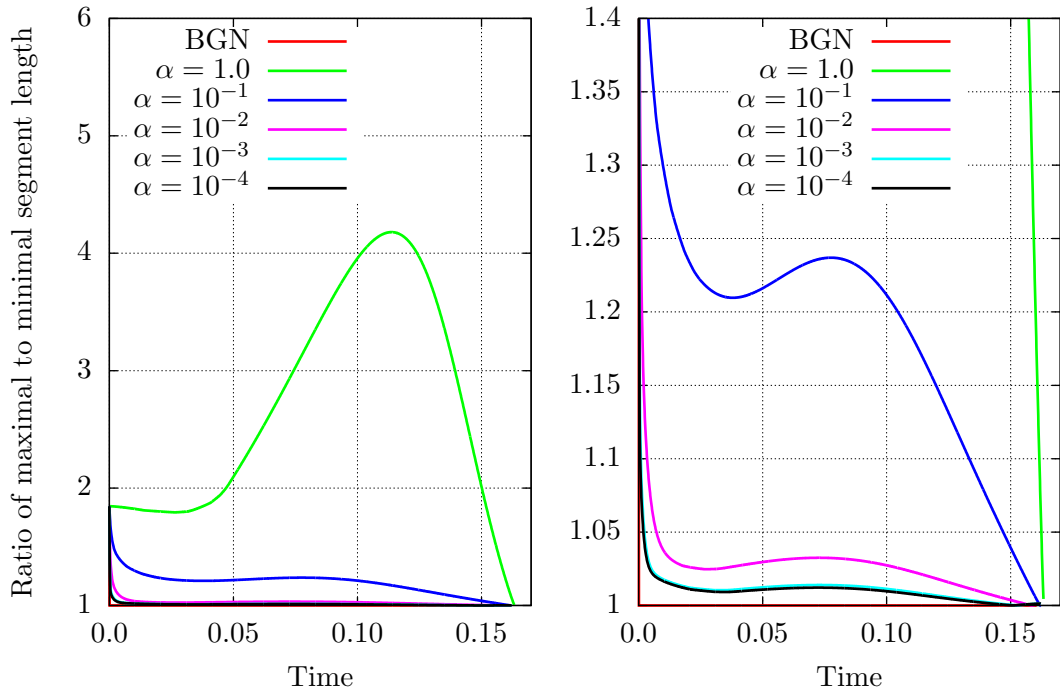


Figure 3: The images show the ratio of the maximal to the minimal segment length for the BGN-scheme (2.16a) in [5] and for Algorithm 1 for different choices of  $\alpha$ . The initial curve is shown in Figure 1a. The right image shows an enlarged section. Due to the equidistribution property of the BGN-scheme, the ratio of the maximal to the minimal segment length is equal to 1 after the first time step. However, the images clearly show that also Algorithm 1 has good properties with respect to the mesh quality provided that  $\alpha$  is chosen sufficiently small. The mesh properties of Algorithm 1 seemed to be (almost) independent of the choice of  $\tau$  if  $\tau \leq 10^{-4}$  (not shown in the picture). See Example 1 of Section 4 for further details.

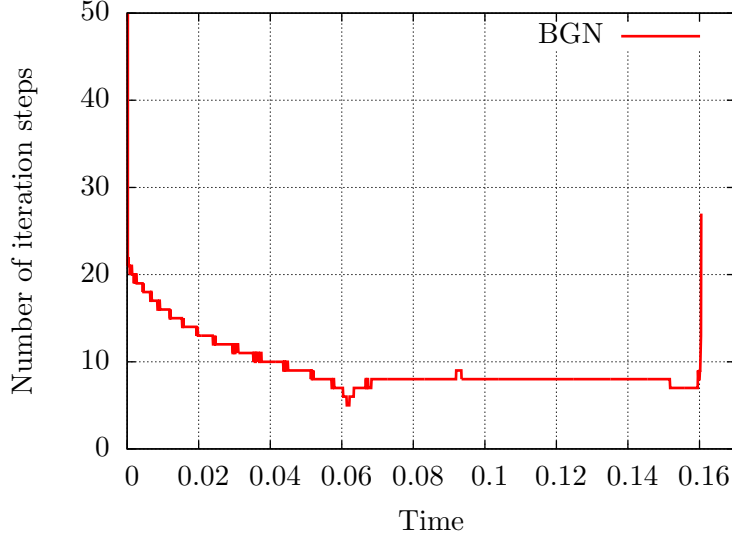


Figure 4: The image shows the number of iteration steps of the fixed point iteration that are necessary to solve the non-linear system of equations which arises in the fully-implicit BGN-scheme (2.16) in [5]. The fixed point iteration was stopped if for all vertices of the discrete curve the distance between the position vectors does not change more than  $10^{-8}$  in one iteration step. The image shows that apart from the first time step and the time step at the end of the simulation the fixed point iteration converges rather fast. See Example 1 of Section 4 for further details.

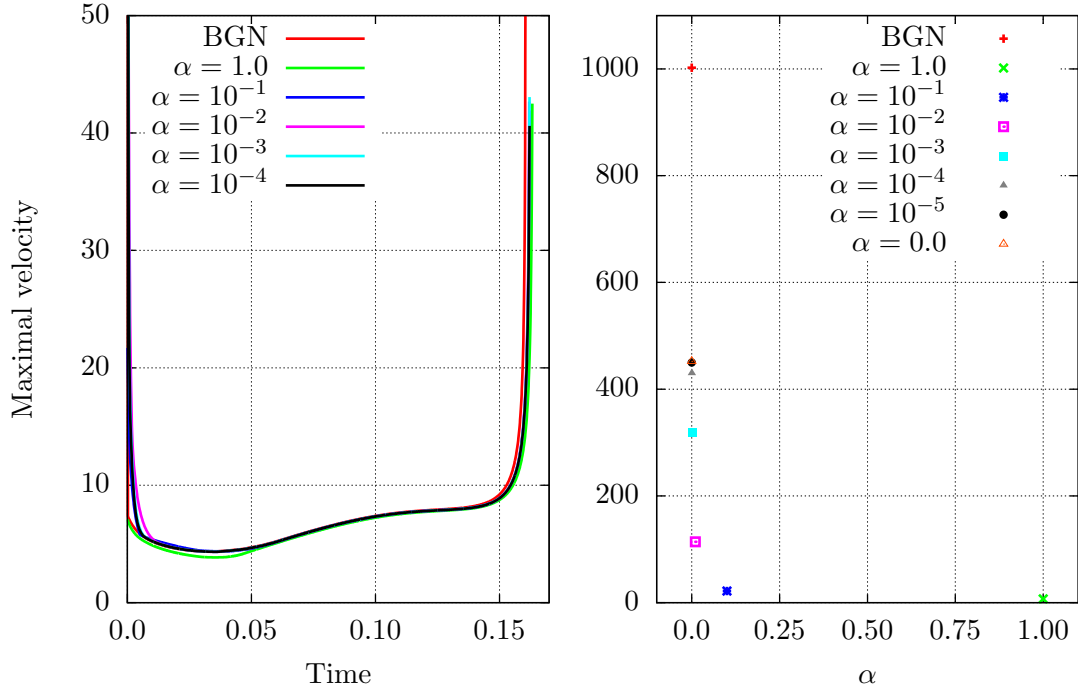


Figure 5: Comparison of the maximal velocity of the vertices for the BGN-scheme (2.16a) in [5] and for Algorithm 1 for different choices of  $\alpha$ . The initial curve of the simulation is shown in Figure 1a. The time step size was  $\tau = 10^{-4}$ . The left image shows the maximal velocity of all vertices as a function of time  $t$ . The right image shows how the maximal velocity of the vertices at time  $t = 0$  depends on the parameter  $\alpha$ . The maximal initial velocity of the BGN-scheme is clearly higher than the maximal initial velocity of the  $\alpha$ -schemes. In fact, Figure 6 shows that the maximal initial velocity of the BGN-scheme as a function of the inverse time step size  $\tau^{-1}$  is unbounded. See Example 1 of Section 4 for further details.

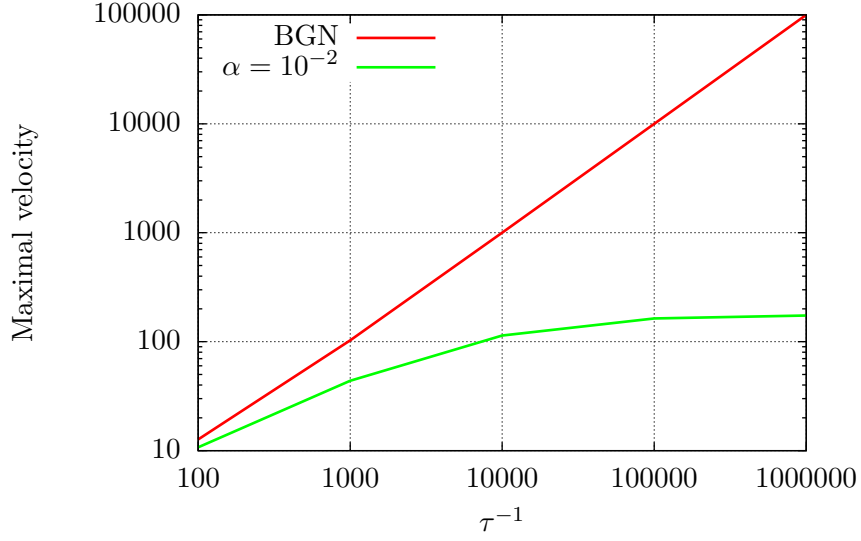


Figure 6: The image shows the maximal initial velocity of the BGN-scheme (2.16a) in [5] and of Algorithm 1 with  $\alpha = 10^{-2}$  as a function of the inverse time step size  $\tau^{-1}$ . The linear growth of the maximal initial velocity of the BGN-scheme is due to the finite jumps of the vertices in the first time step, see Figure 7. In contrast, the maximal initial velocity of the  $\alpha$ -scheme is bounded. See Example 1 of Section 4 for further details.

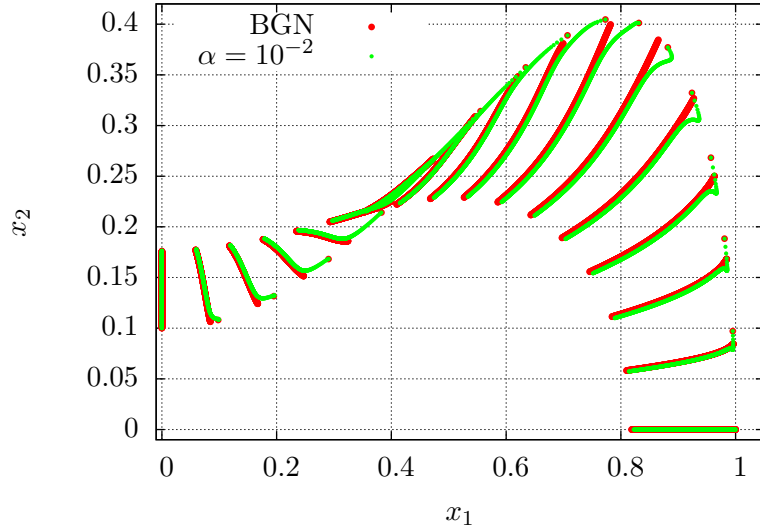
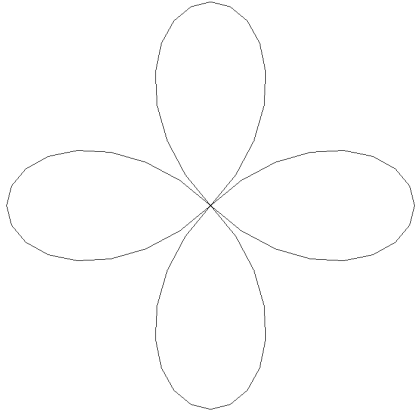
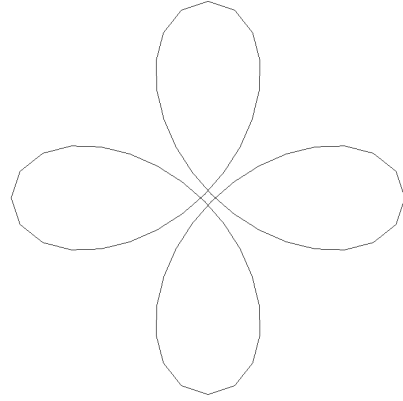


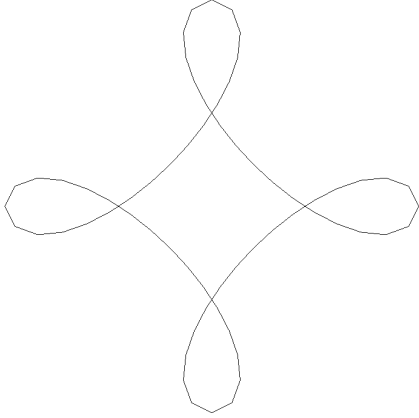
Figure 7: The image shows the motion of the curve vertices for the BGN-scheme (2.16a) in [5] and for Algorithm 1 with  $\alpha = 10^{-2}$ . Only the first quadrant is shown for the first time steps of the simulation. The whole initial curve is shown in Figure 1a. The time step size was chosen as  $\tau = 10^{-4}$ . One can clearly see that the BGN-scheme leads to large jumps of the vertices in the first time step. The  $\alpha$ -scheme seems to interpolate between these jumps. See Example 1 of Section 4 for further details.



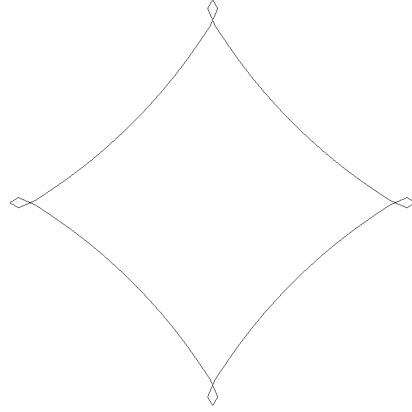
(a) Time  $t = 0.0$ . The curve length is 9.66.



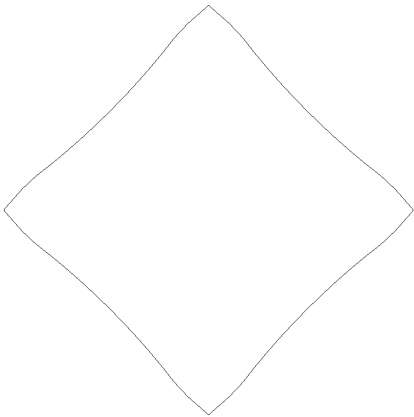
(b) Time  $t = 0.02$ . The curve length is 8.56.



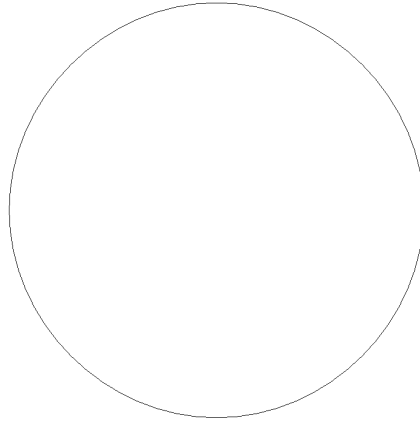
(c) Time  $t = 0.08$ . The curve length is 2.66.



(d) Time  $t = 0.0828$ . The curve length is 1.12.



(e) Time  $t = 0.0829$ . The curve length is 0.86.



(f) Time  $t = 0.086$ . The curve length is 0.56.

Figure 8: Simulation of the curve shortening flow with Algorithm 1 for  $\alpha = 10^{-3}$  and time step size  $\tau = 10^{-4}$ . The computational mesh had 64 vertices. The images are rescaled. A comparison with the BGN-scheme (2.16a) in [5] shows that the fixed point iteration used to solve the fully-implicit BGN-scheme stops to converge at the singularity shown in Figure 8d.



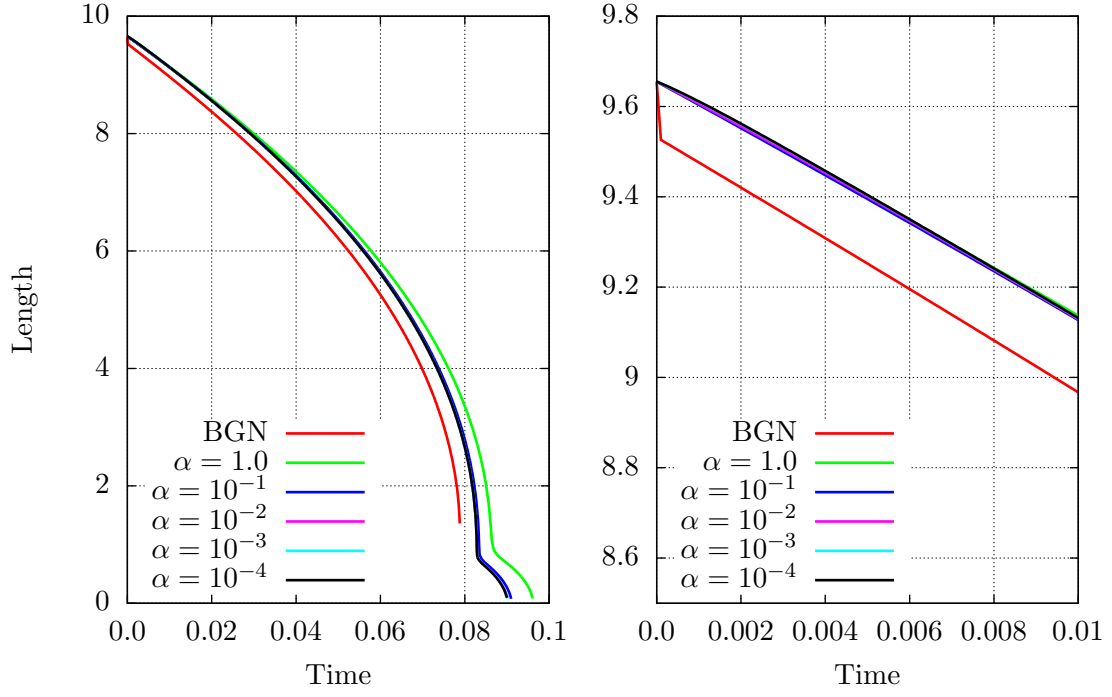


Figure 9: The images show the decrease of the curve length under the curve shortening flow for the BGN-scheme (2.16a) in [5] and for Algorithm 1 for different choices of  $\alpha$ . The initial curve is shown in Figure 8a. The time step size was chosen as  $\tau = 10^{-4}$ . The fixed point iteration used to solve the BGN-scheme stops to converge at time  $t = 0.0789$ , see Figure 11. The right image shows an enlarged section for small times  $t$ . See Example 2 of Section 4 for further details.

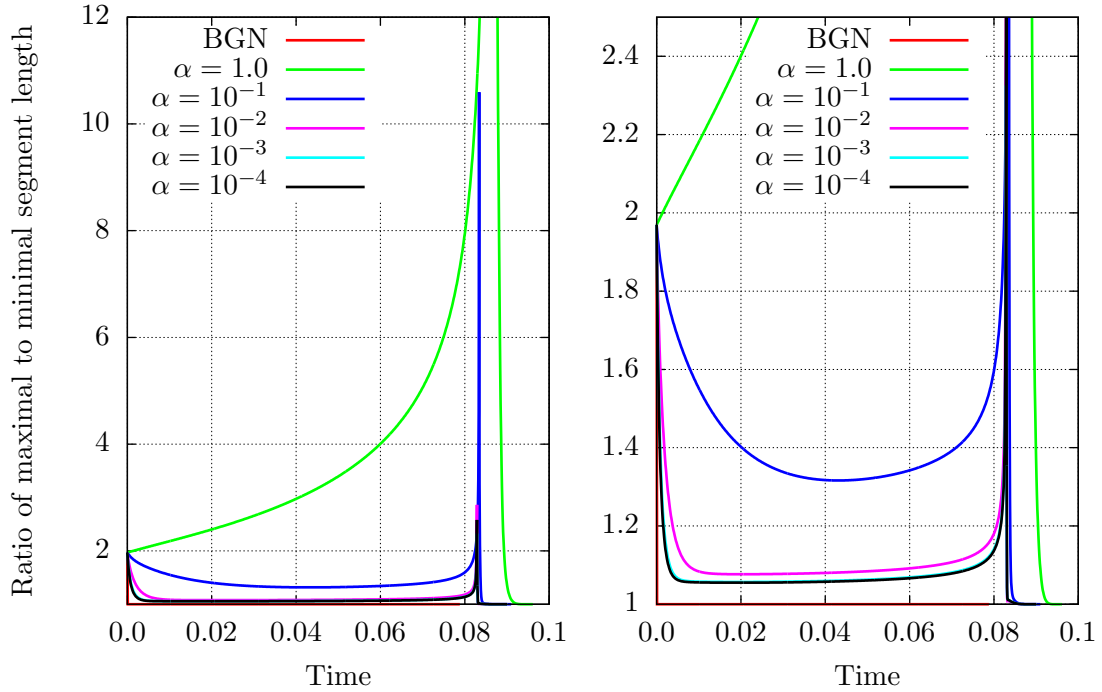


Figure 10: The images show the ratio of the maximal to the minimal segment length for the BGN-scheme (2.16a) in [5] and for Algorithm 1 for different choices of  $\alpha$ . The initial curve is shown in Figure 8a. The right image shows an enlarged section. The simulation shows that Algorithm 1 has good mesh properties for  $\alpha$  sufficiently small. See Example 2 of Section 4 for further details.

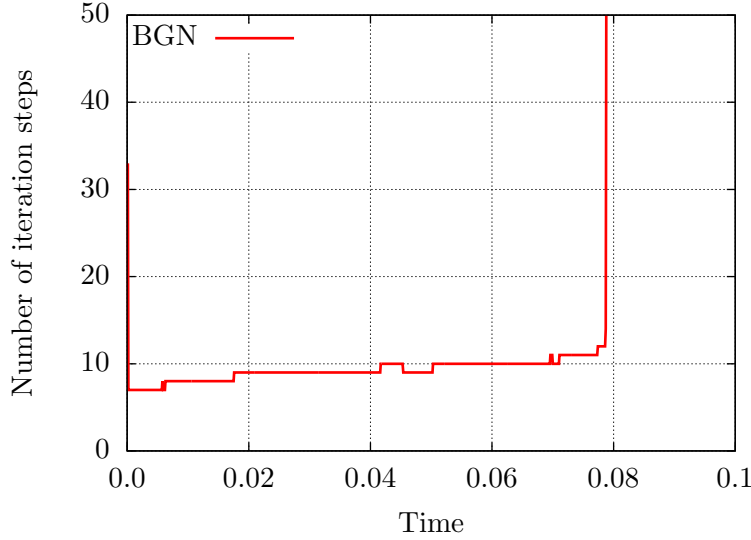


Figure 11: The figure shows the number of iteration steps of the fixed point iteration that are necessary to solve the non-linear system of equations which arises in the fully-implicit BGN-scheme (2.16) in [5]. The fixed point iteration was stopped if for all vertices of the discrete curve the distance between the position vectors does not change more than  $10^{-8}$  in one iteration step. The initial curve of the simulation is shown in Figure 8a. The fixed point iteration stops to converge at time  $t = 0.0789$  which corresponds to the situation shown in Figure 8d. In Example 3, the fixed point iteration also does not converge for a non-singular curve if the time step size is below a critical value. See Example 2 of Section 4 for further details.

question how the latter scheme behaves for initially non-equidistributed meshes. Since the BGN-scheme (2.16a) plays an important role in this paper, we will address this question now in more detail. In this example, the curve shortening flow is computed for the initial triangulation shown in Figure 12. The vertices of this triangulation are distributed in such a way that the segment length slowly decreases anti-clockwise. Figure 13 shows that the initial jumps of the mesh vertices under the BGN-scheme strongly depend on the time step size  $\tau$ . We experimentally observed that for time step sizes  $\tau \leq 10^{-4}$  the fixed point iteration for solving the first time step of the BGN-scheme does not converge any more. Interestingly, Algorithm 1 with  $\alpha = 10^{-2}$  seems to interpolate the motion of the vertices computed by the BGN-scheme with  $\tau = 10^{-2}$ , see also Figure 7 for a similar behaviour. We finally note that by employing a damped fixed point iteration for the BGN-scheme it is possible to circumvent the reported difficulties. However, we have observed that the solution then strongly depends on the damping parameter.

## 5 The reparametrized mean curvature flow

### 5.1 Weak formulation on the reference manifold $\mathcal{M}$

In this section, we derive a weak formulation of the reparametrized mean curvature flow (2.20). Unfortunately, this flow is not in divergence form. We hence decompose the elliptic operator of (2.20) into a divergence and into a non-divergence part. This can be simply achieved by using identity (2.17)

$$(\alpha \mathbf{1} + (1 - \alpha)(\nu \circ \hat{x}_\alpha) \otimes (\nu \circ \hat{x}_\alpha)) \frac{\partial}{\partial t} \hat{x}_\alpha = \Delta_{\hat{g}_\alpha} \hat{x}_\alpha + (P \circ \hat{x}_\alpha) \text{tr}_{\hat{g}_\alpha} (\nabla^h \nabla \hat{x}_\alpha).$$

The reason why the second term on the right hand side is not in divergence form is that the trace  $\text{tr}_{\hat{g}_\alpha}$  has to be taken with respect to the metric  $\hat{g}_\alpha(t)$ , whereas  $\nabla^h$  is the covariant derivative with respect to the metric  $h$ . By choosing  $h$  appropriately, it is possible to derive an expression for  $(P \circ \hat{x}_\alpha) \text{tr}_{\hat{g}_\alpha} (\nabla^h \nabla \hat{x}_\alpha)$ , which is the product of a first order term and of a second order term that is in divergence form. In this section, we will assume that the reference manifold  $\mathcal{M}$  is an  $n$ -dimensional hypersurface in  $\mathbb{R}^{n+1}$ .

In our weak formulation of the mean curvature-DeTurck flow we will make use of the following representation of the metric  $\hat{g}_\alpha(t)$ . We define  $\hat{G}_\alpha : \mathcal{M} \times [0, T] \rightarrow \mathbb{R}^{(n+1) \times (n+1)}$  by

$$\hat{G}_\alpha(t) := (\nabla_{\mathcal{M}} \hat{x}_\alpha(t))^T \nabla_{\mathcal{M}} \hat{x}_\alpha(t) + \mu \otimes \mu, \quad (5.1)$$

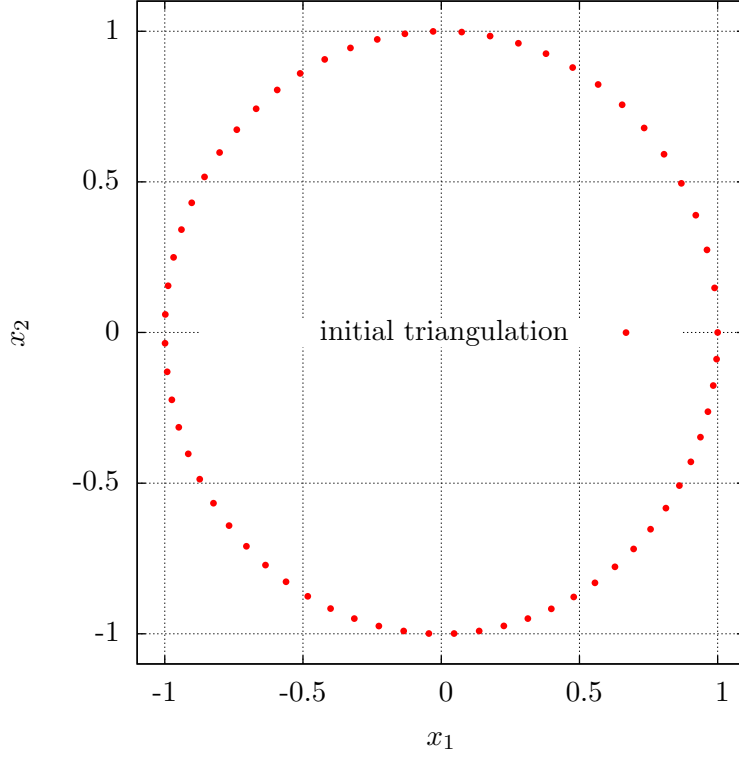


Figure 12: The image shows the 64 vertices of a triangulation of the unit circle. Starting at the point  $(x_1, x_2) = (1, 0)$ , the segment length, that is the length between two vertices, is slowly decreasing anti-clockwise. This leads to a relatively large jump of the segment length between the two segments belonging to the point  $(x_1, x_2) = (1, 0)$ . See Example 3 of Section 4 for further details.

where  $\mu = (\mu_1, \dots, \mu_{n+1})^T$  is a unit normal field to  $\mathcal{M}$ . That this map is indeed a representation of the metric  $\hat{g}_\alpha(t)$  is stated in (5.10) below. The reason, why we have introduced  $\hat{G}_\alpha(t)$ , is the fact that it allows us to represent the metric  $\hat{g}_\alpha(t)$  in global coordinates instead of local ones; see [18] for more details on this kind of representation of metric tensors. Using the global coordinates system of the ambient space will make the spatial discretization of the weak formulation much easier.

**Lemma 2.** *Let  $\alpha \in (0, \infty)$ . Suppose  $\mathcal{M}$  is a smooth,  $n$ -dimensional, closed, connected hypersurface in  $\mathbb{R}^{n+1}$ . Furthermore, let  $h$  be the metric on  $\mathcal{M} \subset \mathbb{R}^{n+1}$  induced by the Euclidean metric  $\mathfrak{e}$  of the ambient space, that is*

$$h_{ij} := \frac{\partial \mathcal{C}_1^{-1}}{\partial \theta^i} \cdot \frac{\partial \mathcal{C}_1^{-1}}{\partial \theta^j}, \quad \text{and} \quad (h^{ij}) := (h_{ij})_{i,j=1,\dots,n}^{-1},$$

where  $\mathcal{C}_1$  is a local coordinate chart of  $\mathcal{M}$ . The mean curvature-DeTurck flow (2.9) then satisfies the following weak formulation

$$\begin{aligned} 0 &= \alpha \int_{\mathcal{M}} \hat{x}_{\alpha t} \cdot \chi \sqrt{\det \hat{G}_\alpha} do_h + (1 - \alpha) \int_{\mathcal{M}} (\hat{x}_{\alpha t} \cdot (\nu \circ \hat{x}_\alpha)) ((\nu \circ \hat{x}_\alpha) \cdot \chi) \sqrt{\det \hat{G}_\alpha} do_h \\ &\quad + \int_{\mathcal{M}} \hat{G}_\alpha^{-1} \nabla_{\mathcal{M}} \hat{x}_\alpha : \nabla_{\mathcal{M}} \chi \sqrt{\det \hat{G}_\alpha} do_h + \int_{\mathcal{M}} ((\nabla_{\mathcal{M}} \hat{x}_\alpha) v_\alpha) \cdot \chi \sqrt{\det \hat{G}_\alpha} do_h, \end{aligned} \quad (5.2)$$

$$0 = \int_{\mathcal{M}} v_\alpha \cdot \xi \sqrt{\det \hat{G}_\alpha} do_h + \int_{\mathcal{M}} \hat{G}_\alpha^{-1} \nabla_{\mathcal{M}} id : \nabla_{\mathcal{M}} \xi \sqrt{\det \hat{G}_\alpha} do_h, \quad (5.3)$$

for all  $\chi, \xi \in H^{1,2}(\mathcal{M}, \mathbb{R}^{n+1})$  and  $t \in (0, T)$ .

*Proof.* A short calculation shows that

$$\hat{g}_\alpha^{ij} \Gamma(h)_{ij}^k = \hat{g}_\alpha^{ij} h^{kl} \left( \frac{\partial h_{li}}{\partial \theta^j} - \frac{1}{2} \frac{\partial h_{ij}}{\partial \theta^l} \right) = \hat{g}_\alpha^{ij} h^{kl} \frac{\partial \mathcal{C}_1^{-1}}{\partial \theta^l} \cdot \frac{\partial^2 \mathcal{C}_1^{-1}}{\partial \theta^i \partial \theta^j}.$$

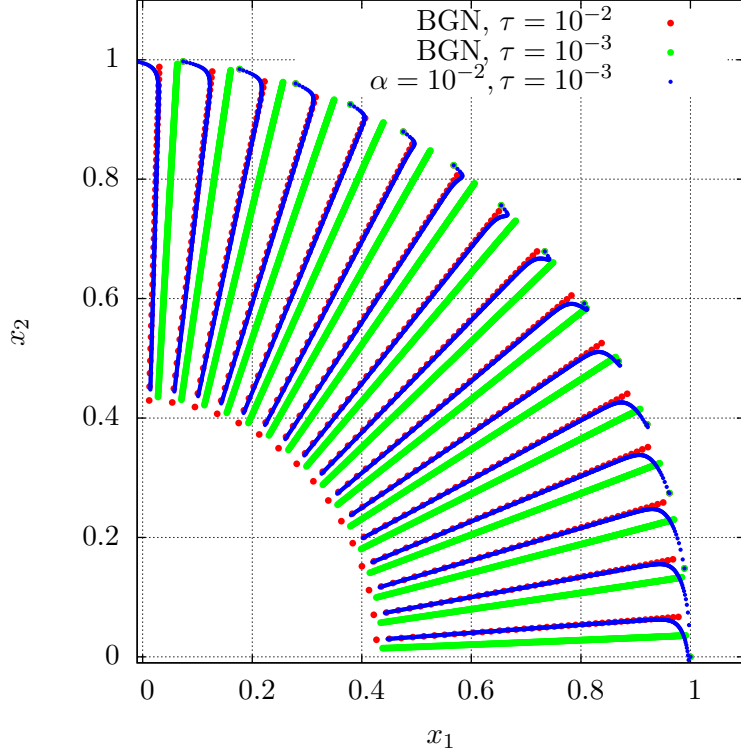


Figure 13: The image shows the motion of the triangulation vertices for the BGN-scheme (2.16a) in [5] and for Algorithm 1 with  $\alpha = 10^{-2}$ . Only the first quadrant is shown. The vertices of the initial triangulation are presented in Figure 12. The time step size was chosen as  $\tau = 10^{-2}$  and  $\tau = 10^{-3}$ . The BGN-scheme leads to relatively large jumps of the vertices in the first time step. The direction of these jumps seems to depend on the time step size (red and green dots). We also observed numerically that the fixed point iteration for the first time step of the BGN-scheme does not converge when the time step size is smaller than a critical value, here for  $\tau \leq 10^{-4}$ . Compare to Figure 11, where the fixed point iteration stops to converge at a singularity of the curve. See Example 3 of Section 4 for further details.

From the decomposition (2.7) we infer that

$$(P \circ \hat{X}_\alpha) \frac{\partial^2 \hat{X}_\alpha}{\partial \theta^i \partial \theta^j} = \Gamma(\hat{g}_\alpha)_{ij}^k \frac{\partial \hat{X}_\alpha}{\partial \theta^k}, \quad (5.4)$$

and hence,

$$(P \circ \hat{X}_\alpha) \hat{g}_\alpha^{ij} \frac{\partial^2 \hat{X}_\alpha}{\partial \theta^i \partial \theta^j} = \hat{g}_\alpha^{ij} \Gamma(\hat{g}_\alpha)_{ij}^m \delta_m^k \frac{\partial \hat{X}_\alpha}{\partial \theta^k} = \hat{g}_\alpha^{ij} \Gamma(\hat{g}_\alpha)_{ij}^m h^{kl} \frac{\partial \mathcal{C}_1^{-1}}{\partial \theta^l} \cdot \frac{\partial \mathcal{C}_1^{-1}}{\partial \theta^m} \frac{\partial \hat{X}_\alpha}{\partial \theta^k}.$$

Altogether, it follows that

$$\begin{aligned} (P \circ \hat{X}_\alpha) (\text{tr}_{\hat{g}_\alpha} (\nabla^h \nabla \hat{x}_\alpha)) \circ \mathcal{C}_1^{-1} &= (P \circ \hat{X}_\alpha) \hat{g}_\alpha^{ij} \left( \frac{\partial^2 \hat{X}_\alpha}{\partial \theta^i \partial \theta^j} - \Gamma(h)_{ij}^k \frac{\partial \hat{X}_\alpha}{\partial \theta^k} \right) \\ &= \hat{g}_\alpha^{ij} \frac{\partial \hat{X}_\alpha}{\partial \theta^k} h^{kl} \frac{\partial \mathcal{C}_1^{-1}}{\partial \theta^l} \cdot \left( \Gamma(\hat{g}_\alpha)_{ij}^m \frac{\partial \mathcal{C}_1^{-1}}{\partial \theta^m} - \frac{\partial^2 \mathcal{C}_1^{-1}}{\partial \theta^i \partial \theta^j} \right) \\ &= -\frac{\partial \hat{X}_\alpha}{\partial \theta^k} h^{kl} \frac{\partial \mathcal{C}_1^{-1}}{\partial \theta^l} \cdot (\Delta_{\hat{g}_\alpha} id) \circ \mathcal{C}_1^{-1}. \end{aligned}$$

The tangential gradient of a function  $f$  on  $\mathcal{M}$  satisfies the formula

$$(\nabla_{\mathcal{M}} f) \circ \mathcal{C}_1^{-1} := h^{ij} \frac{\partial F}{\partial \theta^i} \frac{\partial \mathcal{C}_1^{-1}}{\partial \theta^j}, \quad (5.5)$$

where  $F$  denotes  $F := f \circ \mathcal{C}_1^{-1}$ , see [14] for more details. Please note that a similar identity also holds for the tangential gradient on  $\Gamma(t)$  and the Riemannian metric  $\hat{g}_\alpha(t)$ . We can now deduce that

$$((P \circ \hat{x}_\alpha) \text{tr}_{\hat{g}_\alpha} (\nabla^h \nabla \hat{x}_\alpha)) \circ \mathcal{C}_1^{-1} = -(\nabla_{\mathcal{M}} \hat{x}_\alpha) \circ \mathcal{C}_1^{-1} (\Delta_{\hat{g}_\alpha} id) \circ \mathcal{C}_1^{-1},$$

and thus,

$$(\alpha \mathbf{1} + (1 - \alpha)(\nu \circ \hat{x}_\alpha) \otimes (\nu \circ \hat{x}_\alpha)) \frac{\partial}{\partial t} \hat{x}_\alpha = \Delta_{\hat{g}_\alpha} \hat{x}_\alpha - (\nabla_{\mathcal{M}} \hat{x}_\alpha) (\Delta_{\hat{g}_\alpha} id).$$

We introduce the vector field  $v_\alpha := \Delta_{\hat{g}_\alpha} id$  on  $\mathcal{M}$  and get

$$(\alpha \mathbf{1} + (1 - \alpha)(\nu \circ \hat{x}_\alpha) \otimes (\nu \circ \hat{x}_\alpha)) \frac{\partial}{\partial t} \hat{x}_\alpha = \Delta_{\hat{g}_\alpha} \hat{x}_\alpha - (\nabla_{\mathcal{M}} \hat{x}_\alpha) v_\alpha. \quad (5.6)$$

Henceforward, we write  $\hat{x}_{\alpha t}$  instead of  $\frac{\partial}{\partial t} \hat{x}_\alpha$ . We now multiply (5.6) and the definition  $v_\alpha := \Delta_{\hat{g}_\alpha} id$  on  $\mathcal{M}$  by test functions  $\chi, \xi \in H^{1,2}(\mathcal{M}, \mathbb{R}^{n+1})$  and integrate with respect to the volume form  $do_{\hat{g}_\alpha}$ . Integration by parts directly yields

$$\begin{aligned} 0 &= \alpha \int_{\mathcal{M}} \hat{x}_{\alpha t} \cdot \chi do_{\hat{g}_\alpha} + (1 - \alpha) \int_{\mathcal{M}} (\hat{x}_{\alpha t} \cdot (\nu \circ \hat{x}_\alpha)) ((\nu \circ \hat{x}_\alpha) \cdot \chi) do_{\hat{g}_\alpha} \\ &\quad + \int_{\mathcal{M}} \hat{G}_\alpha^{-1} \nabla_{\mathcal{M}} \hat{x}_\alpha : \nabla_{\mathcal{M}} \chi do_{\hat{g}_\alpha} + \int_{\mathcal{M}} ((\nabla_{\mathcal{M}} \hat{x}_\alpha) v_\alpha) \cdot \chi do_{\hat{g}_\alpha}, \end{aligned} \quad (5.7)$$

$$0 = \int_{\mathcal{M}} v_\alpha \cdot \xi do_{\hat{g}_\alpha} + \int_{\mathcal{M}} \hat{G}_\alpha^{-1} \nabla_{\mathcal{M}} id : \nabla_{\mathcal{M}} \xi do_{\hat{g}_\alpha}, \quad (5.8)$$

where we have made use of the following identity

$$\hat{g}_\alpha^{ij} \frac{\partial F}{\partial \theta^i} \frac{\partial W}{\partial \theta^j} = (\hat{G}_\alpha^{-1} \nabla_{\mathcal{M}} f \cdot \nabla_{\mathcal{M}} w) \circ \mathcal{C}_1^{-1}. \quad (5.9)$$

Here,  $f, w : \mathcal{M} \rightarrow \mathbb{R}$  denote differentiable functions on  $\mathcal{M}$ , and  $F, W$  are given by  $F := f \circ \mathcal{C}_1^{-1}$  and  $W := w \circ \mathcal{C}_1^{-1}$ , respectively. From (5.1) and (5.5) we immediately see that

$$\begin{aligned} (\hat{G}_\alpha)_{\beta\gamma} \circ \mathcal{C}_1^{-1} &= \frac{\partial (\mathcal{C}_1^{-1})_\beta}{\partial \theta^i} h^{ij} \frac{\partial \hat{X}_\alpha}{\partial \theta^j} \cdot \frac{\partial \hat{X}_\alpha}{\partial \theta^k} h^{kl} \frac{\partial (\mathcal{C}_1^{-1})_\gamma}{\partial \theta^l} + (\mu_\beta \mu_\gamma) \circ \mathcal{C}_1^{-1} \\ &= \frac{\partial (\mathcal{C}_1^{-1})_\beta}{\partial \theta^i} h^{ij} \hat{g}_{\alpha jk} h^{kl} \frac{\partial (\mathcal{C}_1^{-1})_\gamma}{\partial \theta^l} + (\mu_\beta \mu_\gamma) \circ \mathcal{C}_1^{-1} \end{aligned} \quad (5.10)$$

and hence,

$$(\hat{G}_\alpha^{-1})^{\beta\gamma} \circ \mathcal{C}_1^{-1} = \frac{\partial(\mathcal{C}_1^{-1})^\beta}{\partial\theta^i} \hat{g}_\alpha^{ij} \frac{\partial(\mathcal{C}_1^{-1})^\gamma}{\partial\theta^j} + (\mu_\beta \mu_\gamma) \circ \mathcal{C}_1^{-1}. \quad (5.11)$$

The identity (5.9) can then be obtained as follows

$$\begin{aligned} (\hat{G}_\alpha^{-1} \nabla_{\mathcal{M}} f \cdot \nabla_{\mathcal{M}} w) \circ \mathcal{C}_1^{-1} &= (\hat{G}_\alpha^{-1})^{\beta\gamma} \circ \mathcal{C}_1^{-1} \frac{\partial(\mathcal{C}_1^{-1})_\beta}{\partial\theta^k} h^{kl} \frac{\partial F}{\partial\theta^l} \frac{\partial(\mathcal{C}_1^{-1})_\gamma}{\partial\theta^s} h^{st} \frac{\partial W}{\partial\theta^t} \\ &= \hat{g}_\alpha^{ij} \frac{\partial(\mathcal{C}_1^{-1})}{\partial\theta^i} \cdot \frac{\partial(\mathcal{C}_1^{-1})}{\partial\theta^k} h^{kl} \frac{\partial F}{\partial\theta^l} \frac{\partial(\mathcal{C}_1^{-1})}{\partial\theta^j} \cdot \frac{\partial(\mathcal{C}_1^{-1})}{\partial\theta^s} h^{st} \frac{\partial W}{\partial\theta^t} \\ &= \hat{g}_\alpha^{ij} h_{ik} h^{kl} \frac{\partial F}{\partial\theta^l} h_{js} h^{st} \frac{\partial W}{\partial\theta^t} \\ &= \hat{g}_\alpha^{ij} \frac{\partial F}{\partial\theta^i} \frac{\partial W}{\partial\theta^j}. \end{aligned}$$

Please be aware that the expressions  $\hat{G}_\alpha^{-1} \nabla_{\mathcal{M}} \hat{x}_\alpha : \nabla_{\mathcal{M}} \chi$  in (5.7) and  $\hat{G}_\alpha^{-1} \nabla_{\mathcal{M}} id : \nabla_{\mathcal{M}} \xi$  in (5.8) are meant to be the following sums

$$\begin{aligned} \hat{G}_\alpha^{-1} \nabla_{\mathcal{M}} \hat{x}_\alpha : \nabla_{\mathcal{M}} \chi &= (\hat{G}_\alpha^{-1})^{\beta\gamma} \underline{D}_\beta \hat{x}_\alpha \cdot \underline{D}_\gamma \chi, \\ \hat{G}_\alpha^{-1} \nabla_{\mathcal{M}} id : \nabla_{\mathcal{M}} \xi &= (\hat{G}_\alpha^{-1})^{\beta\gamma} \underline{D}_\beta id \cdot \underline{D}_\gamma \xi. \end{aligned}$$

It is not difficult to show that the volume form  $do_{\hat{g}_\alpha}$  satisfy the following identity

$$do_{\hat{g}_\alpha} = \sqrt{\det \hat{G}_\alpha} do_h. \quad (5.12)$$

Without loss of generality we can suppose that  $\mu = (0, \dots, 0, 1)^T$ . It then follows that

$$\mathbb{R}^{(n+1) \times n} \ni \left( \frac{\partial(\mathcal{C}_1^{-1})}{\partial\theta^i} \right)_{i=1, \dots, n} = \begin{pmatrix} S \\ 0 \end{pmatrix}$$

for some  $S \in \mathbb{R}^{n \times n}$ , and together with (5.10),

$$\det \hat{G}_\alpha \circ \mathcal{C}_1^{-1} = \det S \det(h_{ij})^{-1} \det(\hat{g}_{\alpha jk}) \det(h_{kl})^{-1} \det S = \frac{\det(\hat{g}_{\alpha jk})}{\det(h_{jk})}, \quad (5.13)$$

where we have made use of  $(\det S)^2 = \det(h_{ij})$ .  $\square$

## 5.2 Weak formulation on the moving hypersurface $\Gamma(t)$

The weak formulation in Lemma 2 could, in principle, be used for developing an algorithm for the computation of the mean curvature-DeTurck flow. However, we will not follow this route here, since numerical schemes based on surface finite elements are usually formulated on the moving hypersurface  $\Gamma(t) := \hat{x}_\alpha(\mathcal{M}, t) \subset \mathbb{R}^{n+1}$  rather than on the reference manifold. In this section we therefore reformulate the problem on the moving hypersurface  $\Gamma(t)$ .

In the following we derive a weak formulation for the map  $u : \Gamma(t) \times [0, T] \rightarrow \mathbb{R}^{n+1}$  defined by  $u := \hat{x}_\alpha \circ \hat{x}_\alpha^{-1}$ . Obviously, we have  $u = id|_{\Gamma(t)}$ . We define the material derivative of a differentiable function  $f$  on  $\Gamma(t)$  by

$$(\partial^\bullet f) \circ \hat{x}_\alpha = \frac{\partial}{\partial t} (f \circ \hat{x}_\alpha).$$

The material derivative of  $u$  is thus given by

$$\partial^\bullet u = \frac{\partial \hat{x}_\alpha}{\partial t} \circ \hat{x}_\alpha^{-1}. \quad (5.14)$$

We want to recall that in this section the reference manifold  $\mathcal{M}$  is assumed to be an  $n$ -dimensional hypersurface in  $\mathbb{R}^{n+1}$ . Similar to the definition of the map  $\hat{G}_\alpha(t)$  in (5.1), we next introduce the global representation  $\hat{H}_\alpha : \bigcup_{t \in [0, T]} \Gamma(t) \times \{t\} \rightarrow \mathbb{R}^{(n+1) \times (n+1)}$  of the Riemannian metric  $\hat{h}_\alpha(t) := (\hat{x}_\alpha^{-1}(t))^* \mathfrak{e}$  on  $\Gamma(t)$ . The map  $\hat{H}_\alpha(t)$  is defined by

$$\hat{H}_\alpha(t) := (\nabla_{\Gamma(t)} \hat{x}_\alpha^{-1}(t))^T \nabla_{\Gamma(t)} \hat{x}_\alpha^{-1}(t) + \nu(t) \otimes \nu(t). \quad (5.15)$$

Here,  $\nu(t)$  is a unit normal field to  $\Gamma(t)$ . That  $\hat{H}_\alpha(t)$  is indeed a global representation of the metric  $\hat{h}_\alpha(t)$  is shown in (5.19). Using the material derivative, the weak formulation in Lemma 2 can be lifted onto the moving hypersurface  $\Gamma(t)$ . This is summarized in the following statement.

**Theorem 3.** Under the same assumptions as in Lemma 2, the identity map  $u = id_{\Gamma(t)}$  on  $\Gamma(t)$  satisfies

$$\begin{aligned} 0 &= \alpha \int_{\Gamma(t)} \partial^\bullet u \cdot \eta d\sigma + (1 - \alpha) \int_{\Gamma(t)} (\partial^\bullet u \cdot \nu)(\nu \cdot \eta) d\sigma \\ &\quad + \int_{\Gamma(t)} \nabla_{\Gamma(t)} u : \nabla_{\Gamma(t)} \eta d\sigma + \int_{\Gamma(t)} w_\alpha \cdot (\nabla_{\Gamma(t)} \hat{x}_\alpha^{-1} \hat{H}_\alpha^{-1} \eta) d\sigma, \\ 0 &= \int_{\Gamma(t)} w_\alpha \cdot \zeta d\sigma + \int_{\Gamma(t)} \nabla_{\Gamma(t)} \hat{x}_\alpha^{-1} : \nabla_{\Gamma(t)} \zeta d\sigma, \end{aligned}$$

for all  $\eta, \zeta \in H^{1,2}(\Gamma(t), \mathbb{R}^{n+1})$  and  $t \in [0, T]$ .

*Proof.* In order to be able to distinguish between the components of the tangential gradients on  $\mathcal{M}$  and on  $\Gamma(t)$ , we introduce the following notation

$$\begin{pmatrix} \underline{D}_1 f \\ \vdots \\ \underline{D}_{n+1} f \end{pmatrix} := \nabla_{\mathcal{M}} f, \quad \text{and} \quad \begin{pmatrix} \underline{D}'_1 f \\ \vdots \\ \underline{D}'_{n+1} f \end{pmatrix} := \nabla_{\Gamma(t)} f,$$

where  $f$  is a differentiable function on  $\mathcal{M}$ , or on  $\Gamma(t)$ , respectively. For differentiable functions  $f, w : \Gamma(t) \times [0, T] \rightarrow \mathbb{R}^{n+1}$ , we obtain the identity

$$\underline{D}_\beta(f \circ \hat{x}_\alpha) = (\underline{D}'_\kappa f) \circ \hat{x}_\alpha \underline{D}_\beta(\hat{x}_\alpha)^\kappa, \quad (5.16)$$

and hence,

$$\begin{aligned} (\hat{G}_\alpha^{-1})^{\beta\gamma} \underline{D}_\beta(f \circ \hat{x}_\alpha) \underline{D}_\gamma(w \circ \hat{x}_\alpha) &= (\hat{G}_\alpha^{-1})^{\beta\gamma} (\underline{D}'_\kappa f) \circ \hat{x}_\alpha \underline{D}_\beta(\hat{x}_\alpha)^\kappa (\underline{D}'_\iota w) \circ \hat{x}_\alpha \underline{D}_\gamma(\hat{x}_\alpha)^\iota \\ &= (\hat{G}_\alpha^{-1})^{\beta\gamma} \underline{D}_\beta(\hat{x}_\alpha)^\kappa \underline{D}_\gamma(\hat{x}_\alpha)^\iota (\underline{D}'_\kappa f \underline{D}'_\iota w) \circ \hat{x}_\alpha \\ &= P^{\kappa\iota} \circ \hat{x}_\alpha (\underline{D}'_\kappa f \underline{D}'_\iota w) \circ \hat{x}_\alpha = (\underline{D}'_\kappa f \underline{D}'_\iota w) \circ \hat{x}_\alpha, \end{aligned}$$

where we have made use of the identity  $(\hat{G}_\alpha^{-1})^{\beta\gamma} \underline{D}_\beta(\hat{x}_\alpha)^\kappa \underline{D}_\gamma(\hat{x}_\alpha)^\iota = P^{\kappa\iota} \circ \hat{x}_\alpha$ . Applying this result, it is easy to see that

$$\hat{G}_\alpha^{-1} \nabla_{\mathcal{M}} \hat{x}_\alpha : \nabla_{\mathcal{M}} \chi = (\nabla_{\Gamma(t)} u : \nabla_{\Gamma(t)} (\chi \circ \hat{x}_\alpha^{-1})) \circ \hat{x}_\alpha, \quad (5.17)$$

$$\hat{G}_\alpha^{-1} \nabla_{\mathcal{M}} id : \nabla_{\mathcal{M}} \xi = (\nabla_{\Gamma(t)} \hat{x}_\alpha^{-1} : \nabla_{\Gamma(t)} (\xi \circ \hat{x}_\alpha^{-1})) \circ \hat{x}_\alpha. \quad (5.18)$$

As in (5.10) and (5.11), we obtain the following relations between the components of the map  $\hat{H}_\alpha(t)$  and the components  $\hat{h}_{\alpha ij}(t)$  of the Riemannian metric  $\hat{h}_\alpha(t) := (\hat{x}_\alpha^{-1}(t))^* \mathfrak{e}$  on  $\Gamma(t)$

$$(\hat{H}_\alpha)_{\beta\gamma} \circ \hat{X}_\alpha = \frac{\partial(\hat{X}_\alpha)_\beta}{\partial\theta^i} \hat{g}_\alpha^{ij} \hat{h}_{\alpha jk} \hat{g}_\alpha^{kl} \frac{\partial(\hat{X}_\alpha)_\gamma}{\partial\theta^l} + (\nu_\beta \nu_\gamma) \circ \hat{X}_\alpha, \quad (5.19)$$

$$(\hat{H}_\alpha^{-1})^{\beta\gamma} \circ \hat{X}_\alpha = \frac{\partial(\hat{X}_\alpha)^\beta}{\partial\theta^i} \hat{h}_\alpha^{ij} \frac{\partial(\hat{X}_\alpha)^\gamma}{\partial\theta^j} + (\nu_\beta \nu_\gamma) \circ \hat{X}_\alpha, \quad (5.20)$$

where

$$\begin{aligned} \hat{h}_{\alpha ij} &= \frac{\partial(\hat{x}_\alpha^{-1} \circ \hat{X}_\alpha)}{\partial\theta^i} \cdot \frac{\partial(\hat{x}_\alpha^{-1} \circ \hat{X}_\alpha)}{\partial\theta^j}, \quad \text{and} \quad (\hat{h}_\alpha^{ij})_{i,j=1,\dots,n} := (\hat{h}_{\alpha ij})_{i,j=1,\dots,n}^{-1}, \\ \hat{g}_{\alpha ij} &= \frac{\partial\hat{X}_\alpha}{\partial\theta^i} \cdot \frac{\partial\hat{X}_\alpha}{\partial\theta^j}, \quad \text{and} \quad (\hat{g}_\alpha^{ij})_{i,j=1,\dots,n} := (\hat{g}_{\alpha ij})_{i,j=1,\dots,n}^{-1}. \end{aligned}$$

Please note that  $\hat{h}_\alpha(t)$  is a metric on  $\Gamma(t)$ , whereas  $h(t)$  is a metric on  $\mathcal{M}$ . However, since  $\hat{X}_\alpha := \hat{x}_\alpha \circ \mathcal{C}_1^{-1}$ , we have

$$\hat{h}_{\alpha ij} = \frac{\partial\mathcal{C}_1^{-1}}{\partial\theta^i} \cdot \frac{\partial\mathcal{C}_1^{-1}}{\partial\theta^j} = h_{ij}.$$

It follows that

$$(\hat{H}_\alpha)_{\beta\gamma} \circ \hat{X}_\alpha = \frac{\partial(\hat{X}_\alpha)_\beta}{\partial\theta^i} \hat{g}_\alpha^{ij} h_{jk} \hat{g}_\alpha^{kl} \frac{\partial(\hat{X}_\alpha)_\gamma}{\partial\theta^l} + (\nu_\beta \nu_\gamma) \circ \hat{X}_\alpha, \quad (5.21)$$

$$(\hat{H}_\alpha^{-1})^{\beta\gamma} \circ \hat{X}_\alpha = \frac{\partial(\hat{X}_\alpha)^\beta}{\partial\theta^i} h^{ij} \frac{\partial(\hat{X}_\alpha)^\gamma}{\partial\theta^j} + (\nu_\beta \nu_\gamma) \circ \hat{X}_\alpha. \quad (5.22)$$

Using the latter identity and (5.5), we deduce that

$$\begin{aligned}
(\nabla_{\mathcal{M}}(\hat{x}_\alpha)^\beta) \circ \mathcal{C}_1^{-1} &= \frac{\partial(\hat{X}_\alpha)^\beta}{\partial\theta^i} h^{ij} \frac{\partial\mathcal{C}_1^{-1}}{\partial\theta^j} = \frac{\partial(\hat{X}_\alpha)^\beta}{\partial\theta^i} h^{ij} \frac{\partial(\hat{x}_\alpha^{-1} \circ \hat{X}_\alpha)}{\partial\theta^j} \\
&= \frac{\partial(\hat{X}_\alpha)^\beta}{\partial\theta^i} h^{ij} \hat{g}_{\alpha j l} \hat{g}_\alpha^{lk} \frac{\partial(\hat{x}_\alpha^{-1} \circ \hat{X}_\alpha)}{\partial\theta^k} \\
&= \frac{\partial(\hat{X}_\alpha)^\beta}{\partial\theta^i} h^{ij} \frac{\partial\hat{X}_\alpha}{\partial\theta^j} \cdot \frac{\partial\hat{X}_\alpha}{\partial\theta^l} \hat{g}_\alpha^{lk} \frac{\partial(\hat{x}_\alpha^{-1} \circ \hat{X}_\alpha)}{\partial\theta^k} \\
&= \frac{\partial(\hat{X}_\alpha)^\beta}{\partial\theta^i} h^{ij} \frac{\partial(\hat{X}_\alpha)^\gamma}{\partial\theta^j} (\underline{D}'_\gamma \hat{x}_\alpha^{-1}) \circ \hat{X}_\alpha \\
&= (\hat{H}_\alpha^{-1})^{\beta\gamma} \circ \hat{X}_\alpha (\underline{D}'_\gamma \hat{x}_\alpha^{-1}) \circ \hat{X}_\alpha,
\end{aligned}$$

and hence,

$$\nabla_{\mathcal{M}}(\hat{x}_\alpha)^\beta = \left( (\hat{H}_\alpha^{-1})^{\beta\gamma} \underline{D}'_\gamma \hat{x}_\alpha^{-1} \right) \circ \hat{x}_\alpha. \quad (5.23)$$

The integral on  $\mathcal{M}$  with respect to the volume form  $do_{\hat{g}_\alpha}$  is transformed into an integral on  $\Gamma(t)$  with respect to the volume form  $d\sigma$  induced by the Hausdorff measure in the following way

$$\begin{aligned}
\int_{\mathcal{M}} f do_{\hat{g}_\alpha} &= \int_{\Omega} f \circ \mathcal{C}_1^{-1} \sqrt{\det(\hat{g}_{\alpha ij})} d^n \theta \\
&= \int_{\Omega} (f \circ \hat{x}_\alpha^{-1}) \circ \hat{X}_\alpha \sqrt{\det \left( \frac{\partial\hat{X}_\alpha}{\partial\theta^i} \cdot \frac{\partial\hat{X}_\alpha}{\partial\theta^j} \right)} d^n \theta \\
&= \int_{\Gamma(t)} f \circ \hat{x}_\alpha^{-1} d\sigma,
\end{aligned}$$

where  $f : \mathcal{M} \rightarrow \mathbb{R}$  denotes an integrable function with  $\text{supp} f \subset U$  and  $\mathcal{C}_1 : U \subset \mathcal{M} \rightarrow \Omega \subset \mathbb{R}^n$  is a local coordinate chart of  $\mathcal{M}$ . This result can be easily generalized using a partition of unity. From (5.7) and (5.8) we then infer that

$$\begin{aligned}
0 &= \alpha \int_{\Gamma(t)} (\hat{x}_{\alpha t} \cdot \chi) \circ \hat{x}_\alpha^{-1} d\sigma + (1 - \alpha) \int_{\Gamma(t)} ((\hat{x}_{\alpha t} \cdot (\nu \circ \hat{x}_\alpha))((\nu \circ \hat{x}_\alpha) \cdot \chi)) \circ \hat{x}_\alpha^{-1} d\sigma \\
&\quad + \int_{\Gamma(t)} \left( \hat{G}_\alpha^{-1} \nabla_{\mathcal{M}} \hat{x}_\alpha : \nabla_{\mathcal{M}} \chi \right) \circ \hat{x}_\alpha^{-1} d\sigma + \int_{\Gamma(t)} \left( ((\nabla_{\mathcal{M}} \hat{x}_\alpha) v_\alpha) \cdot \chi \right) \circ \hat{x}_\alpha^{-1} d\sigma, \\
0 &= \int_{\Gamma(t)} (v_\alpha \cdot \xi) \circ \hat{x}_\alpha^{-1} d\sigma + \int_{\Gamma(t)} \left( \hat{G}_\alpha^{-1} \nabla_{\mathcal{M}} id : \nabla_{\mathcal{M}} \xi \right) \circ \hat{x}_\alpha^{-1} d\sigma.
\end{aligned}$$

Using the notations  $w_\alpha := v_\alpha \circ \hat{x}_\alpha^{-1}$ ,  $\eta := \chi \circ \hat{x}_\alpha^{-1}$  and  $\zeta := \xi \circ \hat{x}_\alpha^{-1}$ , and applying the identities (5.14), (5.17), (5.18) and (5.23) finally proves the claim.  $\square$

### 5.3 Numerical scheme on moving hypersurfaces

We will now discretize the weak formulation which we received in Theorem 3 in space and time. The reference hypersurface  $\mathcal{M} \subset \mathbb{R}^{n+1}$  is supposed to be approximated by a piecewise linear, polyhedral hypersurface

$$\mathcal{M}_h := \bigcup_{T \in \mathcal{T}_h} T \subset \mathbb{R}^{n+1}.$$

Here,  $\mathcal{T}_h$  is an admissible triangulation consisting of non-degenerate  $n$ -dimensional simplices in  $\mathbb{R}^{n+1}$ . The finite element space  $\mathcal{S}(\mathcal{M}_h)$  is the set of piecewise linear, continuous functions

$$\mathcal{S}(\mathcal{M}_h) := \{ \chi_h \in C^0(\mathcal{M}_h) \mid \chi_h|_T \text{ is a linear polynomial for all } T \in \mathcal{T}_h \}. \quad (5.24)$$

$\mathcal{S}(\mathcal{M}_h)$  is a linear space of dimension  $N$ , where  $N$  is the number of the vertices  $p_j \in \mathcal{M}_h$ ,  $j = 1, \dots, N$ , of the triangulation. It is spanned by the basis functions  $\phi_i \in \mathcal{S}(\mathcal{M}_h)$  defined by  $\phi_i(p_j) = \delta_{ij}$ ,  $\forall i, j = 1, \dots, N$ .

For the time discretization we introduce the notation  $f^m = f(\cdot, m\tau)$  for the discrete time levels  $\{m\tau \mid m = 0, \dots, M_\tau \in \mathbb{N}\}$  with time step size  $\tau > 0$  and  $M_\tau \tau < T$ . The approximation of the moving hypersurface  $\Gamma(t)$  at time  $m\tau$  will be denoted by

$$\Gamma_h^m := \bigcup_{T \in \mathcal{T}_h^m} T \subset \mathbb{R}^{n+1},$$



where  $\mathcal{T}_h^m$  is an admissible triangulation of  $n$ -simplices in  $\mathbb{R}^{n+1}$ . The finite element spaces  $\mathcal{S}(\Gamma_h^m)$  are defined in accordance to (5.24). The tangential gradient  $\nabla_{\Gamma_h^m}$  on  $\Gamma_h^m$  is defined piecewise on each  $n$ -simplex  $T \in \mathcal{T}_h^m$ . Taking the geometric quantities from the previous time step, it is possible to linearize the problem in each time step and to obtain a semi-implicit scheme in the spirit of [13]. In order to make the scheme more implicit, we observe that  $\nabla_{\Gamma} u = P$  and write

$$\begin{aligned} w_\alpha \cdot (\nabla_{\Gamma(t)} \hat{x}_\alpha^{-1} \hat{H}_\alpha^{-1} \eta) &= w_\alpha \cdot (\nabla_{\Gamma(t)} \hat{x}_\alpha^{-1} \hat{H}_\alpha^{-1} P \eta) \\ &= P \hat{H}_\alpha^{-1} (\nabla_{\Gamma(t)} \hat{x}_\alpha^{-1})^T w_\alpha \cdot \eta \\ &= (\nabla_{\Gamma} u) \hat{H}_\alpha^{-1} (\nabla_{\Gamma(t)} \hat{x}_\alpha^{-1})^T w_\alpha \cdot \eta. \end{aligned}$$

This leads to the following scheme.

**Algorithm 2.** Let  $\alpha \in (0, \infty)$ . For a given initial polyhedral hypersurface  $\Gamma_h^0 = \hat{x}_h^0(\mathcal{M}_h)$  with  $\hat{x}_h^0 \in \mathcal{S}(\mathcal{M}_h)^{n+1}$ , set  $y_h^0 := (\hat{x}_h^0)^{-1} \in \mathcal{S}(\Gamma_h^0)^{n+1}$  and determine for  $m = 0, \dots, M_\tau - 1$  solutions  $u_h^{m+1} \in \mathcal{S}(\Gamma_h^m)^{n+1}$  and  $w_h^m \in \mathcal{S}(\Gamma_h^m)^{n+1}$  such that

$$\begin{aligned} &\frac{\alpha}{\tau} \int_{\Gamma_h^m} u_h^{m+1} \cdot \eta_h d\sigma + \frac{1-\alpha}{\tau} \int_{\Gamma_h^m} (u_h^{m+1} \cdot \nu_h^m)(\nu_h^m \cdot \eta_h) d\sigma + \int_{\Gamma_h^m} \nabla_{\Gamma_h^m} u_h^{m+1} : \nabla_{\Gamma_h^m} \eta_h d\sigma \\ &\quad + \int_{\Gamma_h^m} \nabla_{\Gamma_h^m} u_h^{m+1} (\hat{H}_h^m)^{-1} (\nabla_{\Gamma_h^m} y_h^m)^T w_h^m \cdot \eta_h d\sigma = \int_{\Gamma_h^m} \frac{\alpha}{\tau} (\tilde{u}_h^m \cdot \eta_h) + \frac{1-\alpha}{\tau} (\tilde{u}_h^m \cdot \nu_h^m)(\nu_h^m \cdot \eta_h) d\sigma, \\ &\int_{\Gamma_h^m} w_h^m \cdot \zeta_h d\sigma + \int_{\Gamma_h^m} \nabla_{\Gamma_h^m} y_h^m : \nabla_{\Gamma_h^m} \zeta_h d\sigma = 0, \end{aligned}$$

for all  $\eta_h, \zeta_h \in \mathcal{S}(\Gamma_h^m)^{n+1}$ , where  $\nu_h^m$  is a unit normal to  $\Gamma_h^m$ , and

$$\begin{aligned} \tilde{u}_h^m &:= id|_{\Gamma_h^m}, \\ \hat{H}_h^m &:= (\nabla_{\Gamma_h^m} y_h^m)^T \nabla_{\Gamma_h^m} y_h^m + \nu_h^m \otimes \nu_h^m. \end{aligned}$$

The hypersurface  $\Gamma_h^{m+1}$  is defined by

$$\Gamma_h^{m+1} := u_h^{m+1}(\Gamma_h^m),$$

and  $y_h^{m+1} \in \mathcal{S}(\Gamma_h^{m+1})^{n+1}$  is set to be

$$y_h^{m+1} := y_h^m \circ (u_h^{m+1})^{-1}.$$

**Remark 6.** Please note that we do not have to keep track of two different triangulations in the above algorithm. The reference mesh  $\mathcal{M}_h$  only enters into the scheme via the maps  $y_h^m$ . As soon as the map  $y_h^0$  is initialized, the reference mesh  $\mathcal{M}_h$  is not needed any more. Moreover, as we will describe in Section 7, the representation vector  $\mathbf{Y}$  of the maps  $y_h^m$  does not depend on the discrete time levels  $m$ . So in the computer code, the only remnant of the reference manifold is a constant vector.

**Remark 7.** In numerical experiments we observe that the above algorithm is able to redistribute the mesh points of the evolving surface  $\Gamma_h^m$  in such a way that, at least for small  $\alpha$ , the discrete surfaces  $\Gamma_h^m$  and  $\mathcal{M}_h$  are of similar mesh quality. It is therefore crucial to have a reference mesh  $\mathcal{M}_h$  of sufficiently high quality.

**Remark 8.** Please note that the term  $\nabla_{\Gamma_h^m} u_h^{m+1} (\hat{H}_h^m)^{-1} (\nabla_{\Gamma_h^m} y_h^m)^T w_h^m$  in the above algorithm is the product of the first order term  $\nabla_{\Gamma_h^m} u_h^{m+1}$  and the second order term  $w_h^m$ , which is the weak Laplacian of  $y_h^m$ . Since first order terms are, roughly speaking, more critical in numerical simulations with respect to stability, an alternative approach that only leads to a (pure) second order term might be desirable in certain cases. As we will see below, a slight variation of the original DeTurck trick indeed gives rise to a scheme where the elliptic operator only consists of second order terms. By this means, we will obtain an algorithm for the computation of a variant of the mean curvature-DeTurck flow.

## 6 Reparametrizations via a variant of the DeTurck trick

In the following we introduce a variant of the DeTurck trick. We start by changing the system of equations  $(P)$  in Section 2 in the following way

$$(P') = \begin{cases} \frac{\partial}{\partial t} x = -(H\nu) \circ x, & \text{with } x(\cdot, 0) = x_0 \text{ on } \mathcal{M}, \\ \frac{\partial}{\partial t} \psi_\alpha = \frac{1}{\alpha} \Delta_{h,g(t)} \psi_\alpha, & \text{with } g(t) := x(t)^* \mathfrak{e} \text{ and } \psi_\alpha(\cdot, 0) = id(\cdot) \text{ on } \mathcal{M}, \end{cases}$$

where  $h$  is again a fixed yet arbitrary smooth Riemannian metric on  $\mathcal{M}$ . The difference between problem  $(P)$  in Section 2 and  $(P')$  is that the metrics  $h$  and  $g(t) := x(t)^* \mathfrak{e}$  in the map Laplacian have been permuted. By this means we will obtain a reparametrized flow that is (almost) in divergence form if we define the reparametrization of the mean curvature flow by

$$\hat{x}_\alpha(t) := (\psi_\alpha(t)^{-1})_* x(t) := (\psi_\alpha(t))^* x(t) := x(t) \circ \psi_\alpha(t). \quad (6.1)$$

In contrast to definition (2.9) the reparametrization is here defined by using the push-forward instead of the pull-back. Similar as in (2.12), we first observe that the the push-forward metric  $(\psi_\alpha^{-1}(t))_* g(t)$  and the induced metric  $(\hat{x}_\alpha(t))^* \mathfrak{e}$  are equal

$$(\psi_\alpha^{-1}(t))_* g(t) = \psi_\alpha(t)^* g(t) = \psi_\alpha(t)^* (x(t)^* \mathfrak{e}) = (x(t) \circ \psi_\alpha(t))^* \mathfrak{e} = (\hat{x}_\alpha(t))^* \mathfrak{e} =: \hat{g}_\alpha(t). \quad (6.2)$$

The same procedure as in Section 2 then leads to the following evolution equation of the reparametrized flow

$$\begin{aligned} \frac{\partial}{\partial t} \hat{x}_\alpha(t) &= \frac{\partial}{\partial t} x(t) \circ \psi_\alpha(t) + (\nabla x \circ \psi_\alpha(t)) \left( \frac{\partial}{\partial t} \psi_\alpha(t) \right) \\ &= (\Delta_{g(t)} x) \circ \psi_\alpha(t) + \frac{1}{\alpha} (\nabla x \circ \psi_\alpha(t)) (\Delta_{h,g(t)} \psi_\alpha(t)) \\ &= -(H\nu) \circ \hat{x}_\alpha(t) + \frac{1}{\alpha} (\nabla x \circ \psi_\alpha(t)) (\Delta_{h,g(t)} \psi_\alpha(t)) \\ &= \Delta_{\hat{g}_\alpha(t)} \hat{x}_\alpha + \frac{1}{\alpha} (\nabla x \circ \psi_\alpha(t)) (\Delta_{h,g(t)} \psi_\alpha(t)). \end{aligned}$$

In the following we will show that the second term on the right hand side is given by

$$(\nabla x \circ \psi_\alpha(t)) (\Delta_{h,g(t)} \psi_\alpha(t)) = (P \circ \hat{x}_\alpha) \Delta_h \hat{x}_\alpha, \quad (6.3)$$

and hence,

$$\frac{\partial}{\partial t} \hat{x}_\alpha(t) = \Delta_{\hat{g}_\alpha(t)} \hat{x}_\alpha + \frac{1}{\alpha} (P \circ \hat{x}_\alpha) \Delta_h \hat{x}_\alpha.$$

We are not aware that the above equation has yet been considered elsewhere. For  $\Psi_\alpha = \mathcal{C}_2 \circ \psi_\alpha \circ \mathcal{C}_1^{-1}$ ,  $X := x \circ \mathcal{C}_2^{-1}$  and  $\hat{X}_\alpha := \hat{x}_\alpha \circ \mathcal{C}_1^{-1}$  we obtain that

$$\frac{\partial \hat{X}_\alpha}{\partial \theta^k} \left( \frac{\partial (\Psi_\alpha^{-1})^k}{\partial \theta^l} \circ \Psi_\alpha \right) = \frac{\partial X}{\partial \theta^j} \circ \Psi_\alpha \frac{\partial \Psi_\alpha^j}{\partial \theta^k} \left( \frac{\partial (\Psi_\alpha^{-1})^k}{\partial \theta^l} \circ \Psi_\alpha \right) = \frac{\partial X}{\partial \theta^l} \circ \Psi_\alpha.$$

Therefore, in local coordinates  $\mathcal{C}_1$  the term  $\nabla x \circ \psi_\alpha(t) (\Delta_{h,g(t)} \psi_\alpha(t))$  is given by

$$\begin{aligned} &\frac{\partial \hat{X}_\alpha}{\partial \theta^k} \left( \frac{\partial (\Psi_\alpha^{-1})^k}{\partial \theta^l} \circ \Psi_\alpha \right) h^{mn} \left( \frac{\partial^2 \Psi_\alpha^l}{\partial \theta^m \partial \theta^n} - \Gamma(h)_{mn}^p \frac{\partial \Psi_\alpha^l}{\partial \theta^p} + \Gamma(g)_{ij}^l \circ \Psi_\alpha \frac{\Psi_\alpha^i}{\partial \theta^m} \frac{\Psi_\alpha^j}{\partial \theta^n} \right) \\ &= -\frac{\partial \hat{X}_\alpha}{\partial \theta^k} h^{mn} \Gamma(h)_{mn}^k + \frac{\partial \hat{X}_\alpha}{\partial \theta^k} h^{mn} \left( \frac{\partial (\Psi_\alpha^{-1})^k}{\partial \theta^l} \circ \Psi_\alpha \right) \left( \frac{\partial^2 \Psi_\alpha^l}{\partial \theta^m \partial \theta^n} + \Gamma(g)_{ij}^l \circ \Psi_\alpha \frac{\Psi_\alpha^i}{\partial \theta^m} \frac{\Psi_\alpha^j}{\partial \theta^n} \right), \end{aligned}$$

where in this case the indices  $k, m, n, p$  refer to the coordinate chart  $\mathcal{C}_1$  and the indices  $i, j, l$  to the coordinate chart  $\mathcal{C}_2$ . From (6.2) it follows that

$$\begin{aligned} \hat{g}_{\alpha mn} &= (g_{ij} \circ \Psi_\alpha) \frac{\partial \Psi_\alpha^i}{\partial \theta^m} \frac{\partial \Psi_\alpha^j}{\partial \theta^n}, \quad \text{and} \quad g^{ij} \circ \Psi_\alpha = (\hat{g}_\alpha^{mn}) \frac{\partial \Psi_\alpha^i}{\partial \theta^m} \frac{\partial \Psi_\alpha^j}{\partial \theta^n}, \\ \text{as well as} \quad \frac{\partial (\Psi_\alpha)^l}{\partial \theta^k} \Gamma(\hat{g})_{mn}^k &= \left( \frac{\partial^2 \Psi_\alpha^l}{\partial \theta^m \partial \theta^n} + \Gamma(g)_{ij}^l \circ \Psi_\alpha \frac{\partial \Psi_\alpha^i}{\partial \theta^m} \frac{\partial \Psi_\alpha^j}{\partial \theta^n} \right), \end{aligned}$$

and hence,

$$(\nabla x \circ \psi_\alpha(t) (\Delta_{h,g(t)} \psi_\alpha(t))) \circ \mathcal{C}_1^{-1} = -\frac{\partial \hat{X}_\alpha}{\partial \theta^k} h^{mn} \Gamma(h)_{mn}^k + \frac{\partial \hat{X}_\alpha}{\partial \theta^k} h^{mn} \Gamma(\hat{g})_{mn}^k.$$

Since identity (5.4) is still true, we finally obtain

$$\begin{aligned} (\nabla x \circ \psi_\alpha(t) (\Delta_{h,g(t)} \psi_\alpha(t))) \circ \mathcal{C}_1^{-1} &= -\frac{\partial \hat{X}_\alpha}{\partial \theta^k} h^{mn} \Gamma(h)_{mn}^k + h^{mn} (P \circ \hat{X}_\alpha) \frac{\partial^2 \hat{X}_\alpha}{\partial \theta^m \partial \theta^n} \\ &= (P \circ \hat{X}_\alpha) h^{mn} \left( \frac{\partial^2 \hat{X}_\alpha}{\partial \theta^m \partial \theta^n} - \Gamma(h)_{mn}^k \frac{\partial \hat{X}_\alpha}{\partial \theta^k} \right), \end{aligned}$$

which proves (6.3). Instead of (2.19) we now apply the map

$$((\nu \circ \hat{x}_\alpha) \otimes (\nu \circ \hat{x}_\alpha) + \alpha \hat{\rho} P \circ \hat{x}_\alpha) = (\alpha \hat{\rho} \mathbf{1} + (1 - \alpha \hat{\rho})(\nu \circ \hat{x}_\alpha) \otimes (\nu \circ \hat{x}_\alpha)),$$

where  $\hat{\rho} := \sqrt{\det(h_{ij})}/\sqrt{\det(\hat{g}_{\alpha ij})}$ . Please note that the definition of  $\hat{\rho}$  does not depend on the local coordinates in which it is evaluated. This yields

**Theorem 4.** *The reparametrized mean curvature flow  $\hat{x}_\alpha : \mathcal{M} \times [0, T) \rightarrow \mathbb{R}^{n+1}$  defined in (6.1) satisfies*

$$(\alpha \hat{\rho} \mathbf{1} + (1 - \alpha \hat{\rho})(\nu \circ \hat{x}_\alpha) \otimes (\nu \circ \hat{x}_\alpha)) \frac{\partial}{\partial t} \hat{x}_\alpha = \Delta_{\hat{g}_\alpha(t)} \hat{x}_\alpha + \hat{\rho} (P \circ \hat{x}_\alpha) \Delta_h \hat{x}_\alpha, \quad (6.4)$$

with  $\hat{x}_\alpha(\cdot, 0) = x_0(\cdot)$  on  $\mathcal{M}$ .

Using the above identities, a short calculation shows that the inverse  $\psi_\alpha^{-1}$  solves an ODE, which in local coordinates is given by

$$\frac{\partial}{\partial t} (\Psi_\alpha^{-1})^k = \frac{1}{\alpha} (h^{mn} (\Gamma(h)_{mn}^k - \Gamma(\hat{g}_\alpha)_{mn}^k)) \circ \Psi_\alpha^{-1}.$$

Solving this equation and setting  $x(t) = \hat{x}_\alpha(t) \circ \psi_\alpha(t)^{-1}$ , one can recover the solution to (2.5) from the solution to (6.4).

## 6.1 Weak formulation

We now assume again that  $\mathcal{M}$  is a hypersurface in  $\mathbb{R}^{n+1}$  and we choose the metric  $h$  on the reference hypersurface  $\mathcal{M} \subset \mathbb{R}^{n+1}$  to be the metric that is induced by the Euclidean metric  $\mathfrak{e}$  of the ambient space. We multiply (6.4) by a test function  $\chi \in H^{1,2}(\mathcal{M}, \mathbb{R}^{n+1})$ . Integrating with respect to the volume form  $do_{\hat{g}_\alpha}$  then gives

$$\begin{aligned} 0 &= \int_{\mathcal{M}} (\alpha \hat{\rho}) \hat{x}_{\alpha t} \cdot \chi do_{\hat{g}_\alpha} + \int_{\mathcal{M}} (1 - \alpha \hat{\rho}) (\hat{x}_{\alpha t} \cdot (\nu \circ \hat{x}_\alpha)) ((\nu \circ \hat{x}_\alpha) \cdot \chi) do_{\hat{g}_\alpha} \\ &\quad + \int_{\mathcal{M}} \hat{G}_\alpha^{-1} \nabla_{\mathcal{M}} \hat{x}_\alpha : \nabla_{\mathcal{M}} \chi do_{\hat{g}_\alpha} + \int_{\mathcal{M}} \nabla_{\mathcal{M}} \hat{x}_\alpha : \nabla_{\mathcal{M}} ((P \circ \hat{x}_\alpha) \chi) do_h, \end{aligned} \quad (6.5)$$

where we used the fact that  $do_h = \hat{\rho} do_{\hat{g}_\alpha}$  in the last term. In order to derive the equivalent formulation of (6.5) on the moving hypersurface  $\Gamma(t) := \hat{x}_\alpha(\mathcal{M}, t) \subset \mathbb{R}^{n+1}$ , we set  $u := \hat{x}_\alpha \circ \hat{x}_\alpha^{-1}$ ,  $\rho := \hat{\rho} \circ \hat{x}_\alpha^{-1}$  and  $\eta := \chi \circ \hat{x}_\alpha^{-1}$  and obtain the following weak formulation on  $\Gamma(t)$ .

**Theorem 5.** *Let  $\alpha \in (0, \infty)$  and  $\mathcal{M}$  be a smooth,  $n$ -dimensional, closed, connected hypersurface in  $\mathbb{R}^{n+1}$ . Furthermore, let  $h$  be the metric on  $\mathcal{M} \subset \mathbb{R}^{n+1}$  which is induced by the Euclidean metric  $\mathfrak{e}$  of the ambient space and let  $\hat{x}_\alpha : \mathcal{M} \times [0, T) \rightarrow \mathbb{R}^{n+1}$  evolve according to the reparametrized mean curvature flow (6.4). Then the identity map  $u := \text{id}_{\Gamma(t)}$  on  $\Gamma(t)$  satisfies*

$$\begin{aligned} 0 &= \int_{\Gamma(t)} (\alpha \rho) \partial^\bullet u \cdot \eta d\sigma + \int_{\Gamma(t)} (1 - \alpha \rho) (\partial^\bullet u \cdot \nu) (\nu \cdot \eta) d\sigma \\ &\quad + \int_{\Gamma(t)} \nabla_{\Gamma(t)} u : \nabla_{\Gamma(t)} \eta d\sigma + \int_{\Gamma(t)} \hat{H}_\alpha^{-1} \nabla_{\Gamma(t)} u : \nabla_{\Gamma(t)} (P \eta) \rho d\sigma, \end{aligned}$$

where  $\hat{H}_\alpha(t)$  is defined as in (5.15) and  $\hat{H}_\alpha^{-1} \nabla_{\Gamma(t)} u : \nabla_{\Gamma(t)} (P \eta) := (\hat{H}_\alpha^{-1})^{\gamma\kappa} \underline{D}'_\gamma u_\beta \underline{D}'_\kappa (P \eta)_\beta$ . The weight function  $\rho$  is given by  $\rho = \sqrt{\det \hat{H}_\alpha}$ .

*Proof.* By applying (5.14) as well as (5.17) we obtain the first three integrals. For the last term we combine (5.16) and (5.23), which leads to

$$\begin{aligned}
\nabla_{\mathcal{M}} \hat{x}_\alpha : \nabla_{\mathcal{M}} \chi &= \left( (\hat{H}_\alpha^{-1})^{\beta\gamma} \underline{D}'_\gamma (\hat{x}_\alpha^{-1})^\rho \right) \circ \hat{x}_\alpha \underline{D}_\rho \chi_\beta \\
&= \left( (\hat{H}_\alpha^{-1})^{\beta\gamma} \underline{D}'_\gamma (\hat{x}_\alpha^{-1})^\rho \right) \circ \hat{x}_\alpha (\underline{D}'_\kappa \eta_\beta) \circ \hat{x}_\alpha \underline{D}_\rho (\hat{x}_\alpha)^\kappa \\
&= \left( (\hat{H}_\alpha^{-1})^{\beta\kappa} \underline{D}'_\kappa \eta_\beta \right) \circ \hat{x}_\alpha = \left( (\hat{H}_\alpha^{-1})^{\beta\gamma} P_{\gamma\kappa} \underline{D}'_\kappa \eta_\beta \right) \circ \hat{x}_\alpha \\
&= \left( (\hat{H}_\alpha^{-1})^{\kappa\gamma} P_{\gamma\beta} \underline{D}'_\kappa \eta_\beta \right) \circ \hat{x}_\alpha = \left( (\hat{H}_\alpha^{-1})^{\gamma\kappa} \underline{D}'_\gamma u_\beta \underline{D}'_\kappa \eta_\beta \right) \circ \hat{x}_\alpha \\
&= \left( \hat{H}_\alpha^{-1} \nabla_\Gamma u : \nabla_\Gamma \eta \right) \circ \hat{x}_\alpha,
\end{aligned}$$

where we have used  $\hat{H}_\alpha^{-1} P = P \hat{H}_\alpha^{-1}$ , which can be easily seen from (5.22), and  $P = \nabla_\Gamma u$ . Similar as in (5.13), it follows from (5.21) that

$$\det \hat{H}_\alpha \circ \hat{X}_\alpha = \frac{\det h_{ij}}{\det \hat{g}_{\alpha ij}},$$

and thus  $\rho = \sqrt{\det \hat{H}_\alpha}$ . □

**Remark 9.** The reparametrized mean curvature flow (6.5) is a gradient flow in the sense that

$$\begin{aligned}
\int_{\mathcal{M}} \hat{G}_\alpha^{-1} \nabla_{\mathcal{M}} \hat{x}_\alpha : \nabla_{\mathcal{M}} \chi d\hat{g}_\alpha &= \frac{d}{d\epsilon} A(\hat{x}_\alpha + \epsilon \chi) \Big|_{\epsilon=0} \\
\int_{\mathcal{M}} \nabla_{\mathcal{M}} \hat{x}_\alpha : \nabla_{\mathcal{M}} ((P \circ \hat{x}_\alpha) \chi) d\hat{g}_\alpha &= \frac{d}{d\epsilon} E(a(\hat{x}_\alpha + \epsilon \chi)) \Big|_{\epsilon=0}
\end{aligned}$$

where  $A(\hat{x}_\alpha) := \int_{\mathcal{M}} \sqrt{\det \hat{G}_\alpha} d\hat{g}_\alpha = \int_{\mathcal{M}} 1 d\hat{g}_\alpha$  is the area functional of  $\Gamma := \hat{x}_\alpha(\mathcal{M})$ , and  $E(\hat{x}_\alpha) := \frac{1}{2} \int_{\mathcal{M}} |\nabla_{\mathcal{M}} \hat{x}_\alpha|^2 d\hat{g}_\alpha$  is the Dirichlet energy of the map  $\hat{x}_\alpha : \mathcal{M} \rightarrow \Gamma$ . Please note that in the second equation only tangential variations  $a(\hat{x}_\alpha + \epsilon \chi)$  are considered. Here,  $a : \Gamma_\delta \rightarrow \Gamma$  denotes the orthogonal projection onto  $\Gamma$ , that is

$$a(x) = x - d(x)\nu(a(x)) \in \Gamma,$$

where  $x$  is a point in the tubular neighbourhood  $\Gamma_\delta := \{x \in \mathbb{R}^{n+1} \mid |d(x)| < \delta\}$  of width  $\delta > 0$  about  $\Gamma$  and  $d(\cdot)$  denotes the oriented distance function to  $\Gamma$ , see [10] for more details.

## 6.2 Numerical scheme for a variant of the DeTurck trick

We now present an algorithm for the computation of the reparametrized mean curvature flow (6.4) based on the weak formulation in Theorem 5.

**Algorithm 3.** Let  $\alpha \in (0, \infty)$ . For a given initial polyhedral hypersurface  $\Gamma_h^0 = \hat{x}_h^0(\mathcal{M}_h)$  with  $\hat{x}_h^0 \in \mathcal{S}(\mathcal{M}_h)^{n+1}$ , set  $y_h^0 := (\hat{x}_h^0)^{-1} \in \mathcal{S}(\Gamma_h^0)^{n+1}$  and determine for  $m = 0, \dots, M_\tau - 1$  solutions  $u_h^{m+1} \in \mathcal{S}(\Gamma_h^m)^{n+1}$  such that

$$\begin{aligned}
&\frac{1}{\tau} \int_{\Gamma_h^m} (\alpha \rho_h^m) I_h(u_h^{m+1} \cdot \eta_h) d\sigma + \frac{1}{\tau} \int_{\Gamma_h^m} (1 - \alpha \rho_h^m) I_h((u_h^{m+1} \cdot \tilde{\nu}_h^m)(\tilde{\nu}_h^m \cdot \eta_h)) d\sigma \\
&+ \int_{\Gamma_h^m} \nabla_{\Gamma_h^m} u_h^{m+1} : \nabla_{\Gamma_h^m} \eta_h d\sigma + \int_{\Gamma_h^m} (\hat{H}_h^m)^{-1} \nabla_{\Gamma_h^m} u_h^{m+1} : \nabla_{\Gamma_h^m} (I_h(P_h^m \eta_h)) \rho_h^m d\sigma \\
&= \frac{1}{\tau} \int_{\Gamma_h^m} (\alpha \rho_h^m) I_h(\tilde{\nu}_h^m \cdot \eta_h) d\sigma + \frac{1}{\tau} \int_{\Gamma_h^m} (1 - \alpha \rho_h^m) I_h((\tilde{\nu}_h^m \cdot \tilde{\nu}_h^m)(\tilde{\nu}_h^m \cdot \eta_h)) d\sigma, \quad \forall \eta_h \in \mathcal{S}(\Gamma_h^m)^{n+1},
\end{aligned}$$

where  $\nu_h^m$  is the piecewise constant outward unit normal to  $\Gamma_h^m$ ,  $\tilde{u}_h^m := id|_{\Gamma_h^m}$ , and

$$\begin{aligned}
\hat{H}_h^m &:= (\nabla_{\Gamma_h^m} y_h^m)^T \nabla_{\Gamma_h^m} y_h^m + \nu_h^m \otimes \nu_h^m, \text{ and } \rho_h^m := \sqrt{\det \hat{H}_h^m}, \\
\tilde{\nu}_h^m &\in \mathcal{S}(\Gamma_h^m)^{n+1} \text{ such that } \tilde{\nu}_h^m(p_j) = \frac{\sum_{T \in \sigma_j} \nu_h^m|_T |T|}{|\sum_{T \in \sigma_j} \nu_h^m|_T |T|}, \text{ with } \sigma_j = \{T \in \mathcal{T}_h^m \mid p_j \in T\}, \\
P_h^m &\in \mathcal{S}(\Gamma_h^m)^{(n+1) \times (n+1)} \text{ such that } P_h^m(p_j) := \mathbf{1} - \tilde{\nu}_h^m(p_j) \otimes \tilde{\nu}_h^m(p_j) \text{ for all vertices } p_j \in \Gamma_h^m.
\end{aligned}$$

The hypersurface  $\Gamma_h^{m+1}$  is defined by

$$\Gamma_h^{m+1} := u_h^{m+1}(\Gamma_h^m),$$

and  $y_h^{m+1} \in \mathcal{S}(\Gamma_h^{m+1})^{n+1}$  is set to be

$$y_h^{m+1} := y_h^m \circ (u_h^{m+1})^{-1}.$$

## 7 Numerical results for the mean curvature flow

We implemented Algorithms 2 and 3 as well as the benchmark algorithm (2.25) in [3] for the computation of the mean curvature flow within the Finite Element Toolbox ALBERTA, see [28]. For Algorithm 2 one has to solve the linear system

$$\frac{1}{\tau} \sum_{\gamma=1}^{n+1} \sum_{j=1}^N \widetilde{M}_{ij\beta\gamma} \mathbf{U}^{j\gamma} + \sum_{\gamma=1}^{n+1} \sum_{j=1}^N S_{ij\beta\gamma} \mathbf{U}^{j\gamma} + \sum_{\gamma=1}^{n+1} \sum_{j=1}^N B_{ij\beta\gamma} \mathbf{U}^{j\gamma} = \frac{1}{\tau} \sum_{\gamma=1}^{n+1} \sum_{j=1}^N \widetilde{M}_{ij\beta\gamma} \mathbf{U}_{old}^{j\gamma}, \quad (7.1)$$

for  $i = 1, \dots, N$ ,  $\beta = 1, 2$ , whereas for Algorithm 3 one has to assemble the following system,

$$\frac{1}{\tau} \sum_{\gamma=1}^{n+1} \sum_{j=1}^N M_{ij\beta\gamma} \mathbf{U}^{j\gamma} + \sum_{\gamma=1}^{n+1} \sum_{j=1}^N S_{ij\beta\gamma} \mathbf{U}^{j\gamma} + \sum_{\gamma=1}^{n+1} \sum_{j=1}^N D_{ij\beta\gamma} \mathbf{U}^{j\gamma} = \frac{1}{\tau} \sum_{\gamma=1}^{n+1} \sum_{j=1}^N M_{ij\beta\gamma} \mathbf{U}_{old}^{j\gamma}. \quad (7.2)$$

Here,  $u_h^{m+1} = \sum_{\gamma=1}^{n+1} \sum_{j=1}^N \mathbf{U}^{j\gamma} \phi_j e_\gamma$  is the unknown parametrization of the discrete surface  $\Gamma_h^{m+1}$  and  $\tilde{u}_h^m = \sum_{\gamma=1}^{n+1} \sum_{j=1}^N \mathbf{U}_{old}^{j\gamma} \phi_j e_\gamma$  is the identity function on  $\Gamma_h^m$ . Please note that the basis functions are defined on the changing polyhedral surfaces  $\Gamma_h^m$ , that is  $\phi_j = \phi_j^m$ . We usually drop the superscript  $m$  for the sake of convenience. The vector  $\mathbf{U}_{old}$  is just given by the solution vector  $\mathbf{U}$  from the previous time step. The matrices  $\widetilde{M} := (\widetilde{M}_{ij\beta\gamma})$ ,  $S := (S_{ij\beta\gamma})$ ,  $B := (B_{ij\beta\gamma}) \in \mathbb{R}^{((n+1)N) \times ((n+1)N)}$ , and respectively, the matrices  $M := (M_{ij\beta\gamma})$ ,  $S := (S_{ij\beta\gamma})$  and  $D := (D_{ij\beta\gamma})$  can be assembled by summing up the non-vanishing components coming from the element matrices, which are

$$\begin{aligned} \widetilde{M}_{ij\beta\gamma}(T) &= (\alpha \delta_{\beta\gamma} + (1 - \alpha) \nu_{h\beta}^m(T) \nu_{h\gamma}^m(T)) \int_T \phi_i \phi_j d\sigma, \\ S_{ij\beta\gamma}(T) &= \delta_{\beta\gamma} \int_T \nabla_{\Gamma_h^m} \phi_i \cdot \nabla_{\Gamma_h^m} \phi_j d\sigma, \\ B_{ij\beta\gamma}(T) &= \delta_{\beta\gamma} \int_T \phi_i (\nabla_{\Gamma_h^m} \phi_j)_\iota \left( \hat{H}_h^m(T)^{-1} (\nabla_{\Gamma_h^m} y_h^m)^T w_h^m \right)^\iota d\sigma, \\ M_{ij\beta\gamma}(T) &= (\alpha \rho_h^m(T) \delta_{\beta\gamma} + (1 - \alpha \rho_h^m(T)) \tilde{\nu}_{h\beta}^m(p_i) \tilde{\nu}_{h\gamma}^m(p_i)) \delta_{ij} \int_T \phi_i d\sigma, \\ D_{ij\beta\gamma}(T) &= (\delta_{\beta\gamma} - \tilde{\nu}_{h\beta}^m(p_i) \tilde{\nu}_{h\gamma}^m(p_i)) \left( \hat{H}_h^m(T)^{-1} \right)^{\kappa\iota} \rho_h^m(T) \int_T (\nabla_{\Gamma_h^m} \phi_i)_\kappa (\nabla_{\Gamma_h^m} \phi_j)_\iota d\sigma. \end{aligned}$$

Here,  $\phi_i$  and  $\phi_j$  are the nodal basis functions associated with the vertices  $p_i$  and  $p_j$  of the simplex  $T$ . Please note that the unit normal vector  $\nu_h^m(T)$ , the matrix  $\hat{H}_h^m(T)$  and the weight function  $\rho_h^m(T)$  are constant on each simplex. The linear systems (7.1) and (7.2) can be solved by the biconjugate gradient stabilized method. The vector  $w_h^m$  in Algorithm 2 can be easily computed by inverting a mass matrix. The initial polyhedral hypersurface  $\Gamma_h^0$  is constructed by mapping the vertices of a triangulation of the reference hypersurface  $\mathcal{M}_h$ , which is the unit sphere in Example 1 and 2 and a torus in Example 3, onto the initial smooth hypersurface. The linear interpolation of the image then gives  $\Gamma_h^0$ . By this means, the inverse  $y_h^0 := (\hat{x}_h^0)^{-1} = \sum_{\gamma=1}^{n+1} \sum_{j=1}^N \mathbf{Y}^{j\gamma} \phi_j e_\gamma$  is determined by the position vectors  $(\mathbf{Y}^{j\gamma})_{\gamma=1, \dots, n+1}$  for  $j = 1, \dots, N$ , of the vertices of the reference hypersurface  $\mathcal{M}_h$ . Please note that the vector  $\mathbf{Y}$  is constant in time and that only the basis functions change in each time step  $m$ , that is  $y_h^m = \sum_{\gamma=1}^{n+1} \sum_{j=1}^N \mathbf{Y}^{j\gamma} \phi_j^m e_\gamma$  for all  $m$ . In the following, we will compare the performance of Algorithms 2 and 3 as well as of the benchmark scheme (2.25) in [3], defined by the equation

$$\frac{1}{\tau} \int_{\Gamma_h^m} I_h((u_h^{m+1} \cdot \bar{\nu}_h^m)(\bar{\nu}_h^m \cdot \eta_h)) + \int_{\Gamma_h^m} \nabla_{\Gamma_h^m} u_h^{m+1} : \nabla_{\Gamma_h^m} \eta_h d\sigma = \frac{1}{\tau} \int_{\Gamma_h^m} I_h((\tilde{u}_h^m \cdot \bar{\nu}_h^m)(\bar{\nu}_h^m \cdot \eta_h)),$$

where the definition of  $\bar{\nu}_h^m \in \mathcal{S}(\Gamma_h^m)^{n+1}$ , see (2.7) in [3], slightly differs from our definition of  $\tilde{\nu}_h^m$  in Algorithm 3. If we formally set  $\alpha = 0$  in Algorithm 3, the main difference between Algorithm 3 and the BGN-scheme is the second order term given by the matrix  $D$ . In our numerical tests, we will focus on the mesh properties of the schemes. A good quantity to evaluate the mesh quality of a polyhedral surface is

$$\sigma_{max} := \max_{T \in \mathcal{T}_h} \frac{h(T)}{r(T)}, \quad (7.3)$$

where  $h(T)$  denotes the diameter of the simplex  $T$  and  $r(T)$  is the radius of the largest ball contained in the simplex. Small values of  $\sigma_{max}$  imply that there are no simplices with sharp angles.

### Example 1:

The initial surface, approximated by the polyhedral surface in Figure 14b, is given by the local parametrization

$$X_0(\theta, \varphi) := \begin{pmatrix} \cos \varphi \\ (0.7 \cos^2 \varphi + 0.3) \cos \theta \sin \varphi \\ (0.7 \cos^2 \varphi + 0.3) \sin \theta \sin \varphi \end{pmatrix}, \quad \theta \in [0, 2\pi), \varphi \in [0, \pi].$$

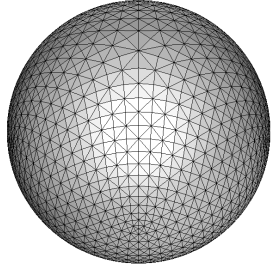
The discrete reference hypersurface  $\mathcal{M}_h$  is a triangulation of the unit sphere, see Figure 14a. The simulation in Figure 14 shows that the mean curvature flow for this initial surface develops a neck pinch singularity in finite time, see Figures 14i or 14j. Please note that under Algorithm 3 the simplices at the poles have a greater area compared to the simplices at the neck of the surface, see Figures 14c, 14e and 14i, whereas under the BGN-scheme (2.25) in [3] this is not the case. However, this does not mean that the mesh properties of Algorithm 3 are not good. On the contrary, the area of the simplices can be easily reduced by local mesh refinements, whereas the size of the quantity  $\sigma_{max}$  almost remains unchanged under local mesh refinements. It is therefore much more preferable to have an algorithm that produces meshes with small values of  $\sigma_{max}$  rather than meshes with simplices of the same area size. The comparison of the simplices at the surface neck, see Figures 14g and 14h, gives a first hint that Algorithm 3 is indeed able to produce good meshes, that is without any sharp angles. This observation is confirmed in a systematic study of  $\sigma_{max}$  for different choices of the parameter  $\alpha$ . Figure 19 shows that Algorithm 3 clearly outperform the BGN-scheme for  $\alpha \leq 0.1$ . For  $\alpha = 1.0$  the result of Algorithm 3 looks similar to the result of the BGN-scheme, see also Figure 15. In Figure 18, the mesh properties of Algorithms 2 and 3 are compared. For small values of  $\alpha$ , both schemes show a similar performance, although Algorithm 3 behaves slightly better close to the surface singularity. However, this is not always the case, see for example Figure 23, where Algorithm 2 shows better behaviour at the singularity. For  $\alpha = 1.0$  and  $\alpha = 0.1$ , Algorithm 2 generally seems to produce better meshes. In the following, we will mainly focus on the comparison of Algorithm 3 and the BGN-scheme, since Algorithms 2 and 3 provide similar behaviour. Figure 16 shows the decrease of the discrete surface area under the mean curvature flow. Please note that for small values of  $\alpha$  and for times close to the starting point, the area of the surface is not monotonically decreasing under Algorithm 3. This behaviour is due to relatively large tangential motions that occur for small choices of  $\alpha$  if the initial surface parametrization  $x_0 : \mathcal{M} \rightarrow \Gamma(0)$  is not harmonic. Although, Figure 17 indicates that the initial increase of the surface area can be reduced by choosing smaller time step sizes  $\tau$ , an improved time discretization might solve the problem also for larger time step sizes. This is an open problem that should be addressed in further research. Figure 20 illustrates the influence of decreasing maximal diameters  $h = \max_T h(T)$  on the behaviour of the mesh quality  $\sigma_{max}$ .

### Example 2:

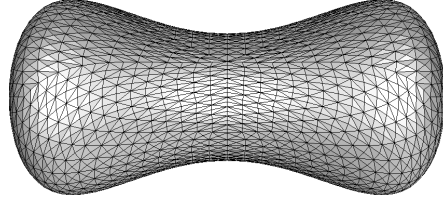
We now change the local surface parametrization to be

$$X_0(\theta, \varphi) := \begin{pmatrix} \cos \varphi \\ (0.6 \cos^2 \varphi + 0.4) \cos \theta \sin \varphi \\ (0.6 \cos^2 \varphi + 0.4) \sin \theta \sin \varphi \end{pmatrix}, \quad \theta \in [0, 2\pi), \varphi \in [0, \pi].$$

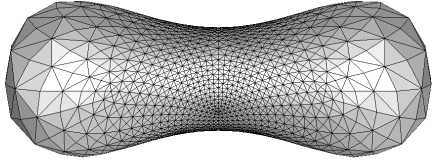
The radius at the neck of the initial surface is now equal to 0.4 instead of 0.3 as in Example 1. In this case, the mean curvature flow does not develop a neck pinch singularity, but shrinks to



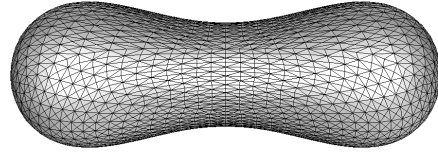
(a) Reference surface for Algorithm 3.



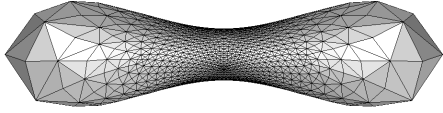
(b) Surface at time  $t = 0.0$ . The surface area is 5.549.



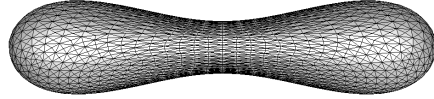
(c) Algorithm 3 at time  $t = 0.0301$ . The surface area is 3.296.



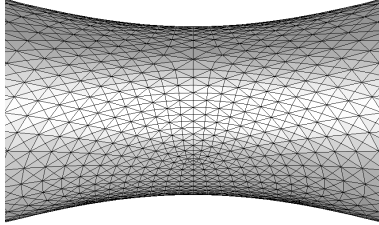
(d) BGN-scheme at time  $t = 0.0301$ . The surface area is 3.111.



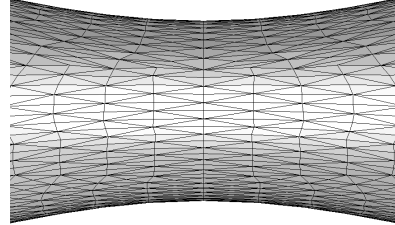
(e) Algorithm 3 at time  $t = 0.0556$ . The surface area is 1.208.



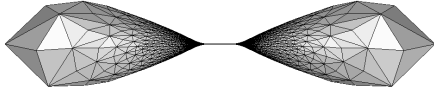
(f) BGN-scheme at time  $t = 0.0556$ . The surface area is 0.893.



(g) Algorithm 3 at time  $t = 0.0556$ . The surface area is 1.208. Enlarged section of the surface neck.



(h) BGN-scheme at time  $t = 0.0556$ . The surface area is 0.893. Enlarged section of the surface neck.

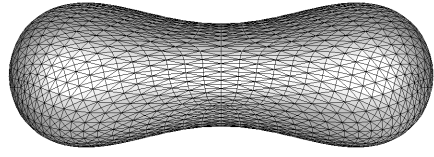


(i) Algorithm 3 at time  $t = 0.0603$ . The surface area is 0.697.

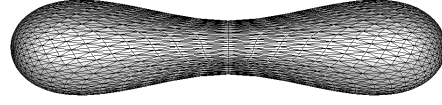


(j) BGN-scheme at time  $t = 0.0596$ . The surface area is 0.389.

Figure 14: Comparison of Algorithm 3 for  $\alpha = 10^{-4}$  and the BGN-scheme (2.25) in [3]. The time step size for both schemes was  $\tau = 10^{-4}$ . The mesh had 5120 triangles and 2562 vertices. The images are rescaled. See Example 1 of Section 7 for further details.



(a) Algorithm 3 at time  $t = 0.0301$ . The surface area is 3.127.



(b) Algorithm 3 at time  $t = 0.0556$ . The surface area is 0.923.

Figure 15: Results of Algorithm 3 for  $\alpha = 1$ . The time step size was  $\tau = 10^{-4}$ . The images are rescaled. See Figures 14c and 14e for the corresponding results with  $\alpha = 10^{-4}$ . See Example 1 of Section 7 for further details.

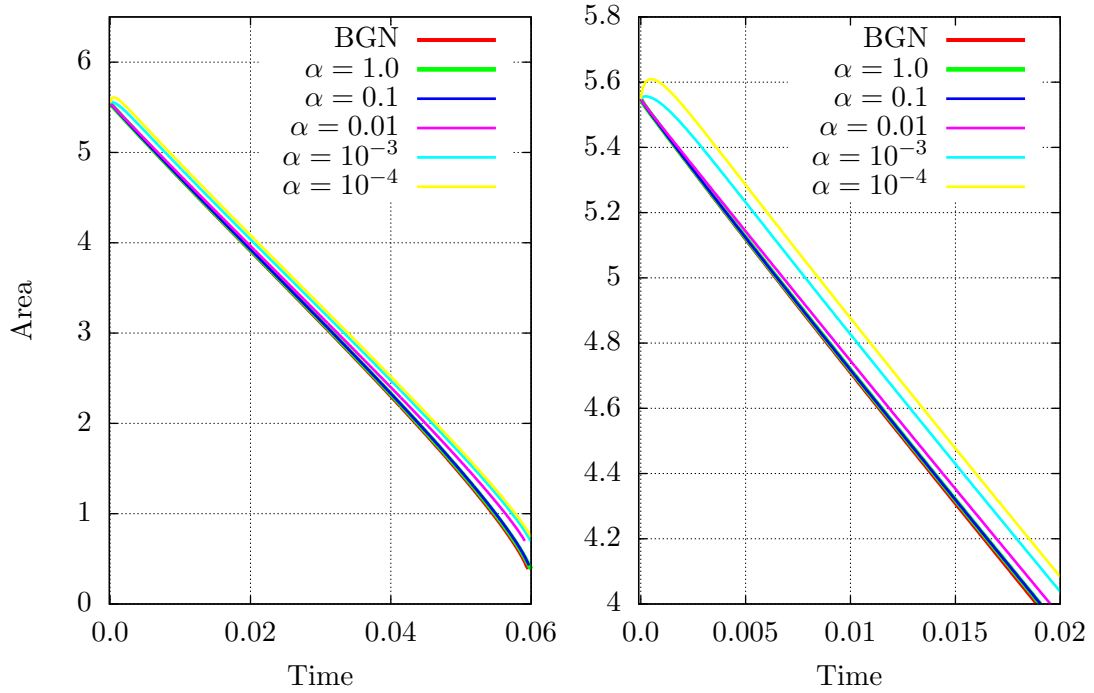


Figure 16: The images show the behaviour of the surface area for the BGN-scheme (2.25) in [3] and for Algorithm 3 for different choices of  $\alpha$ . The initial surface is shown in Figure 14b. The time step size was chosen as  $\tau = 10^{-4}$ . The right image shows an enlarged section for small times  $t$ . In general, for small  $\alpha$  and small times  $t$ , the area of the solution of the  $\alpha$ -scheme is not monotonically decreasing, see for example the solution for  $\alpha = 10^{-4}$  in the right picture. However, smaller time step sizes  $\tau$  lead to a drop of the absolute increase of the area, see Figure 17. For further details see Example 1 of Section 7.



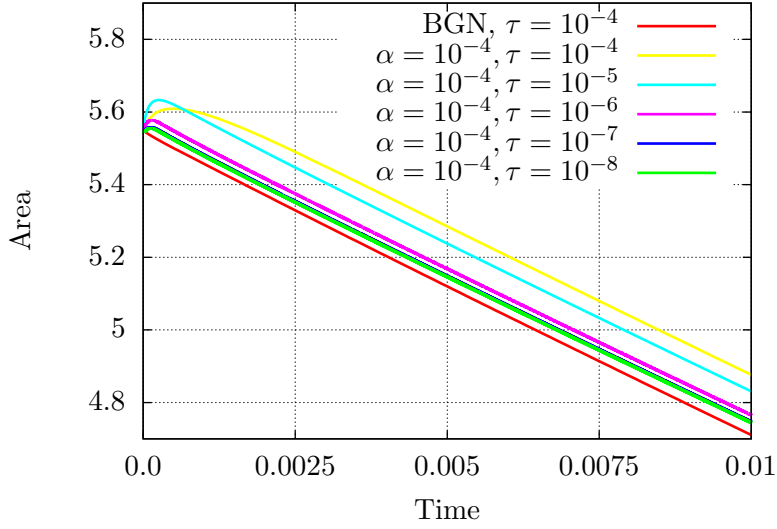


Figure 17: The image shows the behaviour of the area under the mean curvature flow for the BGN-scheme (2.25) in [3] and for Algorithm 3 with  $\alpha = 10^{-4}$  for different time step sizes  $\tau$ . The initial surface of the simulation is shown in Figure 14b. The area increase of the  $\alpha$ -scheme clearly depends on the time step size. Smaller time step sizes lead to a significant drop of the absolute increase of the surface area. See Example 1 of Section 7 for further details.

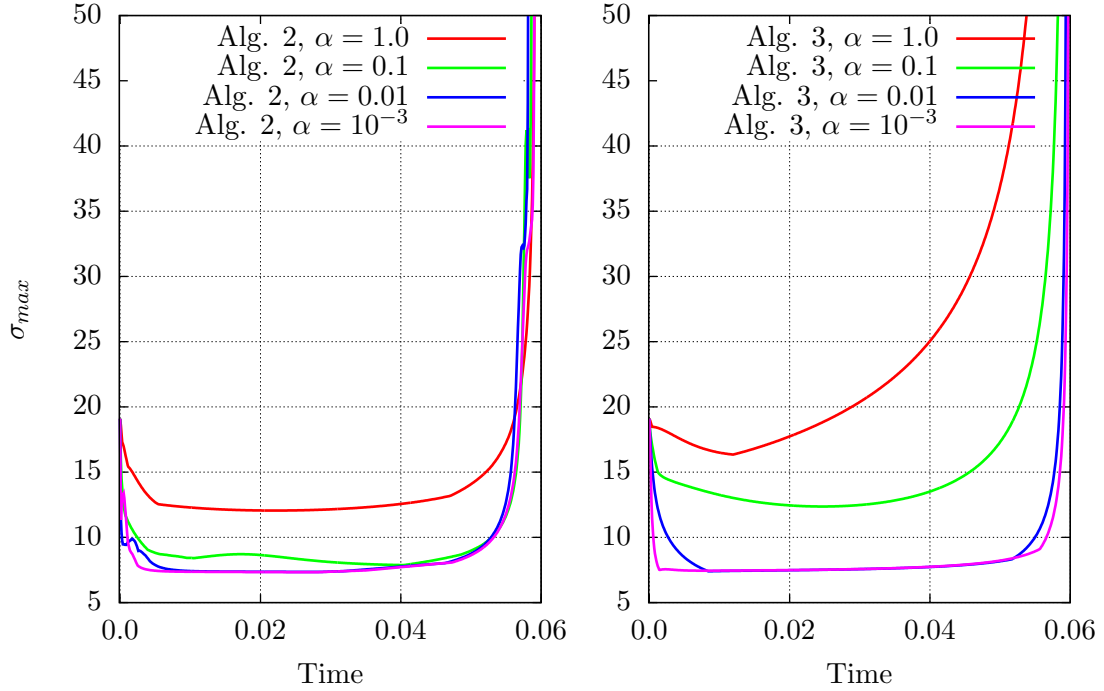


Figure 18: Comparison of Algorithms 2 and 3 with respect to the quantity  $\sigma_{max}$  for different choices of  $\alpha$ . The reference surface and the initial surface are shown in Figures 14a and 14b. The time step size was  $\tau = 10^{-4}$ . The experiment shows that for  $\alpha = 0.01$  and  $\alpha = 10^{-3}$  both algorithms produce good meshes. For these choices of  $\alpha$ , Algorithm 3 seems to have a slightly better behaviour close to the surface singularity, whereas Algorithm 2 has a better mesh performance for  $\alpha = 1.0$  and  $\alpha = 0.1$ . See Example 1 of Section 7 for further details.

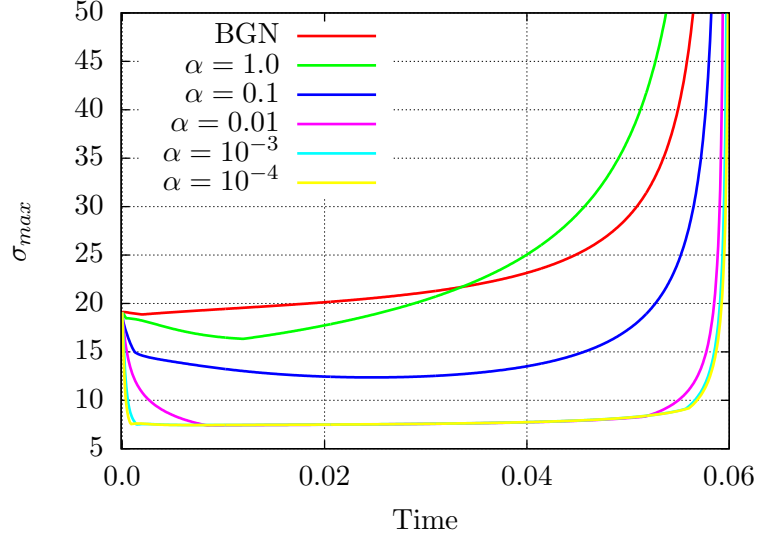


Figure 19: The image shows the behaviour of the mesh quality described by the quantity  $\sigma_{max}$  for the BGN-scheme (2.25) in [3] and for Algorithm 3 for different choices of  $\alpha$ . The initial surface is shown in Figure 14b. The reference surface for the  $\alpha$ -scheme is presented in Figure 14a. In this example, the  $\alpha$ -schemes with  $\alpha \leq 0.1$  outperform the benchmark scheme (2.25) in [3] with respect to the mesh quality. See Example 1 of Section 7 for further details.

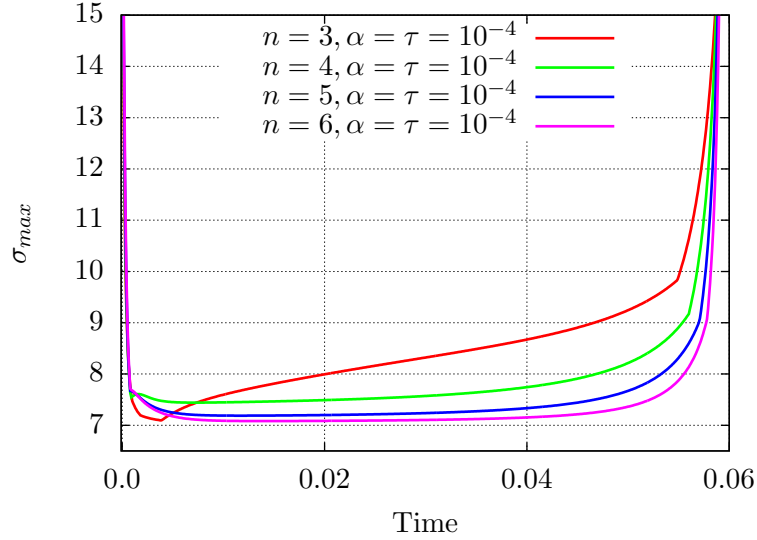


Figure 20: The image shows the behaviour of the mesh quantity  $\sigma_{max}$  for Algorithm 3 with  $\alpha = 10^{-4}$  and for different global mesh refinements  $n$  of the macro triangulation. In each refinement step the simplices are bisected twice so that the maximal diameter of the simplices is approximately halved in each step. The reference surface and the initial surface for  $n = 4$  are shown in Figures 14a and 14b. For smaller mesh sizes (that is a higher number of global mesh refinements) the positive properties of the  $\alpha$ -scheme with respect to the mesh quantity  $\sigma_{max}$  become more pronounced. In Figure 19 the mesh properties of the BGN-scheme (2.25) in [3] and of Algorithm 3 are compared for the global refinement  $n = 4$  and different choices of  $\alpha$ . See Example 1 of Section 7 for further details.

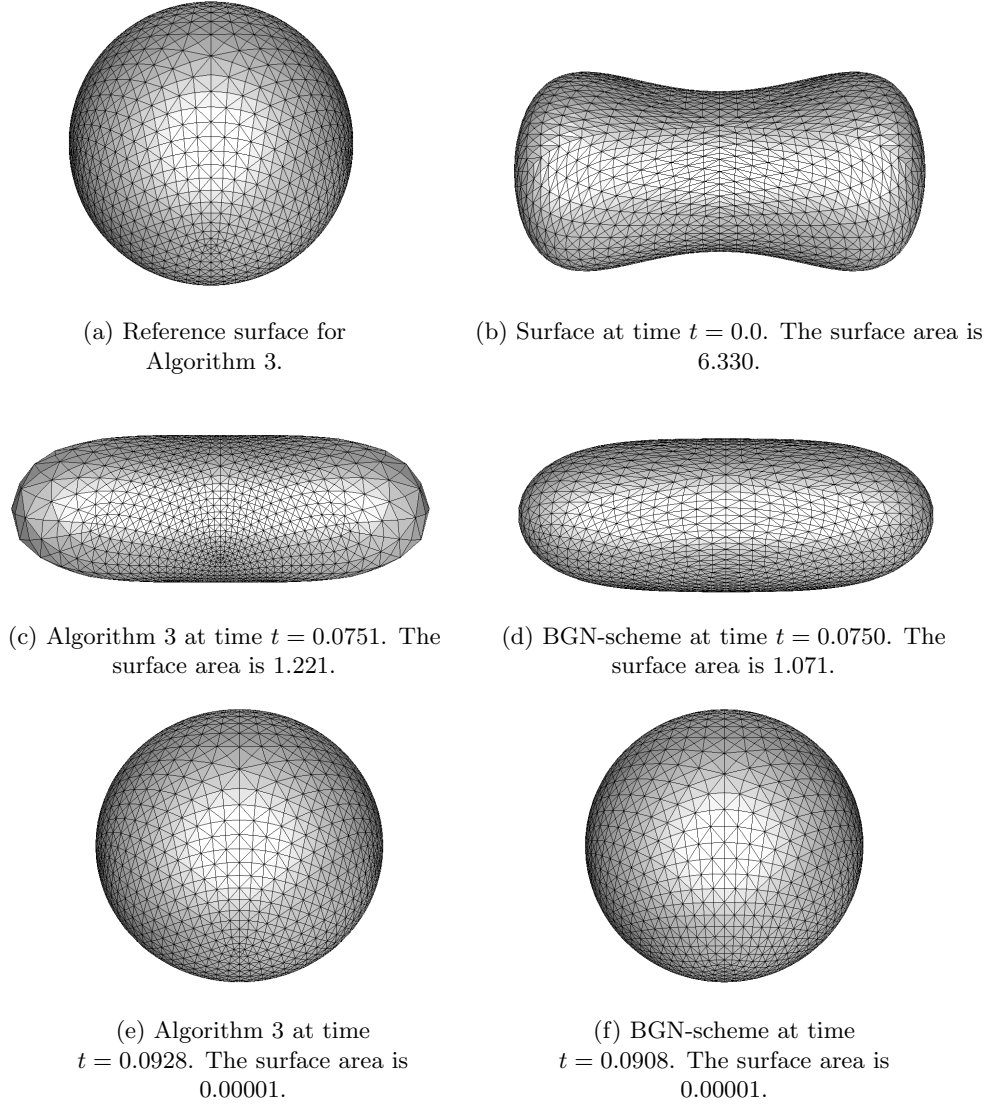


Figure 21: Comparison of Algorithm 3 for  $\alpha = \tau$  and the BGN-scheme (2.25) in [3]. The time step size in both schemes was chosen as  $\tau = 0.01h^2$ , where  $h$  is the maximal diameter of the surface triangulation. The mesh had 5120 triangles and 2562 vertices. The images are rescaled. See Example 2 of Section 7 for further details.

a round sphere, see Figure 21. The decrease of the surface area is presented in Figure 22. For a round shrinking sphere the area should decrease linearly in time. However, for both schemes and fixed time step size  $\tau$ , the area does not decrease linearly close to the singularity of the surface. We, therefore, couple the time step size to the maximal diameter  $h$  of the mesh by  $\tau = 0.001h$  and  $\tau = 0.01h^2$ . This leads to a linear decrease of the surface area also for times close to the surface singularity. In Figure 24 the comparison of the mesh quantity  $\sigma_{max}$  is presented. Away from the singularity, Algorithm 3 outperforms the BGN-scheme. The BGN-scheme, however, shows better mesh behaviour at the singularity. Coupling the parameter  $\alpha$  to the time step size  $\tau$  and thus to the mesh size  $h$ , a good mesh behaviour at the singularity is also achievable for Algorithm 3, see Figure 25. Please note that such a coupling is not necessary for Algorithm 2, see left image in Figure 23. In this example, Algorithm 2 clearly shows better mesh behaviour than Algorithm 3.

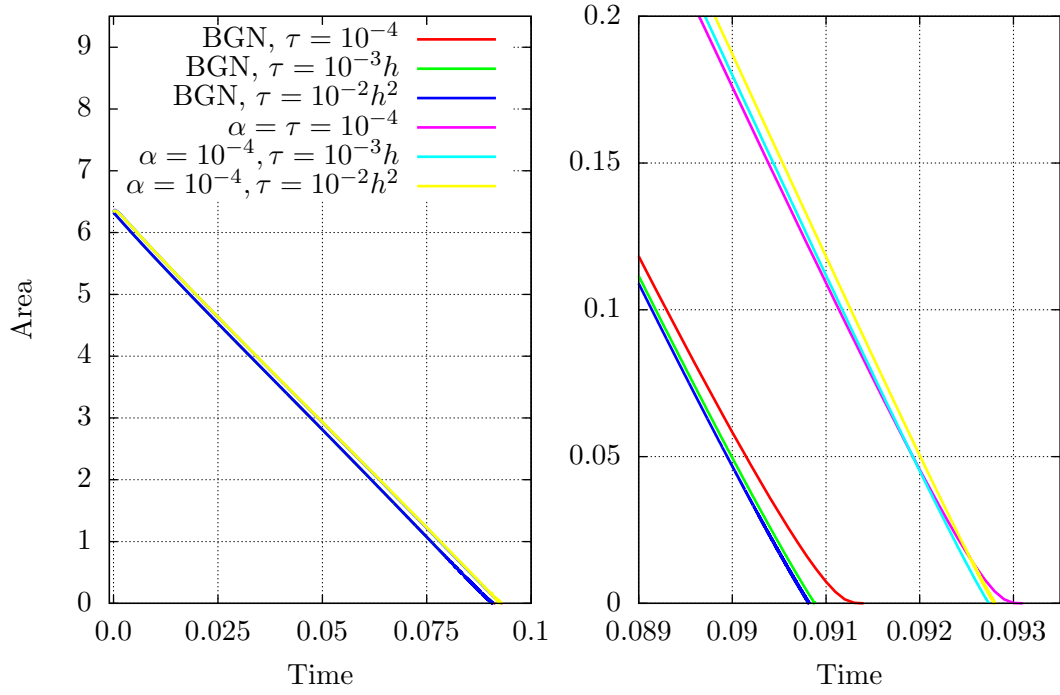


Figure 22: The images show the decrease of the surface area for the BGN-scheme (2.25) in [3] and for Algorithm 3 with  $\alpha = 10^{-4}$ . The initial surface and the reference surface used in Algorithm 3 are presented in Figures 21b and 21a. The right image shows an enlarged section for times close to the surface singularity. The colour code is valid for both images. Different time step sizes were chosen. For a fixed time step size  $\tau = 10^{-4}$ , the area does not decrease linearly close to the singularity (right image). However, by coupling the time step size  $\tau$  to the maximal diameter  $h$  of the triangulation, we also obtain a linear area decrease close to the singularity. See Example 2 of Section 7 for further details.

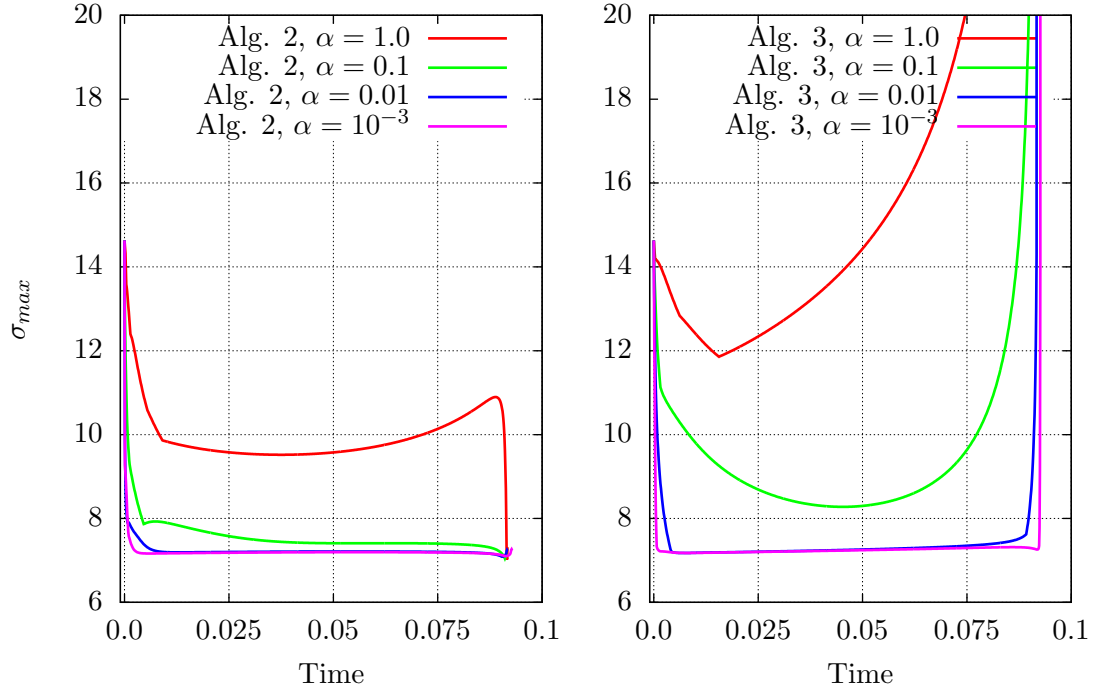


Figure 23: Comparison of Algorithms 2 and 3 with respect to the quantity  $\sigma_{max}$  for different choices of  $\alpha$ . The reference surface and the initial surface are shown in Figures 21a and 21b. The time step size was  $\tau = 10^{-4}$ . For  $\alpha = 0.01$  and  $\alpha = 10^{-3}$  both algorithms have good mesh properties. However, Algorithm 2 outperforms Algorithm 3 for  $\alpha = 1.0$  and  $\alpha = 0.1$  as well as for times close to the surface singularity. For Algorithm 2 it is not necessary to couple the parameter  $\alpha$  to the time step size  $\tau$ , like in Figure 25, in order to obtain a good mesh behaviour at the surface singularity. See Example 2 of Section 7 for further details.

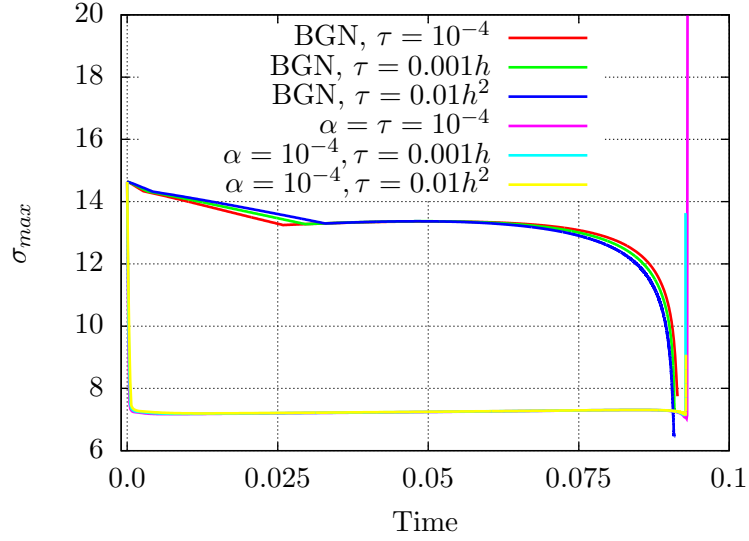


Figure 24: The image shows the behaviour of the mesh quantity  $\sigma_{max}$  for the BGN-scheme (2.25) in [3] and for Algorithm 3 with  $\alpha = 10^{-4}$ . The initial surface and the reference surface for Algorithm 3 are presented in Figures 21b and 21a. Apart from the singularity, Algorithm 3 shows good mesh properties. By coupling  $\alpha$  and  $\tau$ , see Figure 25, the mesh properties of Algorithm 3 also remain controlled close to the surface singularity. For further details see Example 2 of Section 7.

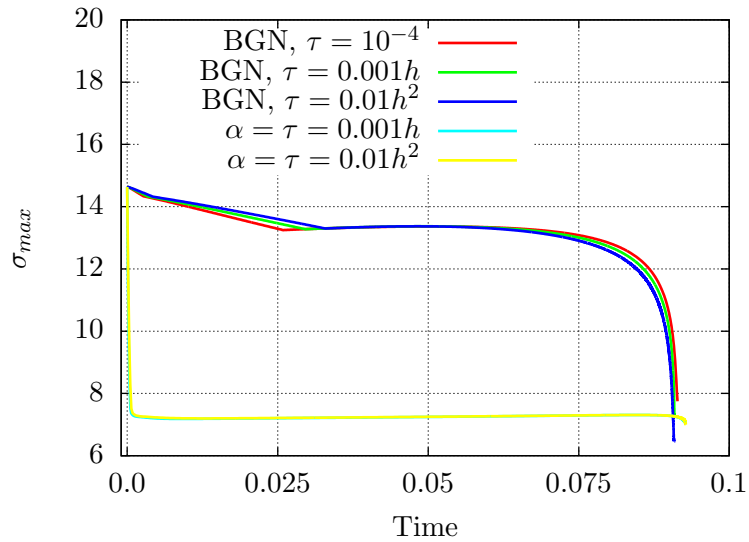


Figure 25: The image shows the behaviour of the mesh quantity  $\sigma_{max}$  for the BGN-scheme (2.25) in [3] and for Algorithm 3 with  $\alpha = 10^{-4}$ . The initial surface and the reference surface for Algorithm 3 are presented in Figures 21b and 21a. The parameter  $\alpha$  was coupled to the time step size  $\tau$  for the choices  $\tau = 0.001h$  and  $\tau = 0.01h^2$ . For these choices Algorithm 3 has good mesh properties even close to the singularity of the surface. See Example 2 of Section 7 for further details.

### Example 3:

In the last example, we consider a surface of genus one given by the local parametrization

$$X_0(\theta, \phi) := \begin{pmatrix} (r_1 + r_2 \cos \varphi) \cos \theta \\ (r_1 + r_2 \cos \varphi) \sin \theta \\ r_2 \sin \varphi + \frac{1}{5} \sin(6\theta) \end{pmatrix}, \quad \theta \in [0, 2\pi), \varphi \in [0, 2\pi).$$

We simulated the mean curvature flow for the radius  $r_1 = 1.0$  and for different choices of the radius  $r_2$ , that is for  $r_2 = 0.7$ ,  $r_2 = 0.6$  and  $r_2 = 0.65$ . For  $r_2 = 0.6$  the surface shrinks to a circle, see Figure 26d, whereas for  $r_2 = 0.7$  it tries to converge to a sphere developing a singularity, see Figure 26f and Figure 4.7 in [10]. Because of this behaviour there must be a range of radii  $r_2$ , where the formation of the singularity becomes unstable in the sense that small changes of the initial triangulation, the mesh size  $h$  or the time step size  $\tau$  can lead to the formation of different singularities. Moreover, the formation of the singularity will even depend on the chosen algorithm. Because of this instability, a rigorous study of the formation of the singularities for radii  $r_2$  close to  $r_2 \approx 0.65$  does not make sense here. Nevertheless, a comparison of Algorithm 3 to the BGN-scheme (2.25) of [3] for times far away from the singularity gives an interesting insight into the mesh behaviour of both algorithms. As shown in Figures 27b and 29, the mesh of the surface degenerates under the BGN-scheme at a time when the surface is still far away from the singularity. In contrast, Algorithm 3 provides good meshes with small values of  $\sigma_{max}$  as long as the surface does not become singular, see Figures 27a and 29. Algorithm 2 again provides a similar behaviour as Algorithm 3.

## 8 Generalizations to other geometric flows

We are aware that the ideas developed in Sections 2, 5 and 6 can be easily generalized to other geometric evolution equations such as the anisotropic mean curvature flow and the Willmore flow. For example, suppose that the time-dependent embedding  $x : \mathcal{M} \times [0, T) \rightarrow \mathbb{R}^{n+1}$  evolves according to

$$\frac{\partial}{\partial t} x = \mathcal{V} \circ x,$$

where  $\mathcal{V}$  denotes the normal velocity of  $\Gamma(t) = x(\mathcal{M}, t)$ . Obviously, this equation of motion can be rewritten in the form

$$\frac{\partial}{\partial t} x = \Delta_{g(t)} x + \tilde{\mathcal{V}} \circ x,$$

with

$$\tilde{\mathcal{V}} \circ x = (\mathcal{V} + H\nu) \circ x.$$

Since  $\tilde{\mathcal{V}}$  is normal to the hypersurface  $\Gamma(t) \subset \mathbb{R}^{n+1}$ , this term remains unaffected under the operations of Sections 2, 5 and 6. Hence, the reparametrized equations equivalent to (5.6) are given by

$$\begin{aligned} (\alpha \mathbf{1} + (1 - \alpha)(\nu \circ \hat{x}_\alpha) \otimes (\nu \circ \hat{x}_\alpha)) \frac{\partial}{\partial t} \hat{x}_\alpha &= \Delta_{\hat{g}_\alpha} \hat{x}_\alpha - (\nabla_{\mathcal{M}} \hat{x}_\alpha) v_\alpha + \tilde{\mathcal{V}} \circ \hat{x}_\alpha \\ &= \mathcal{V} \circ \hat{x}_\alpha - (\nabla_{\mathcal{M}} \hat{x}_\alpha) v_\alpha, \end{aligned}$$

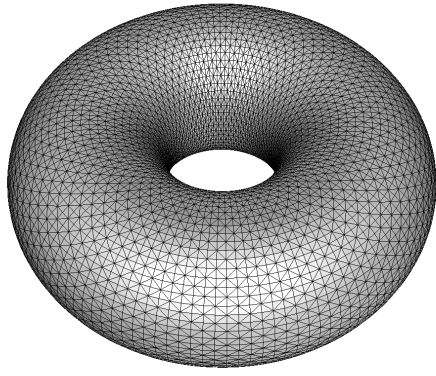
and the reparametrized equations equivalent to (6.4) are

$$(\alpha \hat{\rho} \mathbf{1} + (1 - \alpha \hat{\rho})(\nu \circ \hat{x}_\alpha) \otimes (\nu \circ \hat{x}_\alpha)) \frac{\partial}{\partial t} \hat{x}_\alpha = \mathcal{V} \circ \hat{x}_\alpha + \hat{\rho}(P \circ \hat{x}_\alpha) \Delta_h \hat{x}_\alpha.$$

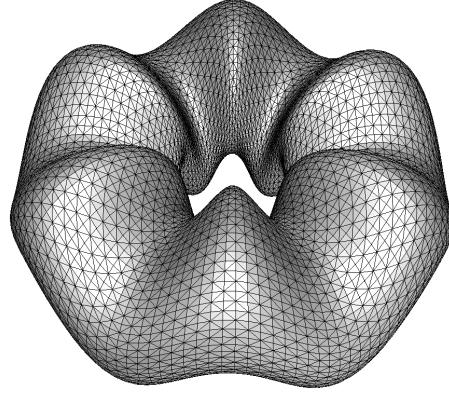
We plan to publish more details including numerical experiments elsewhere.

## 9 Discussion

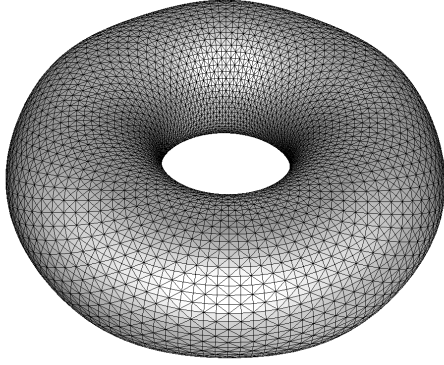
In this paper, we have introduced reformulations of the curve shortening and mean curvature flows based on the DeTurck trick. The main idea was to reparametrize the flows by solutions to the harmonic map heat flow, which leads to (strongly) parabolic PDEs called the curve shortening-DeTurck and mean curvature-DeTurck flows. The motivation for this approach is that the reparametrization should give rise to tangential motions that might be advantageous



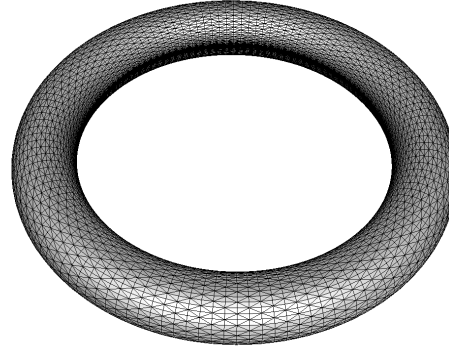
(a) Reference surface for Algorithm 3.



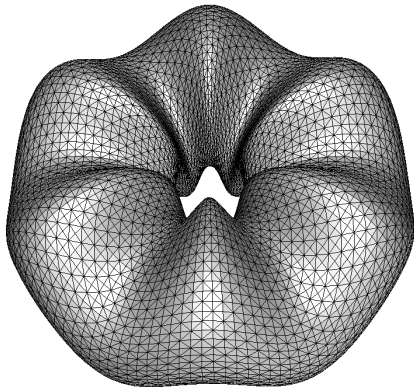
(b) Surface at time  $t = 0.0$ . The radii are  $r_1 = 1.0$  and  $r_2 = 0.6$ . The surface area is 27.56.



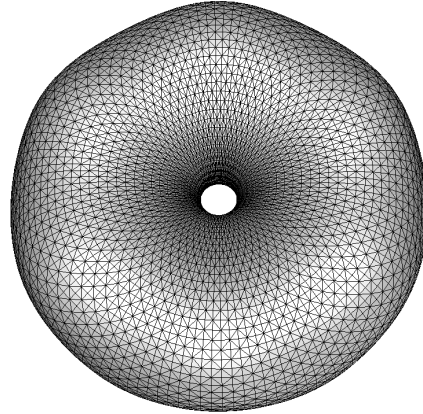
(c) Algorithm 3 at time  $t = 0.1$  for the initial surface 26b. The surface area is 14.91.



(d) Algorithm 3 at time  $t = 0.2$  for the initial surface 26b. The surface area is 3.22.

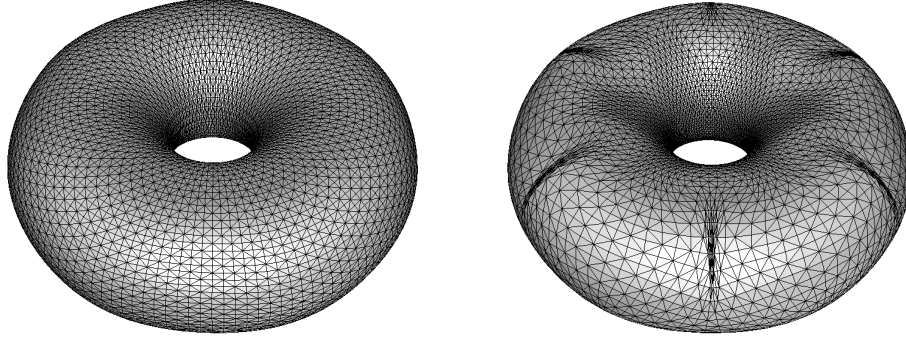


(e) Surface at time  $t = 0.0$ . The radii are  $r_1 = 1.0$  and  $r_2 = 0.7$ . The surface area is 32.28.



(f) Algorithm 3 at time  $t = 0.08$  for the initial surface 26e. The surface area is 21.11.

Figure 26: Simulation of the mean curvature flow for undulating tori with different radii  $r_2$ . The pictures show the numerical results for Algorithm 3 with  $\alpha = 0.01$ . The time step size was  $\tau = 10^{-4}$ . The computational mesh had 16384 triangles and 8385 vertices. The surface singularity strongly depends on the initial radius  $r_2$ . In Figure 26d the torus converges to a circle, whereas in 26f it tries to converge to a sphere developing a singularity, see also Figure 4.7 in [10]. For further details see Example 3 in Section 7.



(a) Algorithm 3 at time  $t = 0.11$ . The surface area is 16.54. (b) BGN-scheme at time  $t = 0.11$ . The surface area is 16.50.

Figure 27: Comparison of Algorithm 3 for  $\alpha = 1.0$  and the BGN-scheme (2.25) in [3]. The radii of the initial surface were  $r_1 = 1.0$  and  $r_2 = 0.65$ , see Figures 26b ( $r_1 = 1.0$  and  $r_2 = 0.6$ ) and 26e ( $r_1 = 1.0$  and  $r_2 = 0.7$ ) for a visualization of the initial surface. The time step size for both schemes was  $\tau = 10^{-5}$ . Both meshes had 16384 triangles and 8385 vertices. In this example the mesh degenerates under the BGN-scheme, whereas the mesh of the  $\alpha$ -scheme evolves in a controlled way. See Figure 29 for the behaviour of the mesh quantity  $\sigma_{max}$  and Example 3 of Section 7 for further details.

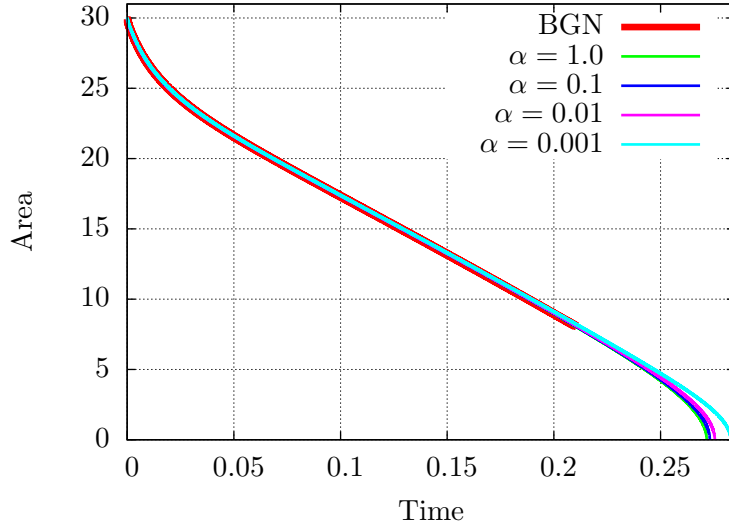


Figure 28: The image shows the area decrease under the BGN-scheme (2.25) in [3] and under Algorithm 3 for different choices of  $\alpha$ . The radii of the initial surface were  $r_1 = 1.0$  and  $r_2 = 0.65$ . See Figure 27 for a visualization of the surface at time  $t = 0.11$ . The time step size was  $\tau = 10^{-5}$ . Please note that the BGN-scheme has to be stopped at time  $t = 0.21023$ , since the mesh fully degenerates, see Figure 29. See Example 3 of Section 7 for further details.



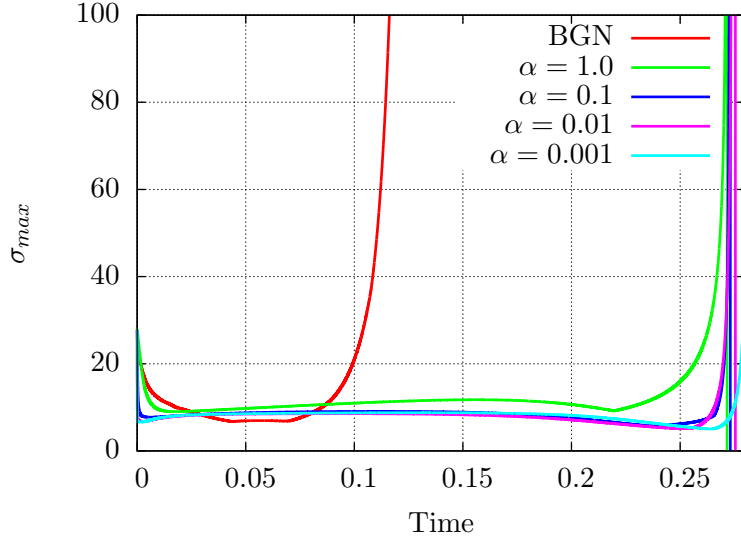


Figure 29: Comparison of the behaviour of the mesh quantity  $\sigma_{max}$  for the BGN-scheme (2.25) in [3] and for Algorithm 3 for different choices of  $\alpha$ . The time step size was  $\tau = 10^{-5}$ . In this example, the mesh degenerates under the BGN-scheme although the surface is still far away from developing a singularity, see Figure 27b. In contrast, the mesh of the  $\alpha$ -scheme does not degenerate until the surface becomes singular. See Example 3 of Section 7 for further details.

in numerical simulations, in particular with respect to the mesh quality. It has turned out in our numerical tests that this is indeed the case. By a straightforward discretization of the reparametrized evolution equations in space and time, we have obtained algorithms with very good mesh properties. For the tangential motions being able to redistribute the mesh vertices efficiently, it was necessary to introduce a variable time scale  $\alpha$  on which the tangential motions take place.

The here presented built-in approach for generating good meshes is clearly more preferable to approaches where the evolution of the flow has to be stopped in order to improve the mesh, see, for example, in [29]. We have therefore compared our schemes to algorithms that are in the spirit of a built-in approach. Namely, we have considered the schemes of Barrett, Garcke and Nürnberg, introduced in [3] and [5]. For the computation of the curve shortening and mean curvature flows, these schemes represent the present benchmarks with respect to the quality of the generated meshes. Our numerical tests show that the algorithms developed on the basis of the DeTurck trick can outperform the BGN-schemes with respect to the mesh quality – at least away from surface singularities. However, we do not regard the better mesh behaviour as the main advantage of our approach, but the fact that the tangential motions in our scheme have an analogue in the continuous case and that our schemes arise from the straightforward discretizations of non-degenerate PDEs. This might be crucial for the numerical analysis of the schemes.

In the following we must clearly distinguish between a hypersurface that evolves according to the mean curvature flow in a purely geometric sense, and its parametrization which might not evolve according to the corresponding PDE. For example, the solutions to our schemes will certainly not approximate the PDE-solution to the mean curvature flow (with vanishing tangential velocity) in the continuous case. However, we hope that under sufficient conditions they are good approximations to the PDE-solution of the mean curvature-DeTurck flow, and hence also approximate the geometric evolution of the mean curvature flow. The fact that we have concrete and unique PDE-candidates to which our discrete solutions might converge is very important if one is interested in the error analysis of our schemes. The scheme for the mean curvature flow in [3] is based on the discretization of the system

$$\frac{\partial x}{\partial t} \cdot (\nu \circ x) = -H \circ x, \quad (H\nu) \circ x = \Delta_{g(t)}x, \quad (9.1)$$

see (1.7) in [3]. As the authors clearly state this system has a whole family of solutions, since the tangential component of the velocity of  $x$  is not prescribed. The question, which then arises, is: Which of these solutions is approximated by the discrete solution of the BGN-scheme? Or,

is there at least a candidate which might be considered in the error analysis of the scheme? Firstly, it is not possible that the solution to the BGN-scheme approximates the solution to the mean curvature flow (2.5), since this solution has vanishing tangential velocity, whereas the desirable mesh properties of the BGN-schemes are exactly due to non-vanishing tangential motions. Another possible answer to this question might be given in Section 4.1 of [3]. There, the authors point out that the discrete solution  $u_h^{m+1} : \Gamma_h^m \rightarrow \Gamma_h^{m+1}$  to their scheme is an approximate discrete conformal map. One could therefore speculate that the discrete solution approximates a parametrization, which evolves according to the mean curvature flow along the normal direction and which in addition satisfy a kind of harmonic map equation in each time step. Apart from the fact that this would couple a PDE of parabolic type to an equation of elliptic type, this cannot be the answer. The reason is that the only surface in the continuous case is the surface  $\Gamma(t)$  and the only Riemannian metric is the metric induced by the Euclidean metric of the ambient space. Hence, this would lead to harmonic maps from  $\Gamma(t)$  onto itself with respect to the same metric. The identity map clearly solves the corresponding harmonic map equation. However, it is not clear how this solution can induce any tangential motions. So, the question remains: Which solution to (9.1) is approximated by the BGN-scheme? Or, is there a non-degenerate PDE with a unique solution that is approximated by the BGN-scheme? To have a candidate to which the discrete solutions might converge is a clear advantage of our approach. This statement holds regardless of the fact whether Algorithms 2 or 3 do converge or not. For the curve-shortening flow, the situation is slightly different. The weak formulation of the BGN-scheme in [5] also depends on a background metric. This metric is actually the same metric which we have used for the curve shortening-DeTurck flow. This strengthens the idea that the BGN-scheme in [5] might approximate the limit of the curve shortening-DeTurck flow (3.1) for  $\alpha \searrow 0$  provided that this limit exists. Whether this view can be made rigorous is an open problem.

In (2.16a) and (2.16b) of [4], the authors introduced numerical schemes for the mean curvature and other geometric flows, which allow to reduce or induce tangential motions. Although, these schemes might seem to have some similarity with the schemes developed in this paper, there are two main differences. Firstly, in contrast to (2.16a) and (2.16b) of [4], our schemes are based on the straightforward discretization of some reparametrized PDEs. Secondly, the tangential motions in our scheme are uniquely determined by the DeTurck trick, and in some sense by the fixed background metric  $h$ , whereas in (2.16a) and (2.16b) of [4] there are no background metrics at all.

Compared to the scheme (2.25) in [3] the implementation of Algorithm 3 requires the assemblage of the additional stiffness matrix  $D$  in each time step, whereas for Algorithm 2 an additional matrix associated to the tangential part in (5.6) has to be assembled, see Section 7 for further details. In both algorithms, the map  $y_h^0$  has to be computed in the first time step, which is, however, trivial if the initial surface is given by an embedding of the reference surface.

From a numerical point of view, the main difference between the approaches in Sections 5 and 6 is that the original DeTurck trick leads to a term, which behaves like a first order term, whereas our variant of the DeTurck trick introduced in Section 6 leads to a term that can be written in divergence form. Whether Algorithm 2 or 3 is generally more advantageous for computations as well as for numerical analysis is an open question.

In our numerical tests, Algorithms 2 and 3 turned out to be numerically stable if the surface was not singular. Nevertheless, it is not clear whether they are unconditionally stable in general. This is still an open problem. In contrast, the BGN-scheme in [3] is known to be unconditionally stable. This does, however, not imply that this scheme is always able to prevent mesh degenerations, see Figure 27. It is not unlikely that the time discretization in Algorithms 2 and 3 has to be improved in order to prove stability. A further question that should be addressed in future research is how the parameter  $\alpha$  can be chosen to obtain an optimal behaviour with respect to the mesh quality.

## Acknowledgements

We would like to thank Klaus Deckelnick and Gerhard Dziuk to call our attention to the fact that their work in [9] can be linked to the DeTurck trick as described above. The second author would also like to thank the Alexander von Humboldt Foundation, Germany, for their financial support by a Feodor Lynen Research Fellowship in collaboration with the University of Warwick, UK.

## References

- [1] C. Baker, *The mean curvature flow of submanifolds of high codimension*, PhD thesis, Australian National University (2010). URL <http://www.arxiv.org/abs/1104.4409v1>
- [2] J. W. Barrett, H. Garcke and R. Nürnberg, *On the variational approximation of combined second and fourth order geometric equations*, SIAM J. Sci. Comput. **29**, no. 3 (2007), 1006–1041.
- [3] J. W. Barrett, H. Garcke and R. Nürnberg, *On the parametric finite element approximation of evolving hypersurfaces in  $\mathbb{R}^3$* , J. Comput. Phys. **227** (2008), 4281–4307.
- [4] J. W. Barrett, H. Garcke and R. Nürnberg, *Parametric Approximation of Willmore Flow and related geometric evolution equations*, SIAM J. Sci. Comput. **31**, no. 1 (2008), 225–253.
- [5] J. W. Barrett, H. Garcke and R. Nürnberg, *The Approximation of Planar Curve Evolutions by Stable Fully Implicit Finite Element Schemes that Equidistribute*, Numer. Methods Partial Differential Equations **27** (2011), 1–30.
- [6] J. W. Barrett, H. Garcke and R. Nürnberg, *Parametric approximation of isotropic and anisotropic elastic flow for closed and open curves*, Numerische Mathematik **120**, no. 3 (2012), 489–542.
- [7] K.-C. Chang, W.-Y. Ding and R. Ye, *Finite-time blow-up of the heat flow of harmonic maps from surfaces*, J. Differential Geometry **36**, no. 2 (1992), 507–515.
- [8] B. Chow, P. Lu and L. Ni, *Hamilton’s Ricci Flow*, Graduate Studies in Mathematics, AMS Science Press (2006).
- [9] K. Deckelnick and G. Dziuk, *On the approximation of the curve shortening flow*, Calculus of Variations, Applications and Computations: Pont-à-Mousson, Pitman Research Notes in Mathematics Series (1994), 100–108.
- [10] K. Deckelnick, G. Dziuk and C. M. Elliott, *Computation of geometric partial differential equations and mean curvature flow*, Acta Numerica **14** (2005), 139–232.
- [11] D. M. DeTurck, *Deforming metrics in the direction of their Ricci tensor*, J. Differential Geometry **18**, no. 11 (1983), 157–162.
- [12] G. Dziuk, *Finite elements for the Beltrami operator on arbitrary surfaces*, Partial Differential Equations & Calculus of Variations (S. Hildebrandt & R. Leis eds), Lecture Notes in Math., Vol. **1357**, Berlin: Springer (1988), 142–155.
- [13] G. Dziuk, *An algorithm for evolutionary surfaces*, Numerische Mathematik **58**, no. 1 (1991), 603–611.
- [14] G. Dziuk and C. M. Elliott, *Finite element methods for surface PDEs*, Acta Numerica **22** (2013), 289–396.
- [15] K. Ecker, *Regularity Theory for Mean Curvature Flow*, Progress in Nonlinear Differential Equations and Their Applications, Vol. **57**, Birkhäuser (2004).
- [16] J. Eells and J. H. Sampson, *Harmonic mappings of Riemannian manifolds*, Amer. J. Math. **86** (1964), 109–160.
- [17] J. Eells and J. C. Wood, *Restrictions on harmonic maps of surfaces*, Topology Vol. **15**, Pergamon Press (1976), 263–266.
- [18] H. Fritz, *Numerical Ricci-DeTurck Flow*, Numerische Mathematik **131**, no. 2 (2015), 241–271.
- [19] R. S. Hamilton, *Three-manifolds with positive Ricci curvature*, J. Differential Geometry **17**, no. 2 (1982), 255–306.
- [20] R. S. Hamilton, *Heat equations in geometry*, Lecture notes, Hawaii (1989).
- [21] R. S. Hamilton, *The formation of singularities in the Ricci flow*, Surveys in Differential Geometry **227** (1995), 7–136.
- [22] T. Y. Hou, J. S. Lowengrub and M. J. Shelley, *Removing the Stiffness from Interfacial Flows with Surface Tension*, J. Comput. Phys. **114** (1994), 312–338.
- [23] C. Mantegazza, *Lecture Notes on Mean Curvature Flow*, Progress in Mathematics, Vol. **290**, Birkhäuser (2010).
- [24] K. Mikula and D. Ševčovič, *Evolution of plane curves driven by a nonlinear function of curvature and anisotropy*, SIAM J. Appl. Math. Vol. **61**, no. 5 (2001), 1473–1501.

- [25] K. Mikula and D. Ševčovič, *A direct method for solving an anisotropic mean curvature flow of plane curves with an external force*, Math. Meth. Appl. Sci. **27** (2004), 1545–1565.
- [26] K. Mikula and D. Ševčovič, *Computational and qualitative aspects of evolution of curves driven by curvature and external force*, Computing and Visualization in Science **6** (2004), 211–225.
- [27] K. Mikula, M. Remešíková, P. Sarkoci, and D. Ševčovič, *Manifold evolution with tangential redistribution of points*, SIAM J. Sci. Comput. **36**, no. 4 (2014), A1384–A1414.
- [28] A. Schmidt and K. G. Siebert, *Design of Adaptive Finite Element Software*, Lecture Notes in Computational Science and Engineering **42**, Springer (2005).
- [29] J. Steinhilber, *Numerical analysis for harmonic maps between hypersurfaces and grid improvement for computational parametric geometric flows*, PhD thesis, University of Freiburg (2014). URL <http://www.freidok.uni-freiburg.de/volltexte/9537/>